Universidad de Salamanca

Doctoral Thesis

Fabrication and characterization of graphene nanodevices

Author:
Cayetano Sánchez-Fabrés Cobaleda

Supervisor:
Dr. Enrique Diez Fernández

A thesis submitted in fulfilment of the requirements for the degree of Doctor of Philosophy

in the

Grupo de Física No Lineal
Departamento de Física Fundamental

April 10, 2014

"The most beautiful experience we can have is the mysterious. It is the fundamental emotion that stands at the cradle of true art and true science. Whoever does not know it and can no longer wonder, no longer marvel, is as good as dead, and his eyes are dimmed"

Albert Einstein, *Mein Weltbild* (1931)

UNIVERSIDAD DE SALAMANCA

Abstract

Facultad de Ciencias
Departamento de Física Fundamental

Doctor of Philosophy

Fabrication and characterization of graphene nanodevices

by Cayetano Sánchez-Fabrés Cobaleda

In this Thesis our results on the fabrication of graphene nanodevices and their magnetotransport properties will be shown. In particular, we have fabricated several graphene nanodevices exploring the routes to field effec transistors using different approaches and fundamental physics research using Hall bars, Corbino rings and more exotic geometries.
We have studied the quantum Hall effect in several graphene nanodevices: bilayer graphene and trilayer graphene, studying the transport regimes when unwanted charged dopants are present in the device.
We extended our studies on the quantum Hall effect and characterized the plateau-plateau quantum phase transition in a high mobility bilayer graphene device. Our results on the quantum phase transitions showed to be compatible with a percolation scenario in which the critical exponent of such transition is $\gamma = 4/3$.
We have also studied the low field regime in a monolayer graphene device and a bilayer graphene device. For the monolayer graphene device, the trigonal warping is manifested in the destruction of the weak antilocalization. The bilayer graphene sample showed different transport regimes (from insulator like to metallic like) driven by the density. Furthermore, a change in the temperature resulted in ballistic transport for higher densities.
Finally, the interplay between the graphene surface and a thin film of tantalum has been studied. We have observed a clear difference between the charge transfer from 3D porous carbon and tantalum and that from 3D porous graphene and tantalum, manifested in a modification of the superconducting properties of thin films of tantalum.

Acknowledgements

It is at the end of a four years period when, looking back, I realise to how many people I am indebted to. First of all, this thesis would not haven been finished without the priceless help of my Ph.D advisor Enrique Diez. Not only you have taught me all I know about Low Temperature Physics, but also encouraged me in those difficult times, showing enthusiams and a new approach to hard times. Thanks to you I have grown both as a person and as a physicist.
I would also like to thank his neverending support to José María Cerveró, his empathy, wisdom and advice showed more humanity and personal values than . Thanks also to Yahya Meziani, the value of your help at the laboratory and your constant availability to solve any problem I could encounter can't be described.
To Mario I would like to dedicate some special words. Your first explanations on graphene and the quantum Hall effect have really helped, but what I thank the most is your constante help and empathy, either at the clean room, during those skype conversations or gmail talks. I can't forget about the beers and meals either!

Vittorio, thank you very much for your constant enthusiam and optimism at work, either during these long days at Grenoble or working with the data and papers. Your hard work writing and working has been inspiring, helful and very fruitful. You have certainly *tirado del carro* at very difficult times. Sergio, it has been a pleasure and enlightening experience to work with you. The number of ideas jumping out of your head and the positive spirit is always something pleasant to rely on! Of course, parties at home cannot be disregarded! Francesco, thanks for sharing times and worries during a long part of this four years. Your constancy and help during the nights at Grenoble has been of great help in this work.
Thank you also to David López-Romero. You have taught me all I know about device fabrication and clean room processes. Without your help and support I'd be still looking for the best resist. Thanks also to Maika Sabido and Alicia Fraile for your help and patience with my "no gloves" policy.

Thank you Wei for your warm welcome in Albuquerque, your help and advice and priceless knowledge Thank you also to all the people from Grenoble and Toulouse with your help and professionalism. In particular, I would like to thank specially Duncan Maude, Walter Escoffier, Benjamin Piot and Fabrice Iacovella for their help, explanations and fruitful discussions. Fabrice, I hope you haven't forgotten your keys anymore!

I have many friends whom I would like to mention. During these four years, I've had the pleasure to share the joys and sorrows of a very important part of my life with Roberto and Marta. Thank you bros. Not just for the beers, coffees and lunches we've had during this time, but for the support and extra teaching about, well, lots of stuff.
Luis, we started together our journey to planes and stuff and I will never be able to express the gratitude I owe you when you encouraged (*strength and honour!*) me to follow my dream. Hadn't it been because of you, I would probably be now doing something else, so part of this thesis is yours. Good job!
Anita, since we met you have always showed that you are a good friend to rely on. Your constant support and advice, in work and non-related work issues, truly gave some rest to a weary mind. I'm finishing one important part of my life, and you have always had a nice word to help me keep focused and optimist. Thanks.
Javier (yep, I'm calling you by your name), we started as archenemies, we ended up sharing geeky hobbies and here we are now, grown men. It is a pleasure seeing that a person you've met as a kid has now become a good man. Thank you for sharing your time and beer knowledge with me. I must also say, that I feel proud to have you as one of my friends. Thank you for sharing your worries with me, listening to my advice and giving me yours in return. I can't forget about M&M. Thanks, Molina and Montejo, who knows what would've happened if we hadn't met at university. Your company, nights out, and endless hours at the library were the best motivation to study those bloody hamiltonians. And of course, our facebook and whatsapp chats have proven to be the best way to keep inspired at work! Also, without Monty I probably would have never started with one of the biggest passions in my life: music. Monty, your cryptic musical lessons, though useless, were very interesting. I think, I haven't quite understood them yet :P. Moli, stop messing around in the library and work. You're too old for that stuff now.

Thank you Анастасия for being there for me whenever I've needed you. The illusion you've brought can't be described with words. You've made it easy to deal with difficult times, encouraging me to always do my best. You've had a faith in me bigger than mine. Thank you.

Last but not least, thanks for those I know will always be there for me: my family. Thanks to my mother in the first place. I love you and you have made me the man I am now, flawed, but trying to improve in all aspects of my life. Thanks to my siblings: Manuel and Luis and Rocío. I don't really know what I can say to you, but thank you. I know this is something I'll never stop telling you. Love you guys.

Contents

Abstract v

Acknowledgements vii

Contents ix

List of Figures xiii

1 Introduction and motivation of this Thesis 1

2 Graphene: From the theory to the experiment 7
2.1 Introduction . . . 9
2.2 Making of graphene . . . 10
2.2.1 Exfoliated graphene . . . 10
2.2.2 Chemical Vapor Deposition . . . 11
2.2.3 Epitaxial graphene . . . 12
2.2.4 Reduced graphene oxide . . . 13
2.2.5 Dependance on the substrate . . . 13
2.3 Processing of graphene devices . . . 14
2.3.1 Exfoliation of graphene, identification of the flake and preparation 14
2.3.2 Electron beam lithography . . . 15
2.3.3 Reactive Ion Etching . . . 15
2.3.4 Metallic contacts deposition . . . 17
2.3.5 Top gates . . . 19
2.3.6 Bonding . . . 19
2.3.7 Obtained devices . . . 20
2.4 Summary and conclusions . . . 25

3 Cryogenics and magnetotransport 27
3.1 Cryogenics . . . 29
3.1.1 Cryofree ^{3}He pulse tubes cryostat Heliox® . . . 30
3.1.2 Cryo-free ^{3}He/^{4}He dilution cryostat Triton® . . . 32
3.1.3 ^{4}He continuum flux cryostat . . . 36
3.1.4 ^{3}He Cryostats with Internal Adsorption Pumps . . . 37
3.2 Magnets . . . 37
3.2.1 Superconducting magnets . . . 37
3.2.2 Resistive magnets . . . 38

3.2.3 Pulsed magnets . . . 38
3.3 Transport measurements . . . 39
3.4 Summary and conclusions . . . 40

4 Quantum Hall effect in graphene nanodevices 41
4.1 Introduction . . . 43
4.2 Quantum Hall effect in graphene . . . 46
4.2.1 Quantum Hall effect in monolayer graphene . . . 46
4.2.2 Quantum Hall effect in bilayer graphene . . . 47
4.2.3 Quantum Hall effect in trilayer graphene . . . 48
4.3 Characterization of the devices by magnetotransport measurements . . . 50
4.4 Results on the quantum Hall effect in bilayer and trilayer graphene . . . 52
4.4.1 Results on the QHE in bilayer graphene . . . 52
4.4.2 Results on the QHE in trilayer graphene . . . 54
4.5 Four layered graphene . . . 60
4.6 Summary and conclusions . . . 62

5 Quantum phase transitions in bilayer graphene 63
5.1 Introduction . . . 65
5.2 Experimental measurement of plateau-plateau quantum phase transitions 67
5.2.1 Characterisation of the h-BN /bilayer graphene/h-BN . . . 67
5.2.2 Study of the plateau-plateau transition in high mobility bilayer graphene . . . 71
5.3 Summary and conclusions . . . 78

6 Zero and low field transport regimes in graphene 79
6.1 Introduction . . . 81
6.2 Weak localization . . . 81
6.2.1 Weak localization and weak antilocalization in monolayer graphene 82
6.2.2 Weak localization in a h-BN/bilayer graphene/h-BN heteroestructure . . . 87
6.3 Zero magnetic field characterization of a h-BN /bilayer graphene/h-BN heteroestructure . . . 88
6.4 Summary and conclusions . . . 92

7 Superconductivity in 3D porous graphene 95
7.1 Introduction . . . 97
7.2 Fabrication of 3D porous graphene structures . . . 97
7.3 Results on Ta decorated 3D porous graphene and 3D porous carbon . . . 99
7.4 Summary and conclusions . . . 103

8 Conclusions and open questions 105

A Introducción y motivación de la Tesis 111

B Resumen y conclusiones de la Tesis 115

C List of publications **119**

Bibliography **121**

List of Figures

2.1 Honeycomb lattice of graphene. . . . 9
2.2 Band structure of monolayer graphene. . . . 10
2.3 Flake of graphene observed under the optical microscope. . . . 11
2.4 Typical graphene device design. . . . 16
2.5 Graphene flake after the lithography which defines the contacts. . . . 16
2.6 Broken graphene device. . . . 17
2.7 Graphene flake tailored into two Hall bars. . . . 17
2.8 Graphene device before and after the evaporation of the contacts. . . . 18
2.9 SEM image of a broken graphene device after using ultra sounds. . . . 18
2.10 Optical image of a graphene FET using XR resist as dielectric between the top of the graphene and the top gate. . . . 20
2.11 Optical image of a processed graphene device after the soldering of the gold wires. . . . 20
2.12 Picture showing the boxes containing the fabricated samples. . . . 21
2.13 Comparison between a tailored graphene flake and a non-tailored flake. . . . 22
2.14 SEM image of a monolayer-bilayer junction. . . . 22
2.15 Optical image of a graphene device in Corbino geometry. . . . 23
2.16 SEM image of a graphene based quantum ring. . . . 24
2.17 Optical image of a FET before and after adding the dielectric layer and the top gate. . . . 24

3.1 Phase diagrams of ^{4}He and ^{3}He . . . 29
3.2 Pictures of our cryostat Heliox. . . . 30
3.3 PT diagram of the pulse tube cycle and sketch of the physical system. . . . 31
3.4 Homemade sample holder for our *Heliox* cryostat. . . . 32
3.5 Vapor pressure as a function of temperature for ^{4}He and ^{3}He . . . 33
3.6 Cryostat Triton. . . . 33
3.7 Phase diagram of ^{3}He/^{4}He mixture. . . . 34
3.8 Homemade tail used in our *Triton* cryostat. . . . 35
3.9 Calibration of our RuO_2 thermometer using a nuclear thermometer. . . . 36
3.10 Sketch of the setup used in the measurements. . . . 40

4.1 Diagram of Landau Levels as a function of the Fermi energy. . . . 44
4.2 IQHE measured at 300 mK with a InGaAS/InAlAs QW. . . . 45
4.3 FQHE measured in a GaAs/AlGaAs QW at temperatures from 53 mK to 867 mK. . . . 46
4.4 Lattice structure of AB bilayer graphene and band structure at low energy. 48
4.5 QHE observed using a bilayer graphene sample on top of Si/SiO_2 . . . 49

4.6 Lattice structure of ABC stacked graphene and ABA stacked graphene. . 49
4.7 Sketch of the side view of a typical graphene device. 51
4.8 Optical image of the device N11. 52
4.9 Dirac peak of the device N11. 54
4.10 QHE as a function of V_g measured using the device N11. 55
4.11 Mobility as a function of density for our bilayer graphene device N11. . . . 56
4.12 Optical image of the trilayer graphene device N33. 56
4.13 Raman spectrum of the device N33 57
4.14 Isotherms of $\rho(B)$ measured using the device N33 58
4.15 $\Delta R(B)$ 59
4.16 Isotherms of ρ_{xy} and ρ_{xx} as functions of the magnetic field. 59
4.17 n and μ as functions of T. 60
4.18 Isotherms of σ_{xy}(a) and σ_{xx}(b) as functions of B for the device N33 . . . 61
4.19 Optical image of a four layered graphene flake. 61
4.20 Dirac peak and R_{xy} at different gate voltages as functions of B. 62

5.1 Optical image of the h-BN /bilayer graphene/h-BN structure. 68
5.2 Dirac peak of the h-BN /bilayer graphene/h-BN structure. 69
5.3 ρ_{xy} as a function of B at $T = 300$ mK at gate voltages from -15 V to 15 V. 69
5.4 ρ_{xx} as a function of B at $T = 300$ mK at gate voltages from -15 V to 15 V. 70
5.5 ρ_{xx} and n as functions of V_g and μ as function of n. 71
5.6 ρ and σ as functions of B 71
5.7 Isotherms of ρ and σ as functions of B at $V_g = 15$ V 72
5.8 $(\partial\rho_{xy}/\partial B)_{max}$ as a function of T for $n = 6.07 \cdot 10^{11}$ cm^{-2}. 73
5.9 Isotherms of ρ_{xx} and ρ_{xy} as functions of B at different carrier densities. . 74
5.10 Close view of the PP transitions under study. 74
5.11 $(\partial R_{xy}/\partial B)_{max}$ for the different transitions as functions of T and fitting with scaling law. 75
5.12 $1/\rho$ as a function of n. 76
5.13 T_0 as a function of $|\nu - \nu_c|$ 77

6.1 Sample S2601 (monolayer graphene on Si/SiO_2 83
6.2 Resistivity and density as a function of the gate voltage. 84
6.3 Transition from WAL to WL. 85
6.4 Transition from WAL to WL. 85
6.5 Supression of WAL in graphene. 86
6.6 WL dependence on temperature for our h-BN /bilayer graphene/h-BN heteroestructure. 87
6.7 L_ϕ as a function of T for our h-BN /bilayer graphene/h-BN heteroestructure. 88
6.8 $\rho_{xx}(V_g)$ at temperatures from 0.3 K to 50 K. 89
6.9 $\rho_{xx}(T)$ at different gate voltages. 90
6.10 (a) and (b): Linear $\sigma_{xx}(T)$. (c) and (d): $\ln \rho_{xx}(T^{-1/\alpha})$. 91
6.11 Transport regimes driven by the density and the temperature observed at zero field 93

7.1 Scheme of the fabrication process of 3D porous graphene. 98
7.2 SEM images of the 3D porous carbon and porous graphene devices studied before and after the Ta coating. 99

7.3 Sketch of the geometry used in our samples. 100
7.4 R as a function of T for 3DG-Ta. 100
7.5 (a) and (c): Resistance as a function of the magnetic field at different temperatures. (b) and (d) Critical magnetic field as a function of the temperature. 102
7.6 Normalized differential resistance. 103

Chapter 1

Introduction and motivation of this Thesis

In a revolutionary and inspiring lecture Richard Feynman stated that “there’s plenty of room at the bottom" [1]. What did he mean? In 1959 researchers and scientists had started to develop the study of microelectronics and the miniaturization of chips. Yet, Feynmam was aware that the path had only been opened.
Scientists managed to confine electrons in a few nanometers wide space, forcing electrons to move in a plane owing to the quantum confinement. This confinement results in a drastically different behaviour from that of 3D systems. For instance, the discovery of the quantum Hall effect in 1980 [2] revealed that, in fact, the confinement of charge carriers leads to new effects.
The observation of the quantum Hall effect was the cornerstone of a new line of research in Physics. Indeed, the samples were improved and the observation of the fractional quantum Hall effect in 1982 [3] opened even more questions, as this consequence of the many body interactions deeply affects the behaviour of matter.
The quantum Hall effect is a quantum phenomenon observable in macroscopic samples. It relies on the fact that when a magnetic field is applied perpendicular to a bidimensional electron gas additional quantization of the states is achieved. As a result, if a current is injected through the sample and the resistance is measured perpendicularly to the direction of the current, it is observed to be quantized in a series of plateaus. Soon after the discovery of the quantum Hall effect, the transient between two plateaus was understood as a localization-delocalization quantum phase transition [4, 5]. Furthermore, it was observed that such plateaus were quantized having the same values independently from the sample, which became of crucial importance in the study of the fundamental properties of matter and metrology.
Nonetheless, even though the resistance follows the same quantization independently from the sample, it was soon observed that the transient from one plateau to the next one (that is, each quantum phase transition) were not necessarily the same for the different samples. This fact opened the question as to whether the quantum phase transitions follow any kind of universal behaviour, governed by the Anderson localization model[6, 7] or not and, if so, under what conditions.

These studies had been carried out using quasibidimensional InGaAs/InAlAs quantum wells in which the electrons were confined in to a plane. Nonetheless, it was known that bidimensional electron gases in certain conditions could have more exotic properties than those observed in quantum wells. In fact, in a seminal work by P.R. Wallace [8], it was found that if a layer of graphite is isolated, electrons in that graphite layer would follow Dirac equation instead of Schrödinger’s. Wallace’s aim was to set a premilinary point from which the properties of graphite (candidate to be used in electronics rather than silicon) could be well understood. Little did he know that his work would inspire the quest for the 2D carbon allotrope: graphene.

Indeed, by the late 20^{th} century, 0D and 1D carbon allotropes (fullerenes [9] and carbon nanotubes [10, 11]) had been found and their research were showing promising and interesting results. Nonetheless, the 2D allotrope had to wait to be found. It was in 2004 when Geim and Novoselov found, using a rather surprising approach (but quite effective), that scotch tape could effectively cleave graphite, breaking it and separating the layers from one another until, eventually, one single layer of graphite was isolated. This layer of graphite was called graphene [12].
Graphene became suddenly one of the hottest topics in Physics. And not without reason. First of all, it is truly a material of atomic thickness. There was, indeed, plenty of room at the bottom. Second of all, since it is a real bidimensional material, effects such as the aforementioned quantum Hall effect could be investigated without the "artificial" confinement of electrons (see Ref. [13] and references therein).
Moreover, graphene fastly probed to be a wonder material in terms of applications [14]: it is one of the hardest materials known, it is an astonishing good electrical conductor and its reduced thickness could be the solution to a further miniaturization of microchips. Furthermore, it is a semiconductor with no bandgap and in which the nature of carriers (holes or electrons) can be modified simply by applying an electrical field perpendicular to the sample. On top of that, the fact that charge carriers obbey the relativistic Dirac equation, allows the study of certain quantum electrodynamics effects without requiring large facilities such as those of the Large Hadron Collider.

In this Thesis we have studied the fundamental properties of graphene, studying the quantum Hall effect in several graphene devices. We have also and characterized the quantum phase transitions, adding more information to the universality debate and studied the different transport regimes in a high mobility graphene device, shedding some relevant light to the potential applications of graphene in the sense that well defined transport regimes are tuned by changing the temperature and the density. Finally, we have studied how the sp^2 graphene bonds affect the superconducting properties of tantalum, as opposed to the effects that sp^3 carbon bonds might have.

This Thesis is divided as follows.

- In Chapter 2 we introduce the main properties of graphene and discuss the different ways that researchers have found to produce graphene. Obviously, each way has its advantages and drawbacks, which will also be commented. We will also illustrate in detail the method used to fabricate in clean room facilities the devices under study. We will show some of our devices and comment on the geometries of each device.

- Chapter 3 is devoted to the experimental techniques which have allowed us to perform our study. Namely, we will show the physical principles of the cryostat we have used, paying a detailed attention to the cryo-free systems used that the *Laboratorio de Bajas Temperaturas* in Salamanca. We will also explain the different kinds of magnets used in our experiments.

- In Chapter 4 we will show and explain the quantum Hall effect in standard two dimensional electron gases and graphene. Particularly, we will show the quantum Hall effect in bilayer graphene and trilayer graphene, showing the quantization of the resistance and the properties of the materials that can be extracted from these measurements.

- We will extend our study of the quantum Hall effect to the characterization of the plateau-plateau quantum phase transitions in a hegaxonal boron nitride and bilayer graphene heterostructure. In Chapter 5 we will show our results on several plateau-plateau transitions, revealing a non universality of the localization-delocalization transition.

- The opposite regime to that of the quantum Hall effect will be studied in Chapter 6. In this Chapter we will study the behaviour of graphene when a small magnetic field is applied. We have observed a transition from weak localization to weak antilocalization in monolayer graphene. In a hexagonal boron nitride and bilayer graphene heterostructure, we have identified several transport regimes tuned by modifying the temperature and the carrier density.

- During a three-month stage at Sandia National Laboratories I had the chance to investigate the superconducting properties of a thin film of tantalum when on top of both 3D porous graphene and 3D porous carbon. The fabrication process needed to obtain such samples, as well as the results of the experiments will be presented in Chapter 7.

- In Chapter 8 we will discuss the overall conclusions of this work, stressing the most important results.

Chapter 2

Graphene: From the theory to the experiment

The production of graphene has attracted a huge interest in the last year. In this chapter we firstly explain the basic theoretical properties of graphene and then we discuss the experimental devices that we obtained and how they were processed.

2.1 Introduction

Graphene was first isolated in 2004 [12], but sixty years before that Wallace had described the band structure of graphene [8]. What started as a prologue to further understanding of the electronic properties of graphite resulted in the deduction of the key property of charge carriers in graphene.

The lattice structure of graphite consists on a planar structure where the carbon atoms in each layer are arranged in a honeycomb lattice, as seen in figure 2.1.

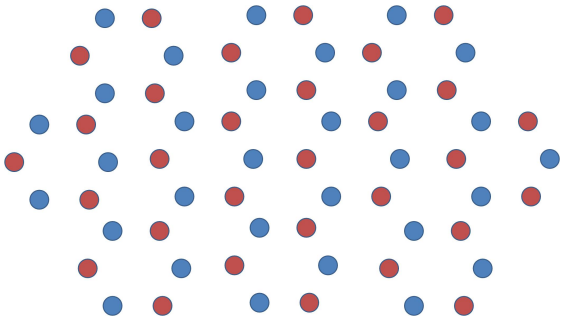

Figure 2.1 Honeycomb lattice of graphene. Circles of the same colour belong to each one of the triangular sublattices.

Thus, monolayer graphene can be described as an unrolled single wall carbon nanotube which has a planar structure of sp^2-bonded carbon atoms in a 2D honeycomb lattice. This can be viewed as two intercalated triangular lattices. Each one of these lattices will result in a triangular reciprocal lattice as well, making the reciprocal lattice of graphene to be also an hexagonal lattice.

In this reciprocal lattice, the conduction band and the valence band intersect six points. Of these six points, there are two sets of three equivalent points each. Each set belongs to one of the triangular reciprocal sublattices. The two inequivalent points (belonging to different reciprocal sublattices) are called K and K'.

At the points K and K', the energy dispersion of the conduction and the valence band is linear and there is no electrical gap between the two bands (see Fig. 2.2). As a consequence, the carriers in graphene behave as massless Dirac particles instead of Schrödinger particles (with parabolic energy-momentum dispersion) and have a Fermi velocity which is 300 times smaller than the speed of light. This results in the possibility of study some properties predicted by quantum electrodinamics (QED) without the use of enormous facilities or accelerators [15].

Also, graphene *is* a truly 2D material. Before the isolation of graphene, 2D systems could only be studied by means of electron confinement: either quantum wells, or heterojunctions. But these are not *truly* bidimensional materials but electrons (or holes) forced to move in a plane of several Å of thickness. Being graphene a purely 2D material allows

us to study the fundamental properties of low dimensionality, such as the quantum Hall effect (see section 4.2) and weak localization (section 6.2).

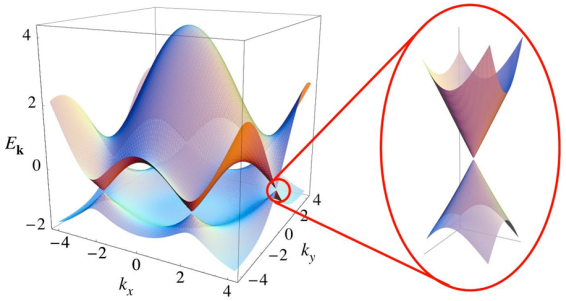

Figure 2.2 Band structure of monolayer graphene. The zoom at low energies shows that close to the points K and K', the charge carriers in graphene behave as massless Dirac particles. Figure adapted from Ref. [15]

Besides its interesting fundamental properties, the (atomic) thickness of graphene and the high Fermi velocity of its carriers, as well as the possibility of easily switching the transport regime from electron-like to hole-like, make graphene one of the most promising materials for the semiconductor industry [14].

2.2 Making of graphene

In this section the different methods to obtain graphene will be discussed. In particular, we will focus on the mechanical cleavage method, as this was the method used to obtain the majority of our samples. We will also introduce the difference of the quality of the graphene samples depending on the substrates on which graphene is deposited.

2.2.1 Exfoliated graphene

Exfoliated graphene is also known as mechanically cleaved graphene. This method, firstly developed by Geim and Novoselov [12], to isolate graphene relies on the weakness of the Van der Waals force. By repetitively cleaving a graphite crystal it is possible to isolate one layer of graphene and then transfer it to a substrate.
The procedure is as follows: a crystal of graphite is stuck on an adhesive tape, which is folded onto itself. When unfolded, the graphite crystal will be peeled, being part of the crystal in an area of the tape and another crystal on a different area. By doing this repetitively, the graphite will be peeled off and thick areas of graphite will be spread on the tape. After that, the carbon residues can be transfered onto a substrate by applying

a gentle pressure on the tape when it is on the subtrate.
After gently removing the tape from the substrate, the graphene has to be identified. Usually the easiest way to identify graphene relies on multilayer interferometry. It is remarkable that a layer of atomic thickness can be identified by optical means. If a graphene flake is on 300 nm of SiO_2 the contrast between the graphene flake and the substrate is maximised and has a value of 12% at 550 nm [16]. Furthermore, thick graphite flakes have a yellowish colour, fading into blue colours as the thickness decreasses and turning finally into light purple for graphene, as seen in figure 2.3.

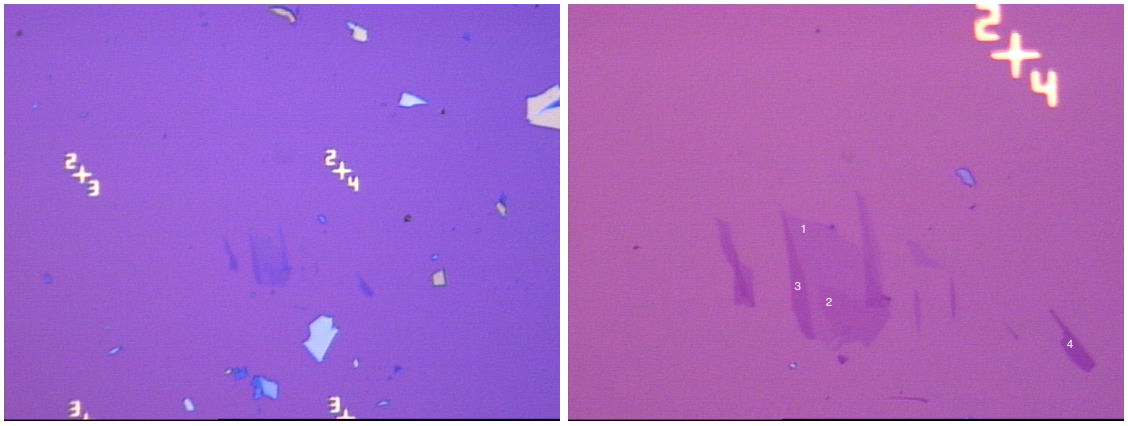

Figure 2.3 Flake of graphene observed under the optical microscope (Nomarsky confocal microscope) at 200X (left) and 500X (right). We can see in the left image light blueish flakes, which correspond to thick graphite crystal. As the thickness decreases, the colour turns darker. For graphene the colour is purple, and the lightness of the colour depends on the number of layers.

The main advantage of this method is the quality of the graphene crystals, since these samples have mobilities $\sim 20000\,\mathrm{cm}^2/\mathrm{Vs}$ when on top of Si/SiO_2 [13] and $> 100000\,\mathrm{cm}^2/\mathrm{Vs}$ when suspended [17] or on top of hexagonal boron nitride (h-BN) [18],which makes exfoliated graphene the most suitable for fundamental physics research. Since the graphene layers are peeled off, the lattice of the graphene is homogeneous along the sample, except small defects. In contrast, the main disadvantage of this method is the fact that it is highly time consuming and not reproducible, with the added inconvenient of the small size (about hundreds of square microns) of the samples which results in an increased difficulty to obtain graphene for industrial purposes.

2.2.2 Chemical Vapor Deposition

In order to overcome the low reproducibility and small size of the samples new methods have been developed. One of them is using chemical vapor deposition (CVD) techniques

to obtain graphene [19].
Tipically, hydrocarbons are introduced in a chamber at a pressure and flow which depends on the experience of the group and their setup. The hydrocarbons are heated up at temperatures above 1000 °C, resulting in the decomposition of the molecule. The carbon is then attached to a metallic foil (being cupper the most usual). Each of the carbon atoms form a seed to which the carbon atoms will join, resulting in a graphene flake. The setup is then cooled down and the metallic foil is completely covered by graphene. Once the system has been cooled down then graphene is transfered onto an isolating substrate using (tipically) PMMA resist.
This system has two obvious advantages: the flakes of graphene obtained are almost as big as the metallic foil and the reproducibility depends on the setup of the equipment. Moreover, the graphene flakes can be transferred to almost any substrate after it has been grown. The scalability and the posibility to choose the substrate on top of which the graphene is deposited is very appealing for industrial and technological applications. As a matter of fact, there are a number of companies which produce CVD graphene for industrial purposes (Graphene Supermarket and Graphenea). Companies such as Samsung, Philips or Nokia are working on finding a way to make the most out of these posibilities. The main disadvantage of this technique is the low mobility (usually $\lesssim 1000$ cm^2/Vs) of the carriers in these graphene systems when compared to exfoliated graphene. Nonetheless, it has been recently shown that CVD grown graphene on h-BN can exhibit mobilities as high as ~ 37000 cm^2/Vs [20].

2.2.3 Epitaxial graphene

This technique uses silicon carbide (SiC) as a precursor [21]. SiC is heated up to temperatures above 1300 °C in high vacuum. Under these conditions the silicon sublimate and the carbon atoms reorganize forming graphene layers. If this process is continued during time more layers of graphene will be added on top of the previous ones.
More recently, CVD grown graphene on SiC with mobility up to ~ 2000 cm^2/Vs has been produced [22].
The main shortcoming of this procedure is the difficulty to control the number of graphene layers. On the other hand, this system allows the growth of large-scale graphene layers.

2.2.4 Reduced graphene oxide

This method uses pristine graphite which is oxidised using oxidisers as sulphuric acid [23]. The oxidation results in removing an electron from the graphene in a redox reaction. The reaction increases the interplanar distance between the layers in graphite. When the graphite has been completely oxidised it can be dispersed in water, where sonication is applied, producing graphene oxide. This graphene oxide can be reduced following different approaches: treating graphene oxide with hydrazine hydrate, exposing graphene oxide to hydrogen plasma or thermally reducing graphene oxide by heating it at temperatures over 1000 °C. The main advantages of reduced graphene oxide are the high surface of material which can be fabricated and high scalability of the process, which could have potential applications in the development of batteries. In contrast, the processes usually result in poor electronic conductivity, imperfections and vacancies in the lattice and reducing the mechanical strength of the reduced graphene oxide.

2.2.5 Dependance on the substrate

Since graphene is a material of atomic thickness, the interaction it has with the substrate highly affects the electronic properties of the material. Another parameter of great importance is the flatness of the substrate, since if the substrate is not flat, it will lead to a corrugation of the graphene, which will most likely create unwanted effects. Thus, the different substrates onto which graphene can be deposited will be discused.

Graphene on SiO_2

The first and mainly used substrate is SiO_2 . It consists of a layer of 300 nm of SiO_2 on top of a highly doped Si wafer which allows us to identify graphene using an optical microscope. It has been shown that the presence of SiO_2 beneath the graphene layer induces a large carrier density inhomogeneity, combined with a corrugation of the graphene sheet. As a consequence, the mobility of graphene is reduced and the transport phenomena must be carefully analised in order to separate the effects caused by the inhomogeneity from the effects under study.

Suspended graphene

One of the approaches that can be taken in order to improve the quality of the sample consists on eliminating the SiO_2 underneath the graphene layer [17]. After following the

steps later described (in section 2.3) the device is dipped into a 1:6 buffered oxigen etch (BOE) for 90 seconds. As a result, $\sim$ 150 nm of SiO_2 are removed, including the SiO_2 that is below the graphene layer. The only remaining SiO_2 is the layer which is masked by the metallic contacts. After that, the device is submerged in ethanol and dried in a critical point drying step in order to avoid the collapse of the suspended graphene layer induce by surface tension.
The main advantages of these devices is the high mobility achieved and the low induced residual charges. This also implies that only certain metals can be used as contacts, since the wet eching might damage the metal. However, a new method which does not require BOE has been developed [24]. Nevertheless, the process is not trivial and the devices are very delicate, requiring a very careful handling and usually being damaged during transportation.

Graphene on *h*-BN

An easier method to circumvent the inconvenients of SiO_2 whilst not facing the difficulties of suspended graphene relies on hexagonal boron nitride (*h*-BN) [18, 25, 26]. This material can be exfoliated following an equivalent procedure to the exfoliaton of graphene, resulting in a flat surface onto the graphene can be deposited. Also, the lattice structure of *h*-BN consists on a hexagonal honeycomb lattice with a mismatch of 1.7% of that of graphene. As a consequence, because of the flatness of the substrate there are no ripples on the graphene sheet. This, combined with the small mismatch between the graphene lattice and the *h*-BN lattice, the mobility of graphene devices on *h*-BN are orders of magnitude greater than the mobility of graphene on SiO_2 .

2.3 Processing of graphene devices

In this section the followed procedures to obtain a graphene device will be explained. We will start from the preparation of the wafer and proceed to discuss each step of the process. We will also show the most representative devices and geometries that were processed.

2.3.1 Exfoliation of graphene, identification of the flake and preparation

The first step consists on cleaning the Si/SiO_2 wafer. The usual procedure is submerging the wafer in acetone, in order to dissolve any impurities. Once the wafer has been in

acetone for about two minutes, it is submerged in alcohol (usually ethanol or propanol) to remove the acetone. Again, after thirty seconds, the wafer is taken out of the alcohol and dried using a nitrogen gun. Then, the wafer must be heated up to temperatures above 100 °C in order to evaporate any water or remaining alcohol. Usually this is done using a hot plate.
Once the wafer is clean, graphene can be exfoliated and deposited onto the wafer as explained in subsection 2.2.1. This was usually done in the Laboratorio de Bajas Temperaturas in Salamanca and in the CT-ISOM (Central de Tecnología-Instituto de Sistemas Optoelectrónicos y Microtecnología). After our graphene flakes were obtained by mechanical exfoliation they were characterized by Raman spectroscopy. Graphene flakes were placed on top of a Si/SiO_2 (380 μm phosphorus doped silicon and 280 nm of SiO_2 on top).

2.3.2 Electron beam lithography

The design of the device is done after measuring the geometry of the actual flake with the optical microscope. Using a commercial program provided by CRESTEC the desired device (pads, mesa and top gates if needed) is designed. In figure 2.4 we show a screenshot with the program used to design the devices. We can see the design of the mesa; the contacts and pads; and the graphene flake as a reference.

The sample is coated with polymethyl methacrylate PMMA (AR-P 671.05) (our experience with other resists such as ZEP520 resulted in losing the graphene). The sample is spinned during 45 s at 4500 rpm in order to have an homogeneous layer of PMMA covering the whole wafer. After that, the sample is heated up at 120 °C during two minutes in order to bake the resist. The litography is then started. We used an electron beam lithography system (CRESTEC CABL 9500C) with a dose of $\sim$ 200 $\mu C/cm^2$ and the energy of the beam was 50 keV. Once this step is finished, the resist is developed, meaning that the resist in the exposed areas will be removed. In order to do that, the sample is submerged in the developer AR600.56 during $\sim$150 s and after that it is submerged in 2-propanol for $\sim$30 s. In figure 2.5 we show a graphene sample after the contacts have been defined.

2.3.3 Reactive Ion Etching

Depending on the shape and size of the graphene flake a mesa tailoring might be required. If a special geometry of the device is needed, then the graphene flake must be tailored

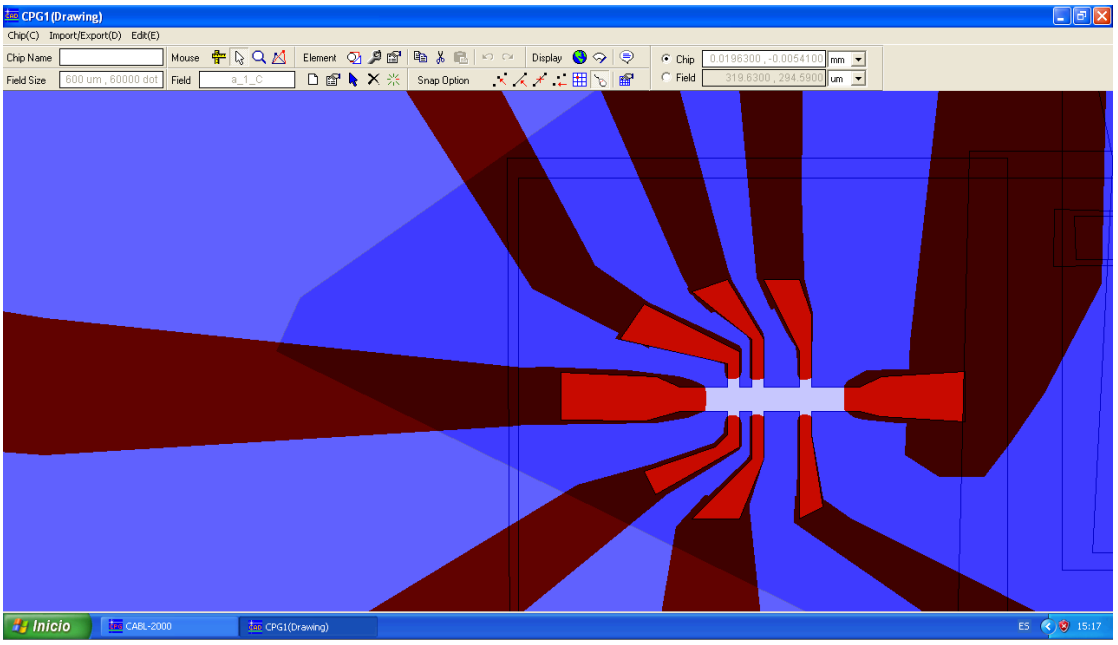

Figure 2.4 Typical graphene device design. In white we see the part of the graphene flake which won't be exposed in the lithography. The geometry of the sample will be a Hall bar. In blue we have marked the areas of the flake which will be exposed in the first lithography (before the Reactive Ion Etching process) and in red (dark and light) we have marked the areas which will be exposed in the second litography in the step previous to the evaporation of the contacts.

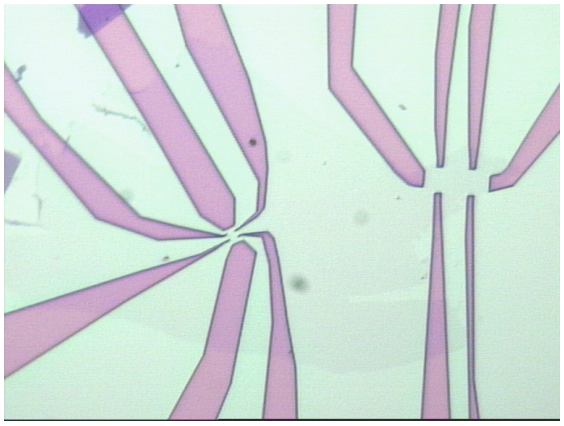

Figure 2.5 Graphene sample after the contacts have been patterned by the lithography and the resist has been developed. In light green we see the unexposed resist (and the graphene under it) and in light purple we see the parts of the resist that have been exposed and developed. We will evaporate metal in these regions to use them as contacts in the final device.

to have the desired geometry. Also, our experience has proven that the adherence of the metal used in the contacts to the graphene is low, so if the sample suffers any vibration the metal might be removed from the sample and the graphene sample will be lost, as shown in Fig. 2.6. In order to avoid that, the surface of graphene under the metal region should be as small as possible, and hence tailoring is needed.

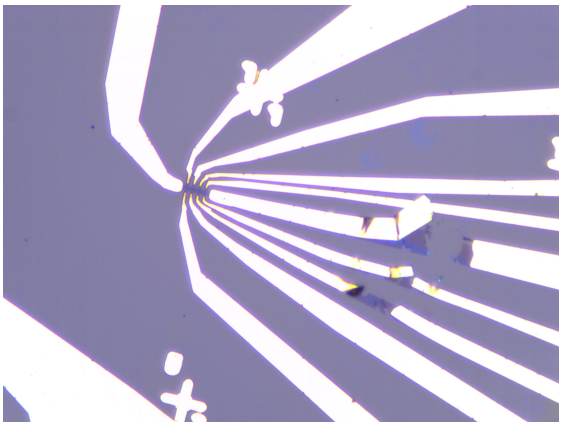

Figure 2.6 Broken graphene device. The contacts on the right side were broken during transportation from the CT-ISOM (Madrid) to our laboratory in Salamanca. This was due to the large area of graphene under the contacts and the low adherence between the metal and the graphene

We have achieved that using oxygen plasma reactive ion etching (RIE). This technique consists on creating an oxygen plasma which will react with the carbon atoms of the graphene which is not covered by resist. The reaction leads to CO and CO_2, and eliminates the exposed carbon. Nonetheless, since the O_2 plasma also reacts with the resists, care must be taken. Usually, 30-60 s of plasma created with 13 W of power (using a PlasmaLab μ80) suffices to remove one layer of graphene and it is yet not enough to remove the resist (which would result in removing more graphene than wanted). In figure 2.7 an image of a tailored graphene flake is shown.

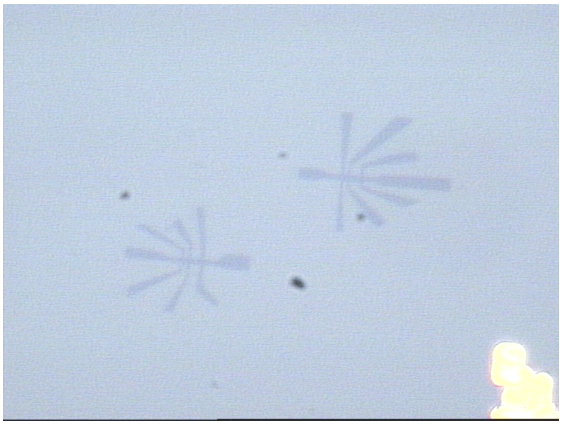

Figure 2.7 Graphene flake tailored in the geometry of two separate Hall bars before the deposition of the metal.

2.3.4 Metallic contacts deposition

After the graphene flake has been tailored (if needed), a second lithography is done in order to define the geometry of the contacts, as seen in figure 2.8 (left).

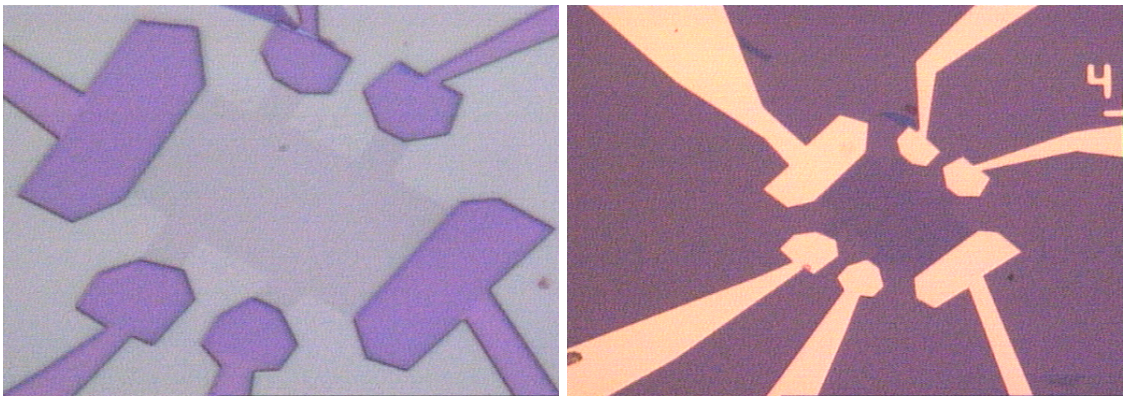

Figure 2.8 Optical image of a device of graphene before the metallic contacts have been deposited (left) and after the metal has been deposited (right).

After the lithography and the development (following the procedure explained in subsection 2.3.2) the device is placed in a VARIAN ultra high vacuum evaporator. The metal is heated up by a 10 kV electron beam which hits the pot that contains the metal. The metal is evaporated and arrives the surface of the sample, covering the whole surface. Nonetheless, since almost all the surface of the device is covered by resist, all the metal which is on top of the resist will be removed.
We deposited 5 nm of titanium followed by 50 nm of gold, as from our experience this thickness suffices to bond the contacts and it can be easily removed with a lift-off process.

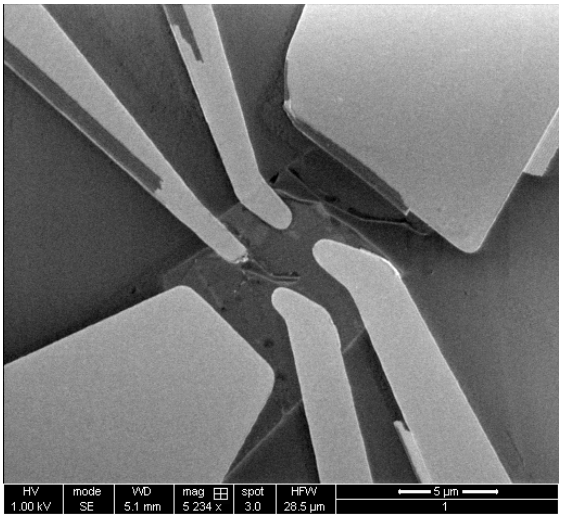

Figure 2.9 SEM image of a broken graphene device after using ultra sounds.

In order to remove the undesired gold, the sample is submerged in warm acetone at 60 °C (which removes the resist and the gold attached to it) during several minutes, until the film of gold starts to separate from the sample. A smooth current of acetone can be applied with a syringe in order to accelerate the process. However, ultra sounds should be avoided, since they usually result in the breaking of the sample (see figure 2.9). Once

the gold has been removed (except that which is to be used for the contacts) the sample is submerged in alcohol to remove the acetone.

2.3.5 Top gates

Top gates are an essential requirement in the fabrication of field effect transistors (FETs). They allow the creation of an electric field which is perpendicular to the sample. This is achieved by adding contact on top of the graphene layer with a dieletric layer between the gate and the graphene. This allows us to modify the density of carriers in the area below the gate by applying an electrical field.
Top gates demand an insulating layer between the graphene and the gate. We used a few nanometers of SiO_2 are deposited via CVD on top of the sample, covering everything. Since we need to have access to the contacts deposited previously, the SiO_2 on top of them must be removed. This is done by a lithography process in which we expose the areas of SiO_2 that are above the pads. The resist is removed and the SiO_2 which isn't covered by resist is etched by a SF_6 RIE. After that, the process explained in 2.3.2 and 2.3.4 is repeated in order to deposit the metallic contact of the gate.
Since covering the sample with SiO_2 would probably have increased the interaction of the graphene flake with the SiO_2 (the substrate and the required layer of SiO_2 for the top gate) and thus increased the inhomogeneity of the sample, the residual density of carriers and reduced the mobility, we tried a new approach.
Instead of covering the whole graphene layer with SiO_2 , we used a resist (XR e-beam resist) as dielectric. Being able to control the area in which the resist would be deposited (by doing a lithography and removing the unwanted resist) the interaction would be reduced. In picture 2.10 an optical image of the graphene device with two top gates (using XR resist as dielectric) is shown.

2.3.6 Bonding

The sample is then ready to be mounted on a sample holder. We used 8 pin double in line (DIL) flat ceramic sockets. We attached the samples to the holder using silver paint, which allowed us not only to glue the sample to the holder, but also provided us of a good electrical contact between the Si of the wafer and the back gate contact (this contact allows us to control the carrier density of the sample).
After that, the gold wires are bonded to the pads. In this step a wire of gold (ø=20 μm) is soldered to each one of the metallic pads, and from there, the wires are soldered to

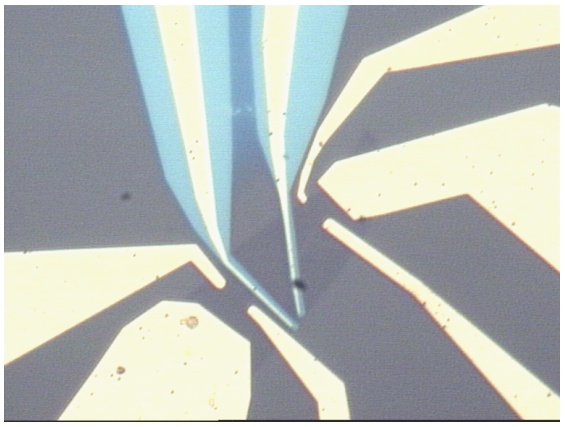

Figure 2.10 Optical image of a graphene FET using XR resist as dielectric between the top of the graphene and the top gate. The light blue areas are the zones covered by XR resist and the yellow contacts are the gold contacts, both the ones touching the graphene and the ones on top of the dielectric used as top gates.

the pins of the DIL (see figure 2.11).

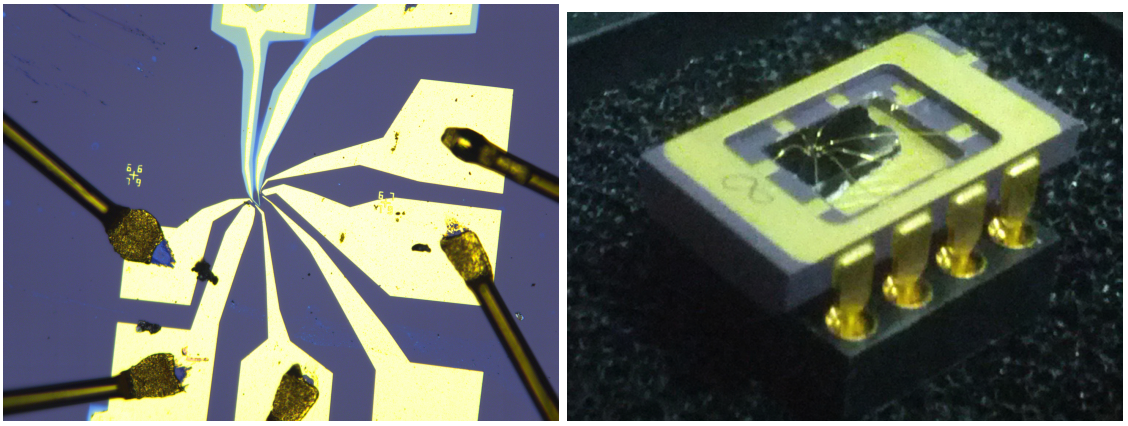

Figure 2.11 Left: optical image of a processed graphene device after soldering the gold wires.
Right: Optical image of a typical chip (graphene device glued to the DIL socket) used in our experiments.

2.3.7 Obtained devices

We designed and processed tens of devices with exfoliated graphene and some with CVD graphene (see figure 2.12). In this section we will show just and example of some of the different devices that were processed in the clean room. We fabricated standard Hall bars for experiments in the quantum Hall regime (using CVD graphene and exfoliated graphene), quantum interferometers, monolayer and bilayer junctions, field effect transistors, Corbino rings.

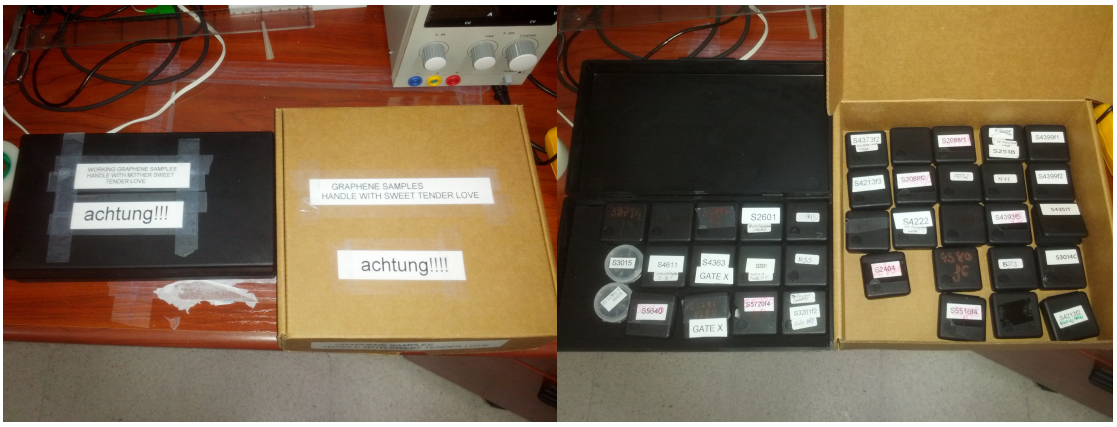

Figure 2.12 Picture showing the boxes containing the fabricated samples.

Nonetheless, the fabrication of graphene devices is a very delicate task which requires several attempts to fabricate a high quality device. Although we fabricated many samples (some of them having several devices on them) most of our devices could not be used for our experiments because of broken contacts, leaks in the dielectric or high density of doped impurities in the sample. Additionally, these devices are highly delicate, and extremely careful handling must be kept in mind. However, some of the devices were damaged during transportation to external facilities. Though not all of the devices worked as good as expected, we will review now some of our most common geometries Therefore, though we fabricated many devices, along this thesis we will present the most representative results that we obtained.

Hall bars

Hall bars are designed to perform magnetotransport measurements in the framework of the QHE. The geometry consists of a rectangular shaped device with one contact in each extreme and several contacts on the sides of the sample.
The contacts on the extremes will usually be used as source and drain contacts, whereas the contacts on the sides will be used in pairs: the contacts on the same side will be used to measure the longitudinal resistivity ρ_{xx} and the contacts on different sides (one in front of each other) are used to measure the perpendicular (Hall) resistivity ρ_{xy}.
In figure 2.13 (left) we show a Hall bar device without tailoring after the lithography which defines the pads and the right image in Fig. 2.13 shows a device in Hall bar configuration without etching.

Using this geometry several devices were processed: monolayer, bilayer, trilayer and

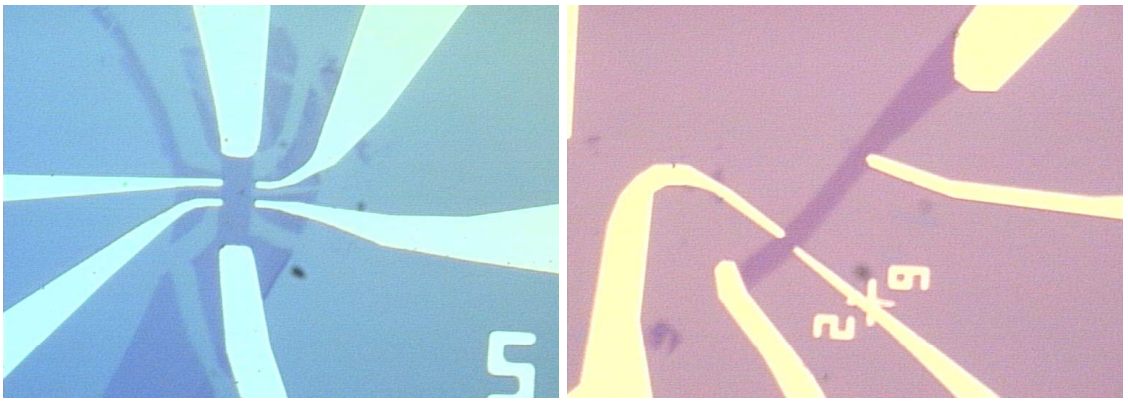

Figure 2.13 Left image shows a tailored graphene device in Hall geometry. The right image shows a graphene Hall bar without tailoring.

tetralayer graphene samples. Nonetheless, further combinations were obtained. In figure 2.14 we show a device in a Hall bar geometry where part of the sample is monolayer graphene and the other part is bilayer graphene.

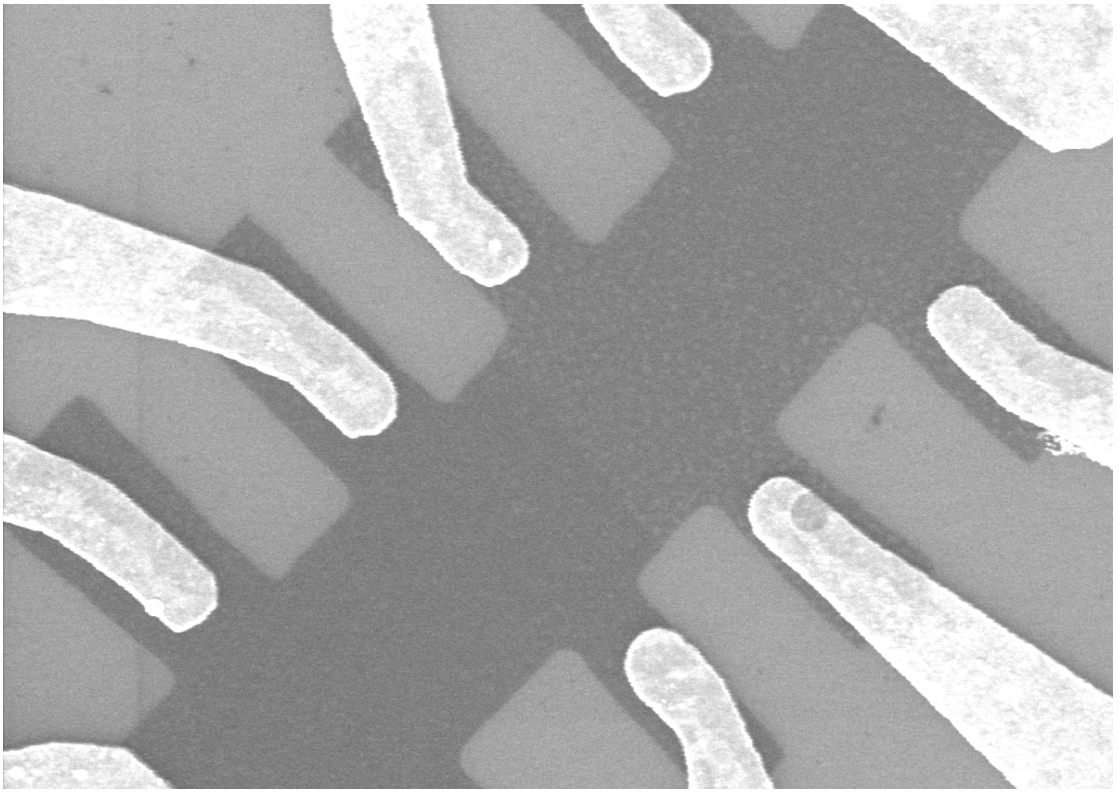

Figure 2.14 SEM image of a graphene device tailored in a Hall bar geometry in which one half of the sample is monolayer graphene and the other half is bilayer graphene.

Corbino geometry

This geometry has been of huge interest to solid state physicists because by using this geometry edge current effects can be avoided [27–29].

The Corbino geometry consists of two circular shaped contacts one within another. The inner contacts is disk and the outer contact is a circular crown with a bigger inner diameter than the diameter of the inner disk. Thus, in between the two contacts there is a graphene sheet with the shape of a crown as shown in figure 2.15.
By doing so, there are two edge currents flowing in oposite directions (one around each contact) cancelling each other.

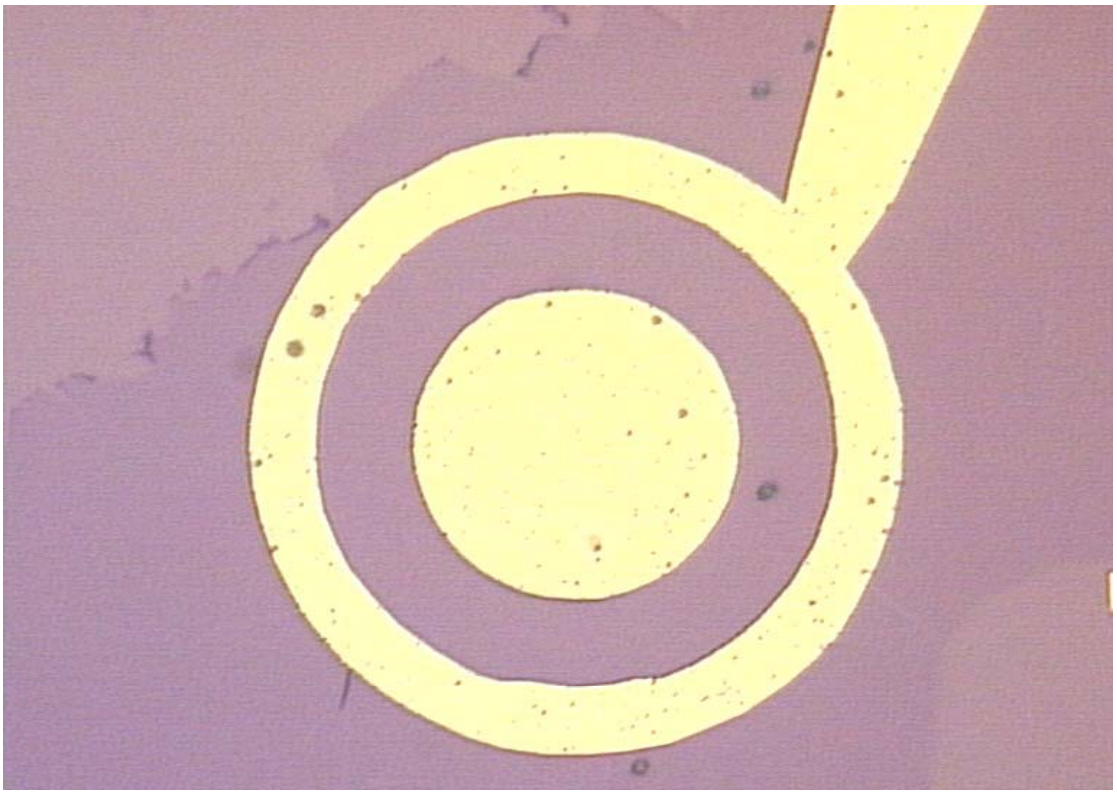

Figure 2.15 Optical image of a graphene device processed in Corbino geometry. We can see the inner and outer contacts surrounding the graphene.

Quantum interferometers

We also processed devices (shown in figure 2.16) which were produced to study fundamental and quantum interference. By making the current to follow two different paths and collecting the current at the same point, if the phases of these two flows are changed within the source-drain trajectory, intereference effects of the wave functions will be observed [30].

Field effect transistors

We processed some field effect transistors (figures 2.17 and fig. 2.10) in order to study a route to have graphene devices showing an amplification factor and a way to control

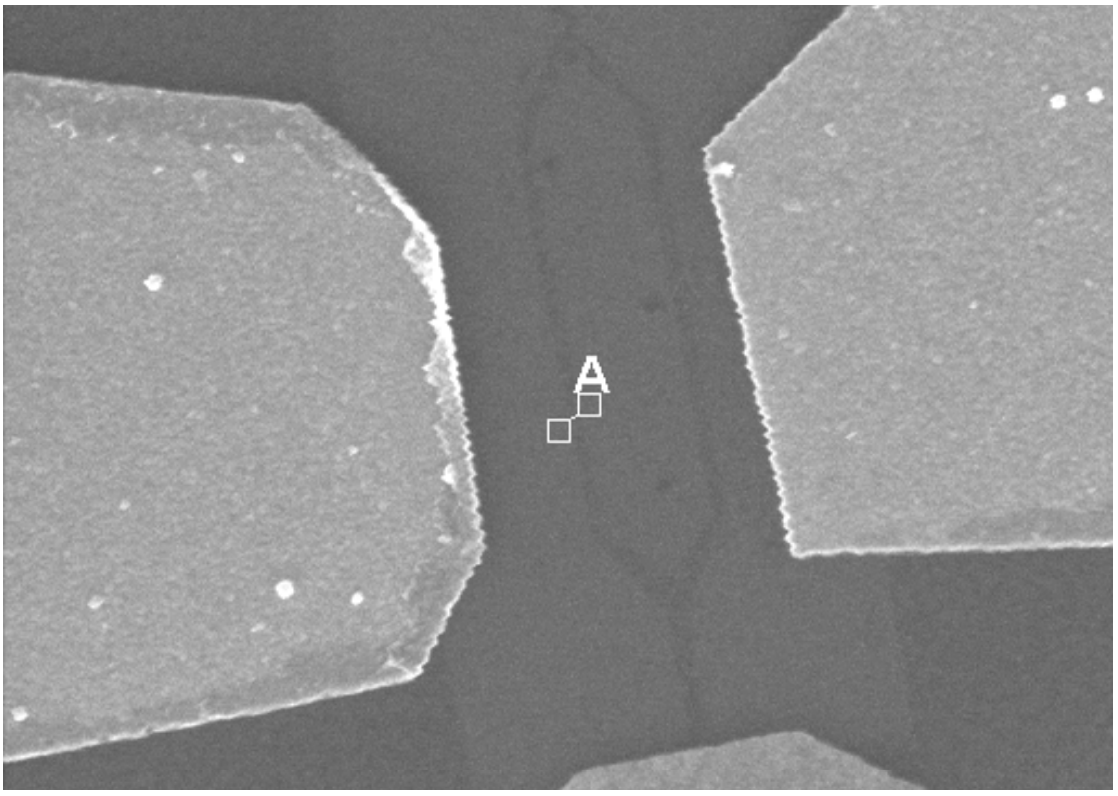

Figure 2.16 SEM image of a quantum ring designed to measure interference effects. We can see the source and drain contacts and two side gates (which do not touch the graphene) whose function would be applying a voltage difference between the two paths, resulting in a difference of the phase. The width of the graphene sheet is $A = 43$ nm.

the current; as well as a route to terahertz detection [31]. However, the transistors we fabricated using either SiO_2 or RX resist showed an amplifaction factor of about 1 %. Now, we are working on using h-BN as the dielectric layer and we hope that it will result in a higher amplification factor.

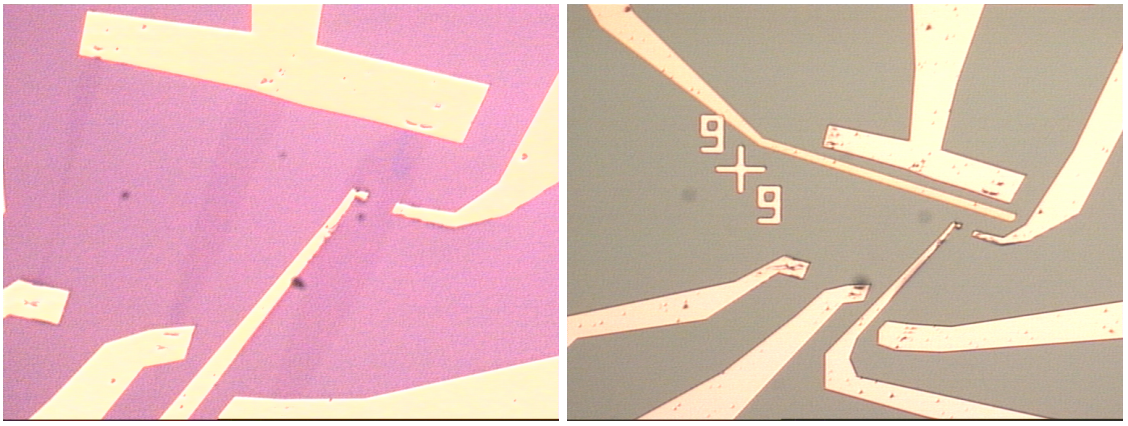

Figure 2.17 Left: Optical image of three graphene samples with a common contact before adding the SiO_2 layer and the top gate.
Right: Based on graphene FET after adding the SiO_2 layer and the top gate, common to the three graphene devices.

2.4 Summary and conclusions

In this Chapter we have briefly introduced the basic properties of graphene and we have throughly explained all the steps involved in the process of graphene.
We have shown the methods we used to produce our exfoliated graphene and some of the devices we obtained. We have also commented on the problems we had to deal with and the steps which usually resulted in the breaking of the sample. The standard protocol we decided to follow (as it was the most optimal, resulting in less damaging than other procedures) started with cleaning the surface of the Si/SiO_2 wafer from adsorbants and impurities using acetone and alcohol. Graphene was mechanically exfoliated on top of the Si/SiO_2 wafer and characterised by Raman spectroscopy and contrast measurements. The wanted device was designed and patterned by means of e-beam lithography using PMMA as e-beam resist, whether with or without RIE tailoring. We have explained how the metallic contacts are evaporated and the different approaches to deposit a top gate. Finally, the process is finished by cleaving the device from the whole wafer, attaching it to a DIL socket and bonding the metallic wires.

Chapter 3

Cryogenics and magnetotransport

Quantum phenomena usually require extreme low temperatures and high magnetic field in order to reach what is known as extreme quantum limit. In this chapter we will review the techniques we have used to obtain such low temperatures and high magnetic fields.

3.1 Cryogenics

In this Chapter we will describe the different cryogenic techniques we have used and the types of magnets used in our experiments. Finally, we will review the well known lock-in technique that was used in our magnetotransport measurements.
For futher information on low temperature techniques, the reader is encouraged to find more information in Ref. [32].
For more than 100 years, liquid helium has been the main material used in the cryogenics equipments. Tipically two isotopes of helium are used, ^{4}He and ^{4}He . ^{4}He is the most stable isotope of helium and is the most common, being obtained mainly from natural gas resources. On the other hand, ^{3}He is very rare and constitutes a fraction $\sim 10^{-7}$ of helium gas coming from natural resources. Since separating these two isotopes is very costly, usually ^{3}He comes as a byproduct of tritium in nuclear reactors:

$$\begin{aligned} {}^{6}_{3}Li + {}^{1}_{0}n &\Longrightarrow {}^{3}_{1}T + {}^{4}_{2}He \\ {}^{3}_{1}T &\Longrightarrow {}^{3}_{2}He + {}^{0}_{-1}e + \bar{\nu} \end{aligned}$$

The main fundamental difference between ^{4}He and ^{3}He is their nuclear spin. ^{4}He has two protons and two neutrons, having a total nuclear spin $I = 0$, which results in bosonic particle, whereas ^{3}He has a nuclear spin $I = 1/2$ resulting a fermion.

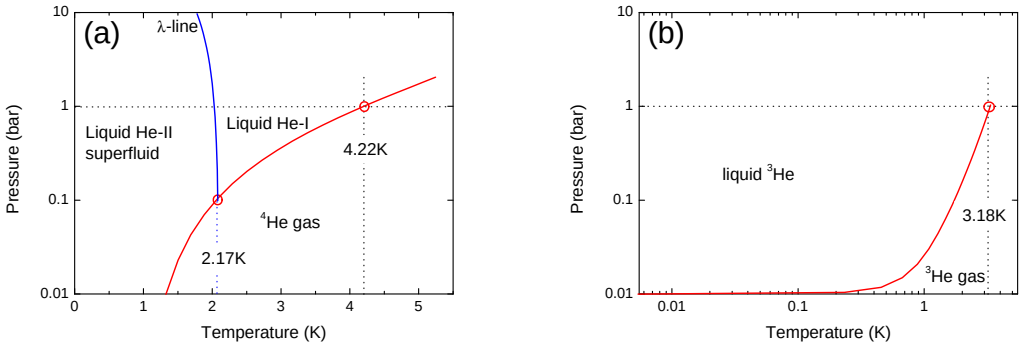

Figure 3.1 Phase diagrams of ^{4}He (a) and ^{3}He (b).

As shown in figure 3.1, ^{3}He has the transition to liquid state at 1.22 K, whereas ^{4}He has the transition to liquid state (known as He-I) at 4.22 K (and 1 bar of pressure). ^{4}He remains behaving as a normal liquid at atmospheric pressures until 2.17 K and 0.1 bar. Under this condition, ^{4}He undergoes a transition to a superfluid state, known as He-II. Nonetheless, by further reducing the pressure, He-I can be cooled down at 1.2 K.
^{3}He liquifies at 3.19 K at atmospheric pressure, but reducing the vapour pressure allows us to cool it down at temperatures down to 250 mK.
It is necessary to remark that both liquid ^{3}He and ^{4}He have very low latent heat of

evaporation (20-80 J/mol), which results in a very small cooling power. As a consequence, evaporating liquid ^{3}He and ^{4}He is very easy and efficient shielding and precooling (with liquid nitrogen usually) are required.

3.1.1 Cryofree ^{3}He pulse tubes cryostat Heliox®

This cryostat (shown in Fig. 3.2), from now on refered to as *Heliox*, was specially designed in collaboration with Oxford Instruments® for our Laboratorio de Bajas Temperaturas at Salamanca.
The operation of this cryostat is remarkable because it allows us to cool down the sample in vacuum to 250 mK without the use of barely any cryogenic liquid. This is achieved by using an adiabatic cycle of expansions of ^{4}He .
The principle of this system relies on letting helium expand against an external force. This is achieved by a rotatory valve which produces oscillations of pressure.

Figure 3.2 Left picture shows the top part of the cryostat with the cold head and the pulse tubes. The right picture shows the cryostat on top of the magnet. Notice that the cryostat and the magnet are physically disconnected.

In figure 3.3(a) the pressure-temperature diagram of the cycle is shown. The cycle starts at the regenerator of the system (labeled as A in figure 3.3(b)) with helium gas at the minimum pressure p_L and initial temperature T_i (α). The rotatory valve is opened and the helium gas is moved to the pulse tube (PT) plate keeping its temperature constante (β). During this compression phase, the regenerator takes heat from the gas, which is

removed by a heat exchanger. The gas reaches then the pulse tube and is adiabatically compressed until it reaches (γ) a higher temperature and the maximum pressure (p_H). Then, the gas flows through an small orifice onto a reservoir of large volume with small pressure oscillations, giving off heat to the surroundings (δ). After that, the cycle is reversed, starting the expansion phase. The orifice is closed and the rotatory valve starts and expansion cycle of the gas (ϵ) cooling down the helium as it approaches the regenerator. Finally, a small hole is opened, letting the gas flow at constant pressure and temperature (T_f) to the PT plate (η). When the gas arrives to the PT plate, its temperature T_f is lower than the initial temperature T_i. Therefore, the gas absorbs heat from the PT plate, cooling the PT plate down. After that, the helium is sent back to the regenerator, making the cycle start again. Using this technique, the PT-plate can be cooled down at temperatures ~ 3 K.

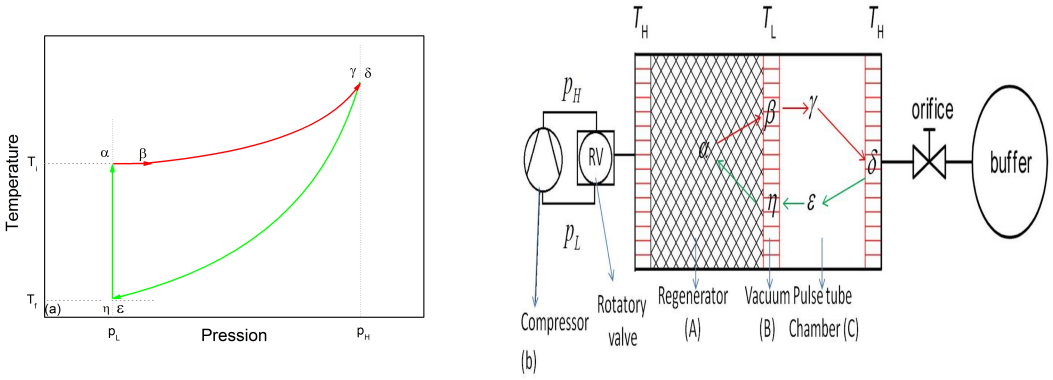

Figure 3.3 (a) PT diagram of the pulse tube cycle. (b) Sketch of the compressor and the dependence of the pressure on the physical position.

This cryostat has a piece of charcoal (called sorb) which can be thermally coupled with the PT-plate via a switch heater. If the switch heater is on, the sorb will be linked with the PT-plate using ^{4}He as exchange gas. Then, a procedure similar to that described in 3.1.4 is started. The sorb is connected to a vessel which contains ^{3}He . Thus, when the charcoal is linked to the PT-plate it is cooled down and adsorbs ^{3}He . Once all the ^{3}He has been adsorbed, a manual valve is closed in order to uncouple the vessel from the sorb and it can be thermally uncoupled from the PT-plate by turning off the switch heater. Once it is unlinked, it can be suddenly heated to 50 K. As a result, all the ^{3}He trapped inside the coal is desorbed, migrating to the ^{3}He pot, where the sample holder is attached. There, since the ^{3}He pot is small, the gas reaches overpressured and liquefies. By connecting the sorb again to the PT-plate, the sorb will be cooled down, and thus will adsorb the remaining ^{3}He gas that is in the ^{3}He pot. This results in reducing the pressure of the liquid ^{3}He (see figure 3.5) and, as a consequence, its temperature. This allows us to cool down the sample to 250 mK, since the sample is thermally coupled to the ^{3}He pot using the connection wires which are wrapped around our low eddy current

homemade tail and in touch with the DIL pins, as seen in figure 3.4. Our sample holder was designed and fabricated by us, and it allows the cooling down of two samples at the same time, since it has two 8 pin DIL sockets.
There are two great advantages of using this system. First of all, no need of costly liquid helium is required, making our installations economically and environmentaly sustainable. Second of all, since the cryostat is not coupled with our superconducting magnet (described in Sec. 3.2.1), it can be used to perform magnetotransport measurements even at room temperature. This would not be possible in conventional systems where the magnet and the cryostat share the ^{4}He bath.

Figure 3.4 Zoom-in of the tail of our *Heliox* cryostat. The tail has two sample holders, allowing us to cool down two samples at once. The samples are cooled down via the connection wires, which are thermally linked with the ^{3}He pot.

3.1.2 Cryo-free ^{3}He/^{4}He dilution cryostat Triton®

This system was bought to Oxford Instruments and we installed it at our Laboratorio de Bajas Temperaturas in 2011. This system allows us to cool down the sample to ~ 35 mK. In figure 3.6 we show the cryostat on top of the magnet whilst being installed without the radiation shields and the outer vacuum chamber wall and the cryostat once its installed ready to be used for our magnetotransport measurements.

This cryostat takes benefit of the same mechanism explained in 3.1.1 as a precooling stage. Once the system is below 1 K we exploit the fact that when a mixture of ^{3}He/^{4}He is cooled down below a critical temperature the two isotopes separate. One of the phases

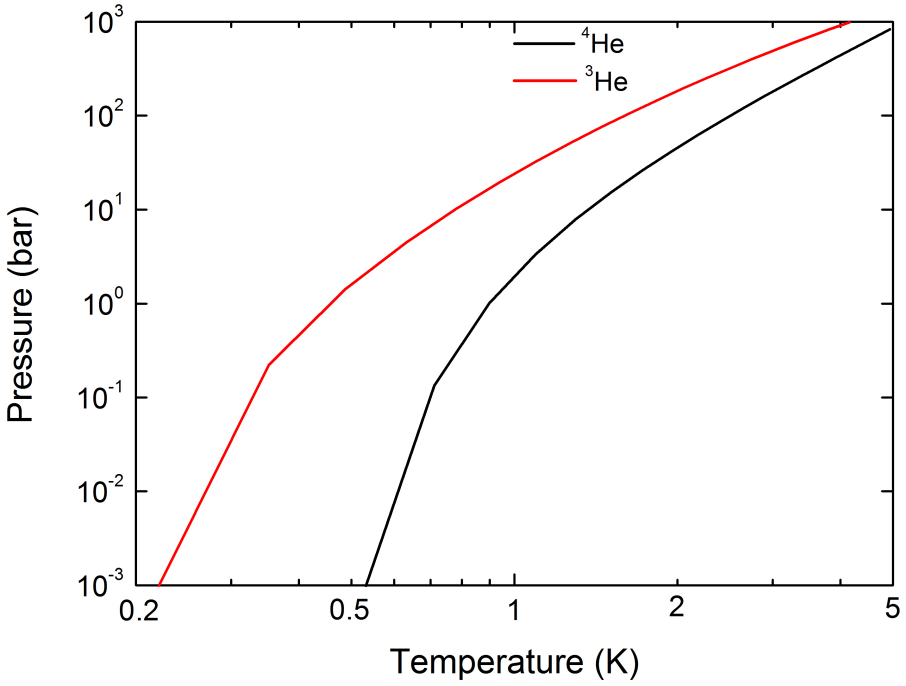

Figure 3.5 Vapor pressure as a function of temperature for ^{4}He (black line) and ^{3}He (red line).

Figure 3.6 Pictures of the Triton cryostat without its radiation shields and OVC wall (left and middle). The different plates and connections can be appreciated. The picture of the right shows the cryostat successfully installed and with its tail inside the bore of the magnet (as the cryostat Heliox shown in figure 3.2).

is lighter (referred to as “concentrated" phase) and is rich in liquid ^{3}He , whereas the other phase is heavier (referred to as “dilute phase") and rich in ^{4}He , with low concentration of ^{3}He gas. In this system, the concentration of ^{3}He depends on the temperature, as shown in figure 3.7.

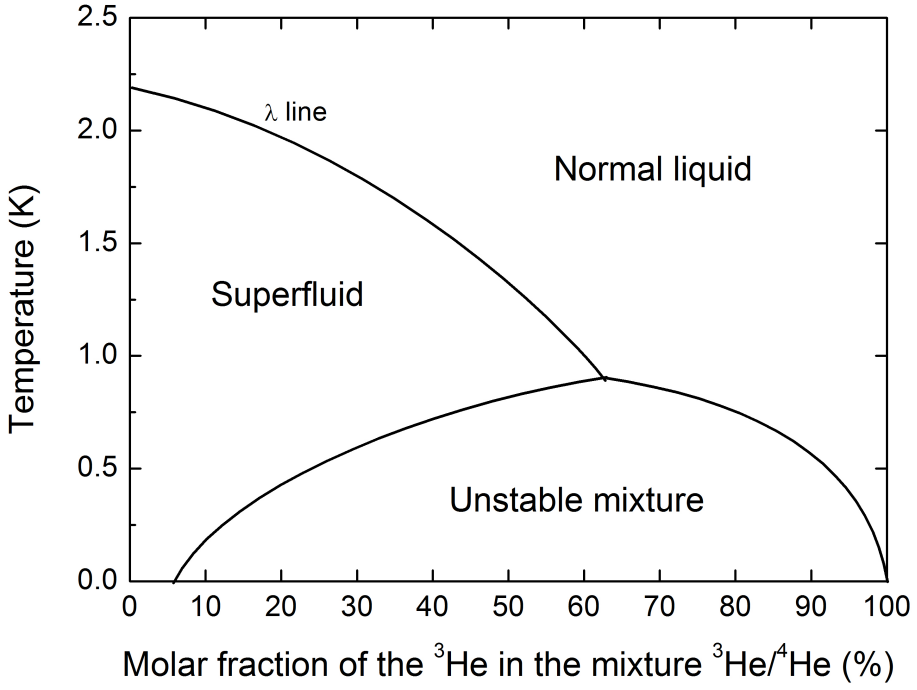

Figure 3.7 Phase diagram (temperature as a function of concentration of ^{3}He) of ^{3}He/^{4}He mixture.

The enthalpy of ^{3}He in each one of the phases is different. As a consequence, if ^{3}He is evaporated from the concentrated phase to the dilute phase, the temperature will be reduced. The ^{3}He gas is formed in the mixing chamber and flows through the liquid ^{4}He with no interaction. As seen in figure 3.7, the mixture is separated into two phases at temperatures below 6 K. The still cools the ^{3}He before it enters the mixing chamber, resulting in the phase separation. Eventually, the dilution unit will be cooled down and the phase separation will be achieved. The ^{3}He is pumped away from the still, which is at 0.6-0.7 K. As seen in figure 3.5, at this temperature the vapour pressure of ^{3}He is roughly 1000 times higher than that of ^{4}He , resulting in the evaporation of ^{3}He majorly to the mixing chamber. Since the specific heat of ^{3}He gas is higher than that of liquid ^{3}He , this phase transition requires heat, and thus the system is cooled down. As a consequence of the flow of ^{3}He from the still to the mixing chamber, the pressure in the still is lower than in the mixing chamber. Due to osmosis, ^{3}He will flow from the mixing chamber to the still, cooling the returning flow of concentrated ^{3}He via heat exchangers

and closing the cycle.

Figure 3.8 Left picture shows the whole tail from the sample holder to the mixing chamber. The right pictures shows a zoom in of the end of the sample holder and the sample holder.

Using this technique, temperatures of the order of ~ 10 mK can be reached in the mixing chamber, which is thermally coupled with the sample, again, using the connection wires which are wrapped around the tail before being connected to the DIL sample holder. Moreover, though only one sample holder is mounted at the end of the tail, there are 24 wires available for use, which would allow us to cool down and measure 3 samples at the same time.

Instead of a low eddy current sample holder, this tail was designed and done with oxygen-free copper in order to achieve the best thermal link with the mixing chamber. Since the tail might be too long (see figure 3.8 to achieve temperatures at the end of the tail as low as in the mixing chamber, an additional thermometer was placed at the end of the tail to monitor its temperature. During the installation of the Triton system, we calibrated

both the mixing chamber and the tail RuO_2 thermometers to the lowest temperatures using a nuclear orientation thermometer (see figure 3.9).

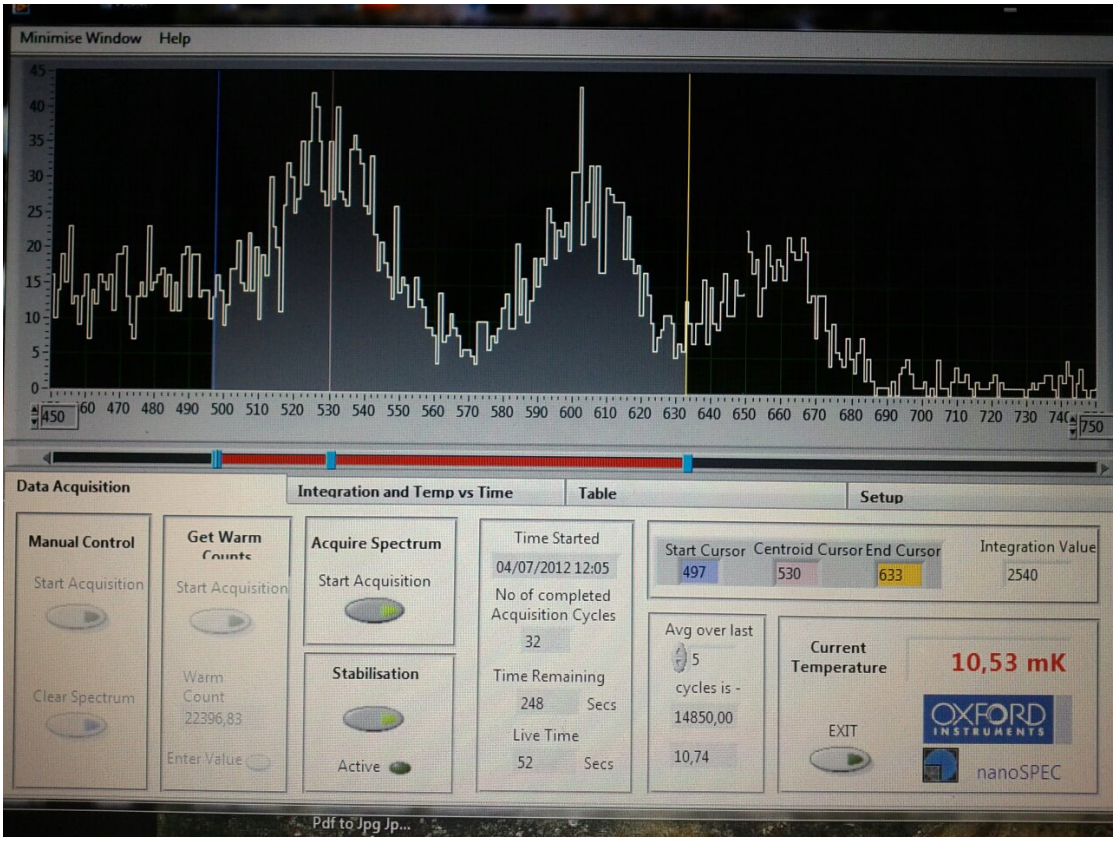

Figure 3.9 Nuclear orientation thermometer measuring a temperature in the mixing chamber of 10.53 mK. This thermometer was used to calibrate our two RuO_2 thermometers (mixing chamber and tail) at their lowest temperature range.

3.1.3 ^{4}He continuum flux cryostat

These cryostats have been used at the Laboratoire National de Champs Magnétiques Intenses in Grenoble. They can operate at temperatures ranging from 1.3 K to hundreds of Kelvin.

The cryostat used belongs to the Variable Temperature Insert (VTI) series by Oxford Instruments®.

Their way of operation is the following: the liquid helium is stored in a dewar and introduced into the cryostat using a transfer tube and the flow is regulated using a needle valve. If temperatures below 4.2 K are to be achieved, a small fraction of the ^{4}He of the bath is introduced into a pot (through a flow impedance) and pumped. Thus, the liquid helium arriving at the pot is isenthalpically expanded and arrives at the pot at which the sample is, cooling it at temperatures below 4.2 K (namely, 1.2 K).

These cryostats are widely used because of their low price and their versatility, since they allow us to work at temperatures from ~ 1.3 K to ~ 300 K.

3.1.4 ^{3}He Cryostats with Internal Adsorption Pumps

This type of equipment was used at the Laboratoire National de Champs Magnétiques Intenses in Toulouse and at Sandia National Laboratories, Albuquerque, New Mexico.
These cryostats' principles are similar to continuum flux cryostats (see section 3.1.3). The procedures used to cool the sample to temperatures ~ 1.2 K are the same, but where it differs is at the further steps. These cryostats can be cooled down to temperatures ~ 250 mK.
It is known that, when cooled, gases adsorb to solid surfaces, and desorb at higher temperatures. These cryostats are based on this principle.
After the cryostat has been cooled to ~ 1.2 K, the sorption pump is heated up and ^{3}He is introduced into the system. A large surface (the sorbtion pump, usually made of charcoal) is kept cold and thus adsorbs ^{3}He gas from the ^{3}He pot. As a consequence, the vapour pressure decreases, resulting in a decrease of the temperature (see Fig. 3.5) cooling down the liquid helium. Once all the ^{3}He gas has been adsorbed, the sorb is be warmed up, resulting in the desorbing of the ^{3}He gas. The gas will reach the ^{3}He pot, which was cold during the adsorbtion of the ^{3}He , and when in contact with the cold walls of the pot, it will cool down and condense again.

3.2 Magnets

Most of the results presented in this Thesis were obtained by the application of magnetic field perpendicular to the sample. In this section we will discuss the kinds of magnets that we have used and their main advantages and disadvantages. We have used superconducting magnets, resistive magnets and pulsed magnets.

3.2.1 Superconducting magnets

Superconducting magnets are the most common in magnetotransport laboratories, as they can reach high magnetic fields (~ 20 T) and they do not require a lot of power to produce high magnetic fields.
This systems require a coil made of superconducting material (tipically Ni_3Sn) through which a high current ($\sim$100 A) flows. The limitation on the magnetic fields comes from

the fact that, as a superconductor, the coil has a critical magnetic field H_{c2}, above which the material behaves as a normal conductor, dissipating a lot of heat (due to the high current) to the surroundings.
Our magnet used at the Laboratorio de Bajas Temperaturas in Salamanca was cooled down by a pulse tube technique similar to that describe in 3.1.1. Our magnet reaches a maximum magnetic field of 12 T and has a bore diameter of 55 mm. Also, with our setup the two cryostats and the magnet are physically and thermally decoupled, which allows us to have a high magnetic field even at room temperature (as seen in figures 3.2 and 3.6).

3.2.2 Resistive magnets

These magnets generate the magnetic field by passing a high current through a metallic coil with ring shape. The use of these magnets allows reaching higher magnetic fields than superconducting magnets and it is not required a high spatial homogeneity. On the other hand, they must be cooled using water, resulting in strong vibrations of the system.
The magnet we have used is made of an outer Bitter magnet with a polyhelix insert at the Laboratoire National de Champs Magnétiques Intenses in Grenoble. This magnet required 20 MW in order to reach its maximum magnetic field, 28 T. Due to the high power required, our time of access to this magnet was limited.

3.2.3 Pulsed magnets

The last type of cryostat that we used reaches very high magnetic fields (60 T) during a short period of time (namelly, 300 ms). We have used this system at the Laboratoire National de Champs Magnétiques Intenses in Toulouse.
The pulses generated by these magnets require 14 MJ provided by a generator made of ten cells with sixty condensers of 24 kV. The coil of the magnet was made of copper and submerged in liquid nitrogen. After each shot, the temperature of the bath rose from 77 K to $\sim$ 300 K. The time needed to cool down the coil was no less than one hour.
Also, due to the short duration in time of the magnetic field, special precautions must be taken. Long loops in the circuit should be avoided in order to reduce spurious signals and eddy currents which would result in heating of the samples.

3.3 Transport measurements

Most part of the measurements which will be presented along this Thesis were taken at the Laboratorio de Bajas temperaturas in Salamanca. Also, some measurements taken at the Laboratoire National de Champs Magnétiques Inteses (Grenoble and Toulouse) and Sandia National Laboratories in Albuquerque, New Mexico will be shown.

The samples were usually glued using silver paint to a 8-pin DIL socket. These sockets have a metallic contact onto which the sample was glued. Since the silver paint is conductive and is in contact with the p-doped silicon of the wafer onto which the graphene was deposited (see Chapter 2) we can use this contact as a back gate in order to modify the carrier density of the samples. This was done using a Keithley® sourcemeter 2601A. Since the dielectric supporting the graphene might be damaged (during manipulation of the sample, RIE processes or fabrication of the wafers) it is desirable to make sure that the applied gate voltage will not drop through the graphene device. In order avoid this effect, a compliance of 10 nA was set, which sets an upper limit to maximum voltage the sourcemeter can apply: if the current measured by the sourcemeter increases above 10 nA, the sourcemeter stops increasing the voltage. Thus, if there is a leak in the dielectric, the leak current will not be greater than 10 nA, keeping the device safe from high currents.
The rest of the main setup works as follows.
We used an DC lock-in amplifier (Standorf Research® 830) (lock-in A in figure 3.10) as a voltage generator of frequency ~ 15 Hz and amplitud $0.5 < V_{AC} < 5$ V. This voltage dropped through an in series resistor of $50 < R_{series} < 500$ MΩ. This allows us to have a small excitation current $1 < i_{AC} < 100$ nA. A small excitation current is wanted in order to avoid heating of the sample due to Joule effect, but on the other hand, some subtle effects (such as weak localization corrections to magnetoconductivity) require a higher current to be properly observed.
We can then set up other lock-in amplifiers to measure *only* the signal of the voltage drop which is in phase of the signal generated by the lock-in A. This reduces the signal/noise ratio and the effect of eletromagnetic contamination.

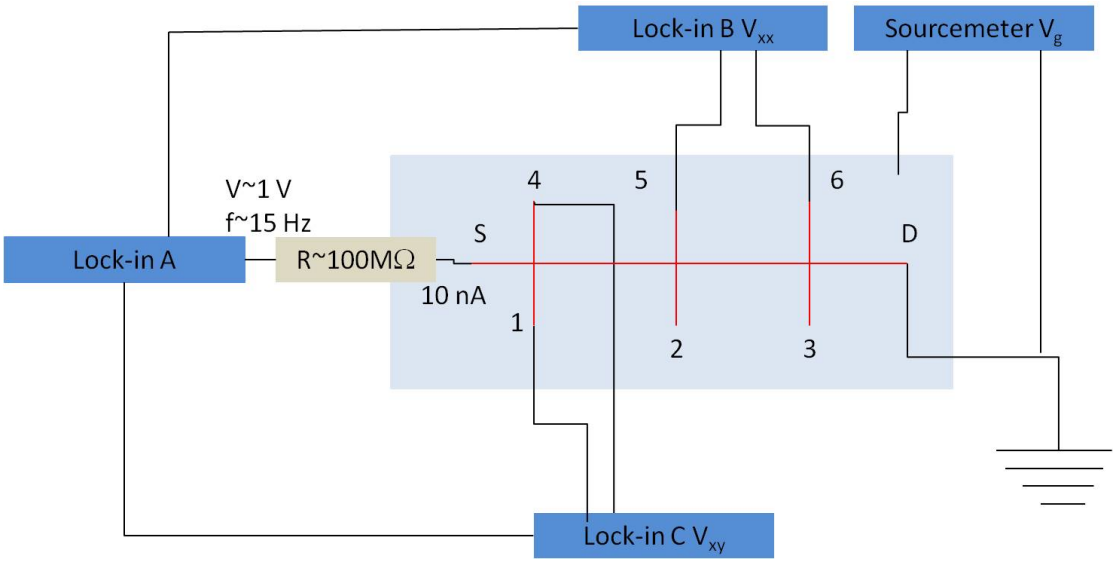

Figure 3.10 Sketch of the setup used. Lock-in amplifier A generates the AC voltage (V_{AC}) which drops through a high resistor (R) which is in series with the sample. Lock-in amplifiers B and C measure the voltage drop along the sample (V_{xx}) and across (V_{xy}) the sample (respectively) using the signal generated by lock-in A as internal reference. With this setup we can know the current flowing through the sample ($i_{AC} = V_{AC}/R$) and we can thus measure the longitudinal (Hall) resistance: $R_{xx(xy)} = V_{xx(xy)}/i_{AC}$.

3.4 Summary and conclusions

In this Chapter we have reviewed the different kinds of cryostats that we have used in our experiments. Their physical principles as well as their main advantages and disadvantages have been explained. Pulse tubes cryostats Heliox and Triton (sections 3.1.1 and 3.1.2) were used at our facilities in Salamanca and most of the our results were used using this equipment.

The different magnet coils have also been introduced, being the superconductive coil the most used during this work. When high magnetic fields were needed, resistive magnets and pulsed magnets were used.

Finally, we have explained the experimental setup used to collect our data.

Chapter 4

Quantum Hall effect in graphene nanodevices

High magnetic fields and low temperatures allows observing a quantized resistance. In this Chapter will review the QHE in graphene and show our results on the quantum Hall effect in graphene.

4.1 Introduction

Two dimensional systems show fascinating properties amongst which we can find the quantum Hall effect (QHE). The QHE was discovered by von Klitzing *et al.* in 1980 and has been since then subject of numerous studies. They found that two dimensional electron gases (2DEGs), at a certain density and magnetic field exhibit a quantized Hall resistance, namely $\rho_{xy} = h/ie^2$, being i an integer [2].
A few years after its discovery, a new kind of quantum Hall effect was found by Störmer, Tsui and Gossard. What they observed was that 2DEGs with extremely high mobility ($\sim 10^6$ cm^2/Vs) shows an Hall resistance with additional quantized values than that observed by von Klitzing. Particularly, their observations were that besides the integer values of the Hall resistance $\rho_{xy} = h/ie^2$, it was quantized following fractional values in the form of $\rho_{xy} = h/fe^2$, where f is a rational fraction [3].

When an electron gas is confined in a two dimensional space (x,y), the energy eigenvalues are given by the expression $E_j = \hbar/2m_x^* k_x^2 + \hbar/2m_y^* k_y^2 + \epsilon_j$ [33]. If the confinement if achieved by means of a quantum well of thickness d_z, the discrete eigenvalues resulting from the quantization in the z-direction are given by: $\epsilon_j \approx \dfrac{\hbar^2\pi^2}{2m_z^*}\dfrac{j^2}{d_z^2}$.
Now, let's suppose that a magnetic field is applied in the z direction. The electrons will be forced to move in circular orbits perperndicular to the magnetic field with a cyclotron frequency $\omega = -eB/m^*$. This results in a harmonic oscillator whose eigenvalues are given by: $E_{j,n,s} = \epsilon_j + (n + 1/2)\hbar\omega + sg\mu_B B$, being $s = \pm 1$ the quantum number, μ_B the Bohr magneton and g the Landé factor.
The magnetic field causes a quantization into Landau levels (LL) separated by an energy $\hbar\omega$. Nonetheless, these Landau levels are degenerated, since the number of states existing prior the quantization must be the same after the quantization into discrete levels. The degeneracy of each LL is $N_L = eB/h$. We can define a quantity known as *filling factor* and which is defined as the ratio between the carrier density n and the degeneracy of the LL: $\nu = n/N_L = nh/eB$ [5].
When the magnetic field is increased, the energy of each LL is higher, and eventually crosses the Fermi energy. When this happens, this LL is emptied and the electrons occupy the next lower Landau level. Further increasing of the magnetic field will result in more LL crossing the Fermi energy. When the Fermi energy lies between two LL, all the states are localized and there is no conduction, since only extended states can carry current (see figure 4.1).

As a result the longitudinal conductivity σ_{xx} and the longitudinal resistivity will be zero ($\sigma_{xx} = \rho_{xx}/\left(\rho_{xx}^2 + \rho_{xy}^2\right) = \dfrac{0}{0 + h/ie^2}$) and the Hall resistivity is quantized following

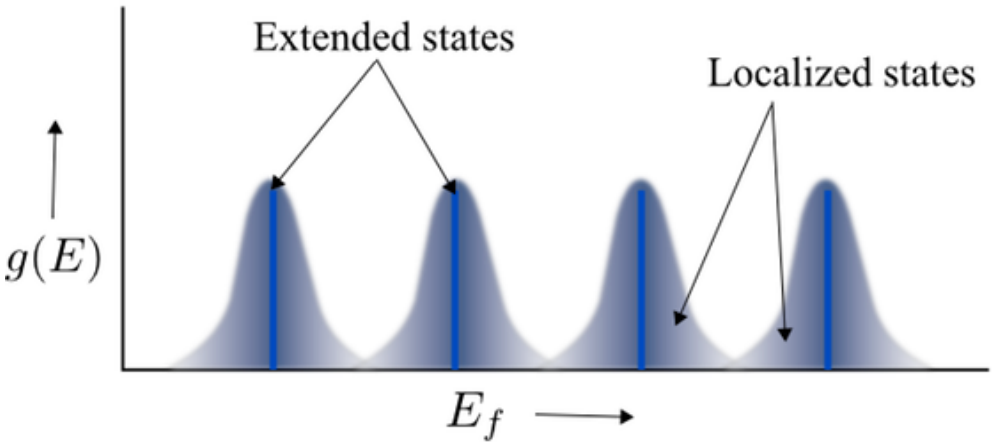

Figure 4.1 Diagram of Landau Levels as a function of the Fermi energy.

$\rho_{xy} = h/ie^2$. Moreover, when the Fermi energy lies exactly at a LL, the states are delocalized and therefore there is charge conduction. This results in a longitudinal resistivity which oscilates when increasing the magnetic field between isolating states ($\rho_{xx} = 0$) and metallic states ($\rho_{xx} \neq 0$). This oscillations are known as Shubnikov de Haas oscillations (SdHO). At the same time, when there is no charge conduction and the 2DEG is in isolating state, the Hall resistivity is quantized. When the longitudinal resistivity increases above zero, the Hall resistivity starts its transition from one plateau to the next one.
Since the isolating states and conductive states correspond to localized and delocalized states (respectively), the transient between two quantum Hall plateaus are in fact localization-delocalization transitions [5, 34]. In figure 4.2 we show the IQHE of a InGaAs/InAlAs quantum well (QW) where the plateaus at filling factor $\nu = 1, 2, 3$ and 4 are observed.

A few years after the discovery of the IQHE, a new kind of quantum Hall effect was found by Störmer and Tsui. What they observed was that 2DEGs with extremely high mobility ($\sim 10^5$ cm^2/Vs) shows an Hall resistance with additional quantized values than that observed by von Klitzing. Particularly, their observations were that besides the integer values of the Hall resistance $\rho_{xy} = h/ie^2$, new quatized plateaus appeared [3]. The first theoretical explanation came in 1983 [35].
The fractional quantum Hall effect refers to a quantized Hall resistivity whose values are given by: $\rho_{xy} = h/fe^2$ where f is a rational fraction in the form: $f = n/(2pn \pm 1)$ and the values related to particle-symmetry in the lowest LL: $f = 1 - n/(2pn \pm 1)$. While the IQHE can be explained of non-interacting electrons, the FQHE cannot be explained following this approach. In fact, the FQHE arises precisely because of the

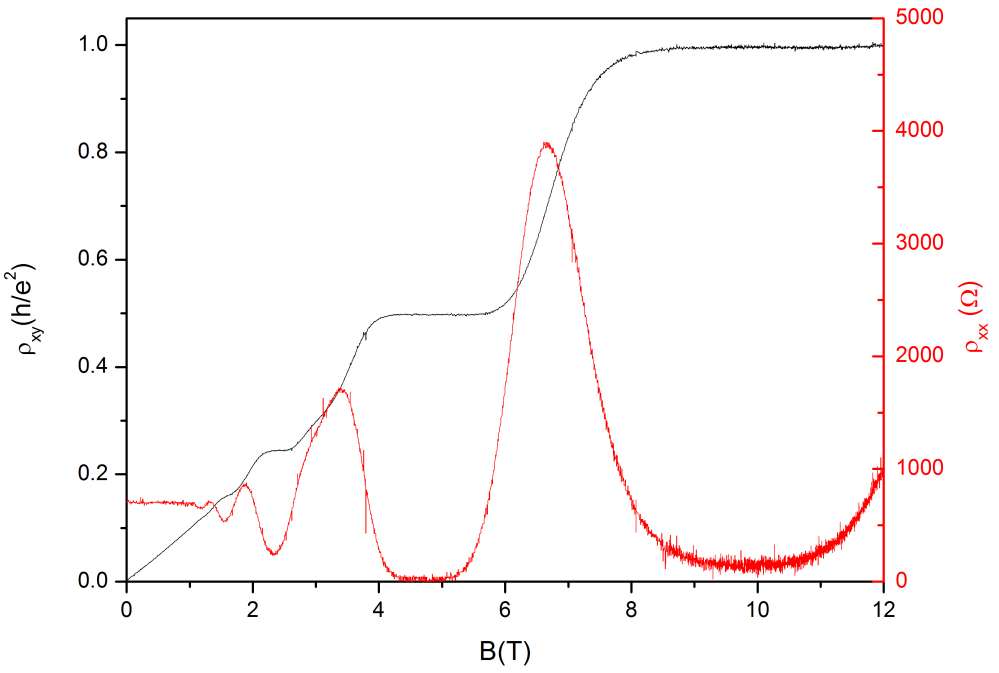

Figure 4.2 IQHE measured at 300 mK in Salamanca. Hall resistivity and longitudinal resistivity (black and red lines respectively) a functions of the magnetic field.The sample was a InGaAS/InAlAs QW with electron density $n = 2.65 \cdot 10^{12}$ cm^{-2} and the mobility $\mu = 33700$ cm^2/Vs .

many body correlations, making thus the FQHE a signature of these true many-body correlations [36, 37].

A deep analysis of the FQHE is beyond the scope of this work, but the interested reader might be referred to Ref. [38] Nonetheless, in figure 4.3 we show some of our measurements taken in Salamanca using our dilution refrigerator (see section 3.1.2) and our superconducting magnet (section 3.2.1). Our data show both the integer plateaus and the fractional plateaus at filling factors $\nu = 1/3, 2/5, 3/5, 2/3, 4/3$ and $5/3$. Both the transient between the plateaus and the SdHO are smoothed when the temperature is increased. Our aim was to study the exotic state $\nu = 5/2$ [39]. However, the mobility of the device under study was too low to observe such state ($\mu = 10^6$ cm^2/Vs) and we were unable to obtain higher mobility devices.

In the next sections we will review the quantum Hall effect in graphene devices, showing the differences between the QHE in graphene and the QHE in 2DEGs.

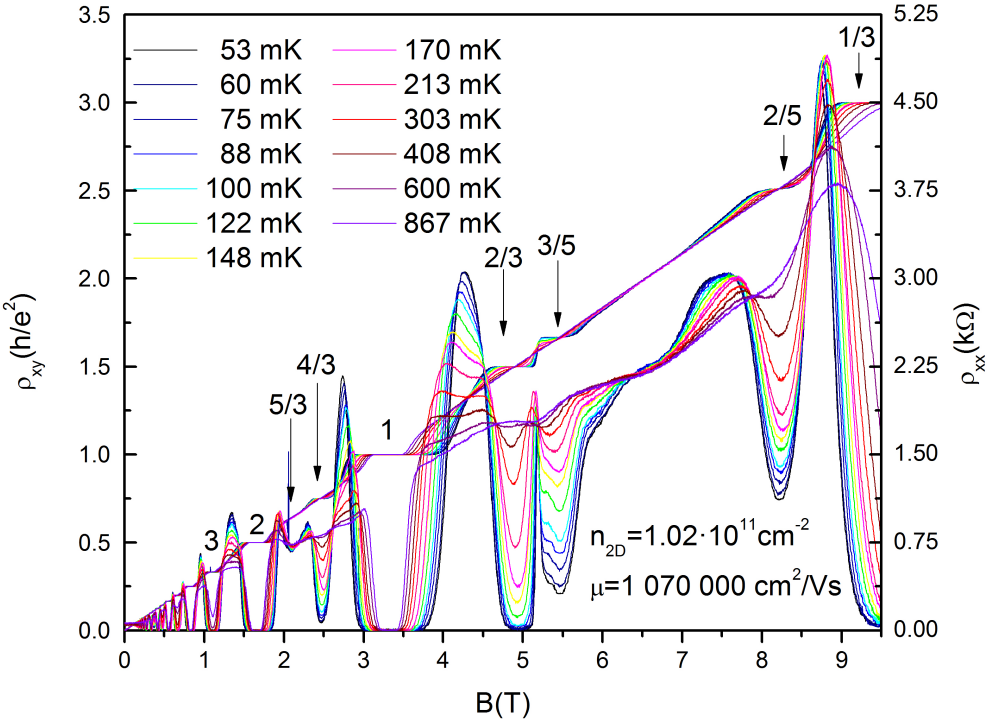

Figure 4.3 FQHE measured in a GaAs/AlGaAs QW at temperatures from 53 mK to 867 mK. We show ρ_{xy} and ρ_{xx} as functions of the magnetic field and their variation with increasing temperature.

4.2 Quantum Hall effect in graphene

We have previously shown the quantum Hall effect as it was known before the discovery of graphene. The QHE in graphene has remarkably different features when compared with the QHE in 2DEGs. In this section we will review the theoretical properties of the QHE in monolayer, bilayer and trilayer graphene.

4.2.1 Quantum Hall effect in monolayer graphene

As said in section 2.1, the band structrure of monolayer graphene is linear [8] at low energies (close to the K and K' points) and there is no gap. As a result, the energy spectrum of the Landau levels follows: $E_n = \pm\sqrt{2e\hbar v_F^2 NB}$ [40], where the $\pm$ signs comes from considering electrons (+) or holes (-) and v_F is the Fermi velocity which has been found to be $v_F \sim c/100$, being c the speed of light [15].

Notice how this spectrum results in a much larger separation between two adjacent Landau levels than the energy of Zeeman spin splitting, resulting in a fourfold degeneracy

(spin and K and K' degeneracy) which can be broken using very high magnetic fields. This fourfold degeneracy implies that the distance between two plateaus is $\Delta\sigma_{xy} = 4e^2/h$. Nonetheless, the quantum Hall effect has been referred to as "anomalous" quantum Hall effect, since the quantum Hall plateaus do not follow the expected series of values $\sigma_{xy} = \pm 4ne^2/h$ but instead follow $\sigma_{xy} = 4(n+1/2)e^2/h$ [13]. The half integer shift is caused by the fact that there are two Dirac cones which share the zero mode, making the degeneracy to be shared by electrons and holes at the same time. As a result, there is a shift of 1/2 in the quantum Hall sequence. The expected values for the IQHE for monolayer graphene with unbroken degeneracies (valley and spin) are thus those at filling factor: $\nu = \pm 2, \pm 6, \pm 10, \ldots$

If the zeroth mode degeneracy is broken, plateaus at filling factors $\nu = 0, \pm 1$ [18, 41] are observed. Nonetheless, in order to break the degeneracy very high magnetic fields are needed. Also, when the mobility of the graphene device is high enough the fractional quantum Hall effect can also be observed [42, 43].

Before starting this Thesis, Amado *et al.* had investigated the localization-delocalization transitions in the quantum Hall regime using a monolayer graphene device tailored in a Hall bar geometry [44, 45]. We aimed to extend the study of the plateau-plateau and plateau-insulator transitions in Corbino rings in order to study the role of the edge currents. Unfortunately, the fabrication of such devices requires the sputtering of an additional dielectric layer or the fabrication of an air bridge in order to bond the inner contact, and none of the fabricated devices worked satisfactorily.

4.2.2 Quantum Hall effect in bilayer graphene

If monolayer graphene can be described as a planar structure of carbon atoms in a honeycomb lattice (see section 2.1), bilayer graphene can be described as a planar structure of carbon atoms arranged in *two* honeycomb lattices, one above the other. The most common arrangement is known as AB stacked bilayer [46] graphene, shown in figure 4.4. The other possible stacking is called AA stacked bilayer graphene [47] and its difference from AB stacked graphene is that there is no relative horizontal displacement between the two layers, being the carbon atoms of one layer right above the atoms of the other layer.

The band structure of AB bilayer graphene is shown in figure 4.4 and is similar to that of monolayer graphene, with the addition of one parabolic conduction subband and one parabolic valence band. Also, though there is still no gap, the dispersion relation is no longer linear close to the K and K' points, but parabolic instead.

As a consequence, when a magnetic field is applied eigenvalues of the Landau levels have an energy $E_N = \pm\hbar\omega_c\sqrt{N(N-1)}$ [49, 50], where ω_c is the cyclotron energy $\omega_c = eB/m^*$.

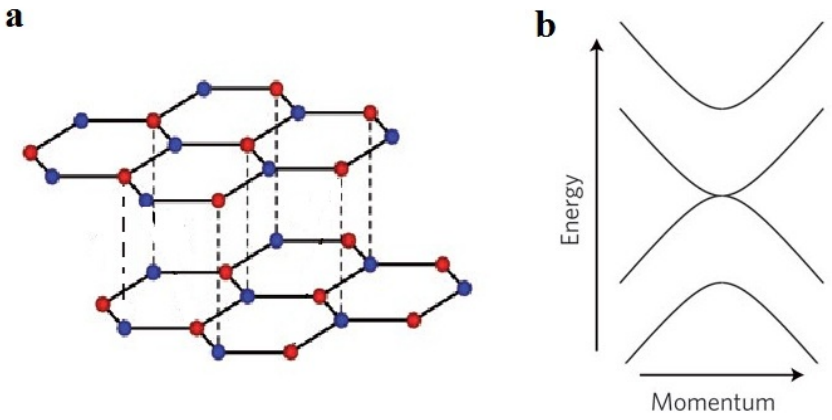

Figure 4.4 (a) Lattice structure of AB bilayer graphene. Atoms of different colours belong to different triangular sublattice of each honeycomb lattice. (b) Energy dispersion at the K and K' points of bilayer graphene at low energies. Image adapted from Ref. [48].

Thus, there are two states ($N = 0$ and $N = 1$) which have zero energy. As a consequence, the zero energy level will have an eighfold degeneracy: spin degeneracy, valley degeneracy and the two states with zero energy. Nonetheless, since there are two LL having the same energy, the 1/2 shift observed in monolayer graphene disappears, and the observed behaviour in the Hall conductivity when passing through $\nu = 0$ (from $\nu = -4$ to $\nu = +4$ or viceversa) is just a step twice bigger than the step of $4e^2/h$ caused by the fourfold degeneracy of the rest of the LL [49]. However, if the symmetry is broken, additional plateaus than those given by $\nu = \pm 4, \pm 8 \pm 12 \ldots$ are observed [51].
In figure 4.5 we show the IQHE for a bilayer graphene device on a Si/SiO_2 substrate as a function of the magnetic field. Precise quantization of the Hall resistivity (black line) at values $\rho_{xy} = h/4\nu e^2$ is observed for values of $\nu = 1, 2, 3$. Plateaus at higher filling factors are not completely developed, but clear hints of their existence are seen in the behaviour of ρ_{xy} in form of changes of the slope. Accordingly, for each plateau in ρ_{xy} (both developed and non developed) there is a minimum in the longitudinal resistivity ρ_{xx}.
Further details on the information that we can extract from the quantum Hall effect will be given in section 4.3.

4.2.3 Quantum Hall effect in trilayer graphene

The thickness of our graphene devices can be further increased by adding another graphene layer. This is known as trilayer graphene. In this case, there are two possible stackings: ABC and ABA stacked graphene [52] (shown in figure 4.6).

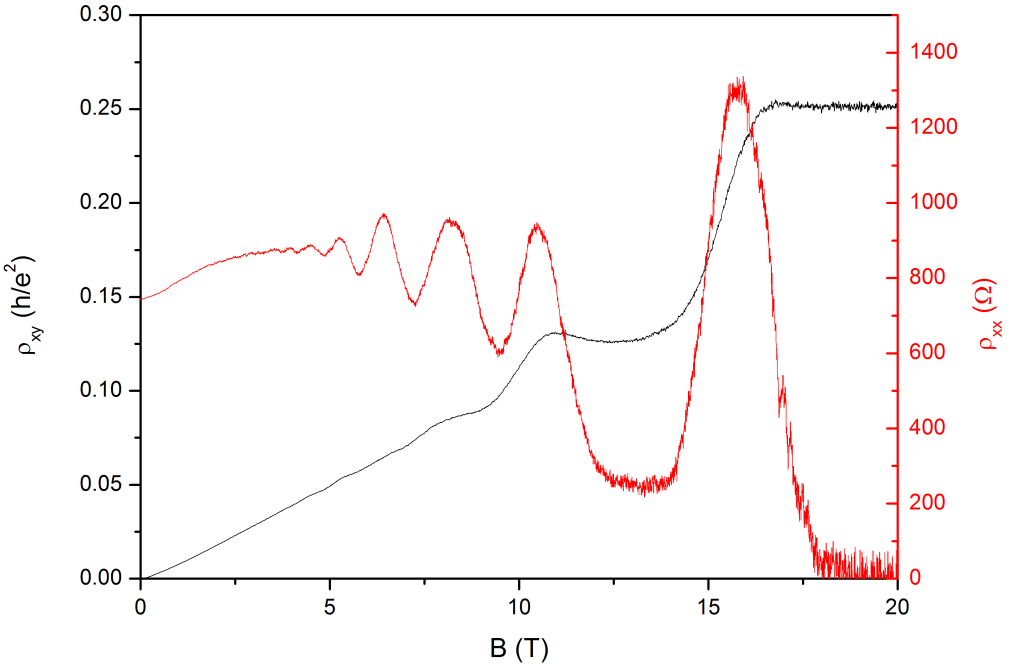

Figure 4.5 Measurements of the QHE using a bilayer graphene device on top of Si/SiO_2 at 4.2 K. The black line shows ρ_{xy} as a function of the magnetic in units of h/e^2. The quantum Hall plateaus are seen at values $\rho_{xy} = 1/4e^2, 1/8e^2, 1/12e^2$ and some more plateus are seen though they are not fully developed. Red line shows ρ_{xx} as a function of the magnetic field.

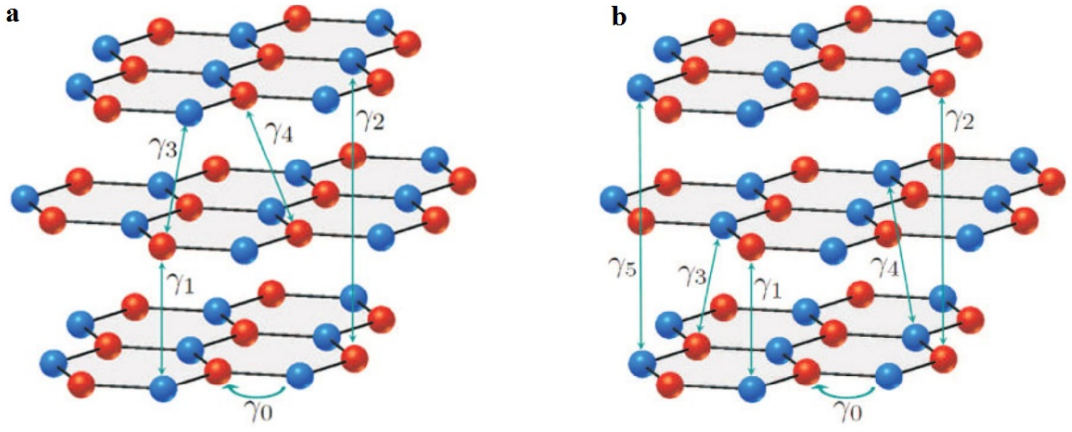

Figure 4.6 Lattice structure of ABC (a) stacked graphene and ABA (b) stacked graphene, adapted from Ref. [52].

These two possible stacking arrangements result in two different quantization band structure. At low energies, ABA trilayer graphene has two bands (conduction and valence) with linear dispersion and no gap, with addicional parabolic subbands without gap [26], whereas ABC trilayer graphene has a qubic dispersion relation. Thus, the quantization of ρ_{xy} will result in two different sequences of quantum Hall plateaus. As a consequence, the quantum Hall effect probes to be a powerful tool to determine the stacking of a trilayer graphene device.

4.3 Characterization of the devices by magnetotransport measurements

As discussed previously (section 4.2), the different sequence of the plateaus observed when varying the magnetic field can be seen as a consequence of the band structure of the material.
Another consequence of the band structure would be the so called Dirac peak. Let's imagine that the Fermi energy can be altered by applying an gate voltage to the sample. If the Fermi energy lies precisely at the point at which the two cones of the band structure touch, the valence band will be completely filled and the conduction will be empty. In standard semiconductors this gate voltage effect would result in a diverging resistivity, but in graphene, due to the linear dispersion, it results in a maximum of the resistance. This maximum is known as Dirac peak and the maximum resistivity has a value $h/4e^2 = 6.45$ k Ω[15].
Ideally, the Dirac peak (also known as charge neutrality point) would appear at a zero gate voltage, thus decreasing when voltage is applied. However, this is the case in which no unintentional doping occurs. Usually, water or other (*e.g.* acetone) adsorbants are found in the surface of graphene, resulting in a shift of the position of the Dirac peak. These adsorbants can be removed by injecting a high current density along the device [53] or thermally annealing the sample [54].
As the gate voltage is set closer to the charge neutrality point, the available states are less than when the Fermi energy lies well far away from the charge neutrality point. This allows us to modify both the density of carriers and their nature (hole like or electron like) but just increasing or decreasing the gate voltage and passing through the Dirac peak.

The density can be derived from the gate voltage as follows. We can assume that our graphene device is a planar capacitor made of two planar conductors (graphene and p-doped silicon) separated by a layer of dielectric (SiO_2) as shown in figure 4.7. By

applying a voltage, an electric charge is induced, resulting in a density proportional to the gate voltage:

$$n = \epsilon \left(V_g - V_D\right) / ed = \alpha \left(V_g - V_D\right) \tag{4.1}$$

Here ϵ is the dielectric constant of SiO_2 (or the dielectric material), e is the charge of the electron, d is the thickness of the SiO_2 layer (~ 300 nm) and V_g and V_D are the gate voltage and the voltage at which the Dirac peak is found, respectively.
Our usual procedure nonetheless was rather different. From the Hall measurements (either quantum or classical) we can obtain the density from the dependence of ρ_{xy} on the magnetic field at low B. Since, at low B,ρ_{xy} (in the QHE) varies linearly with B [33] (and indeed in the classical Hall effect ρ_{xy} is linear for all B [55]) following $\rho_{xy} = B/ne$; the density can be extracted as: $n = \frac{1}{e}\left(\frac{\mathrm{d}\rho_{xy}}{\mathrm{d}B}\right)^{-1}$.
Therefore, measuring the Hall effect at different gate voltages and deriving the density from each one of these measurements gives as a set of (n, V_g), fitting this data accordingly to equation 4.1 allows us to obtain accurately the voltage of the charge neutrality point V_D and the ratio ϵ/d, as well as the density for any given gate voltage.

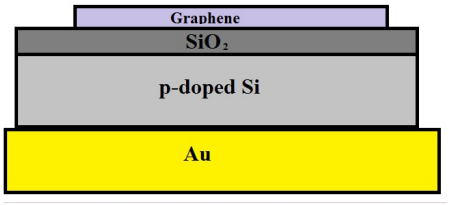

Figure 4.7 Sketch of a side view of a graphene device. The gold in the bottom is thick gold layer of our DIL sockets to which the graphene device is glued using conductive silver paint (section 2.3.6 of Chapter 2).

Once the density and the resistivity at zero magnetic field have been obtained, we can use Drude's formula for the conductivity in order to know the Hall mobility of the sample: $\sigma_{xx} = \mu ne \implies \mu = 1/(ne\rho_{xx})$ [55].
The FET (field effect transistor) mobility can also be inferred by studying the dependence of the conductivity with the gate voltage. Since $\sigma = \mu ne$ and $n = \alpha(V_g - V_D)$, we obtain: $\sigma = \mu e\alpha \left(V_g - V_D\right)$. The FET mobility can be thus obtained as: $\mu = \frac{1}{e\alpha}\frac{\mathrm{d}\sigma}{\mathrm{d}V_g}$.

In the next section we will show our results regarding the QHE in bilayer graphene and trilayer graphene on Si/SiO_2 and the characterization of these devices.

4.4 Results on the quantum Hall effect in bilayer and trilayer graphene

We have reviewed in sections 4.2.2 and 4.2.3 the theoretical properties of the QHE in bilayer and trilayer graphene and explained the method we have used to extract valuable information from these measurements. In this section we will show our results on the QHE in bilayer and trilayer graphene on Si/SiO_2 .

4.4.1 Results on the QHE in bilayer graphene

Besides extending the study of the localization-delocalization transitions performed by Amado *et al.* [44, 45] using monolayer Corbino rings, we also wanted to understand this transitions in bilayer graphene devices.

We studied a bilayer graphene device (called N11 and shown in figure 4.8) tailored in the geometry of a Hall bar with a channel of width $W = 10$ μm.

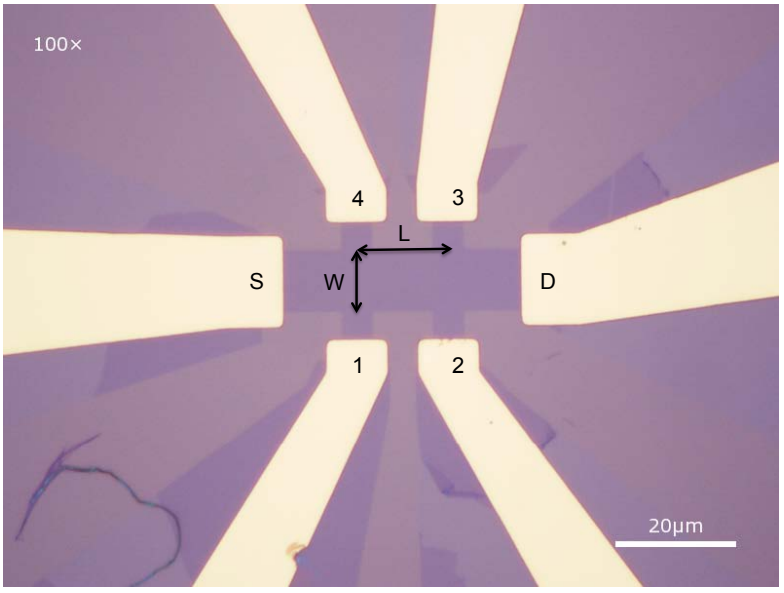

Figure 4.8 Optical image of the sample N11 after being processed.

In the following, we will define the Hall resistivity ρ_{xy} as the resistivity deriving from measuring the voltage drop in the direction perpendicular to the direction of the current and the longitudinal resistivity ρ_{xx} is the resistivity measured by knowing the voltage drop between two contacts aligned in the same direction of the current. Therefore, if a

current i is injected from the source S to the drain D in figure 4.8, we define ρ_{xy} [55] as

$$\rho_{xy} = (V_4 - V_1)/i = V_{41}/i$$

Obviously, we can also define $\rho_{xy} = V_{32}/i$. The longitudinal resistivity is measured in a similar way [55], but the ratio between the distance separating the contacts L at the same side and the width W of the sample must be considered. The longitudinal resistivity is defined as:

$$\rho_{xx} = \frac{(V_4 - V_3)/L}{i/W} = \frac{V_{43}}{i}\frac{W}{L}$$

Again, the longitudinal resistivity can also be obtained as $\rho_{xx} = (V_{43}/i)(W/L)$.

The sample was cooled down at 2 K and the voltage drop between pairs of contacts using several lock-in amplifiers. The excitation current was 10 nA and a gate voltage was applied with a sourcemeter.
We measured ρ_{xx} sweeping the gate voltage at zero magnetic field. As we can see in figure 4.9, the Dirac peak was found to be at $V_D = 25.6$ V. This suggests that high unintentional doping occured. Unfortunately, thermal annealing [54] in vacuum wasn't possible above 100 °C and the impurities couldn't be evaporated.

The resistivities ρ_{xy} and ρ_{xx} were measured at different densities (changed by means of the gate voltage) using the magnetic field as driving paramenter.

From the slope of ρ_{xy} at low B we extracted the carrier density (red squares in figure 4.9) and fitted our data with respect to eq. 4.1 (see red line in fig. 4.9). We obtained $\alpha = 7.02 \cdot 10^{14}$ V/m^2 and $V_D = 25.6$ V.
From our data of ρ_{xx} at different gate voltages (and thus, at different densities) we extracted the Hall mobility by exploiting the relation $\mu = (ne\rho_{xx})^{-1}$. The mobility as a function of density is shown in figure 4.11.

Since we wanted to study the plateau-plateau and plateau-insulator quantum phase transitions (see Chapter 5), but the high density of dopants resulted in a high inhomogeneity along the sample. As said before, vacuum annealing was not an option, therefore we tried current annealing [53]. We increased the current injection through the device in order to evaporate or drift the impurities. Nonetheless, the current annealing did not improve the quality of the sample (noticeable by the shift of the Dirac peak) but furthermore, the current density was higher than the breaking current density of graphene, and it resulted in the break of the device.

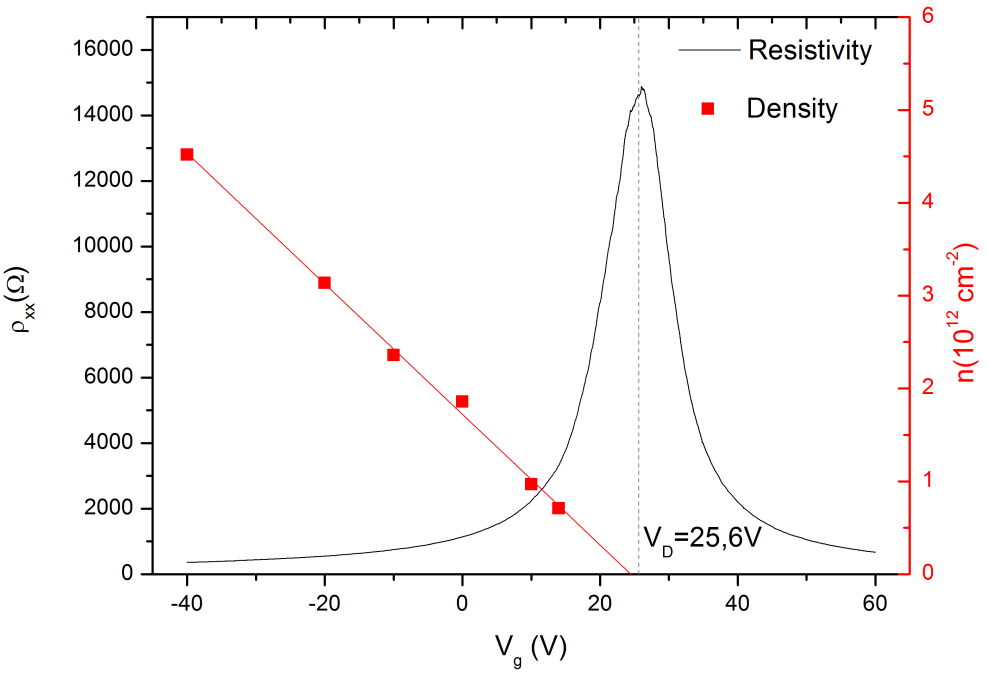

Figure 4.9 Black line shows ρ_{xx} as a function of the gate voltage at 0 T and 4.2 K. Red squares show the density as a function of the gate voltage (obtained from the Hall measurements shown in Fig. 4.10(a)). Image adapted from Ref. [56].

After breaking this device we tried to fabricate more bilayer graphene samples, but unfortunately, most of our bilayer graphene devices showed a large inhomogeneity or broke whilst doing the experiment. In order to avoid the carrier density inhomogeneity, we tried to obtain a bilayer graphene device on top of *h*-BN . This kind of devices, as we have seen, enhances the mobility and reduces inhomogeneities. After several attempts, we finally obtained such device (shown in figure 5.1), which was covered with and additional *h*-BN flake in order to avoid contamination over time due to the exposure of ambient conditions. This device showed very high mobility and low inhomogeneities, and we could study the localization-delocalization transitions showed in Chapter 5.

4.4.2 Results on the QHE in trilayer graphene

In parallel with the study of the quantum phase transitions in bilayer graphene systems, we also wanted to study the quantum Hall effect in trilayer graphene. At that time, the existence of quantum Hall effect in trilayer graphene was under debate. The results presented here were obtained in December of 2010, and the observation of the quantum Hall effect in trilayer graphene had not been reported yet. Nonetheless, whilst writing the manuscript of the report showing our results [58] and discussing the importance of

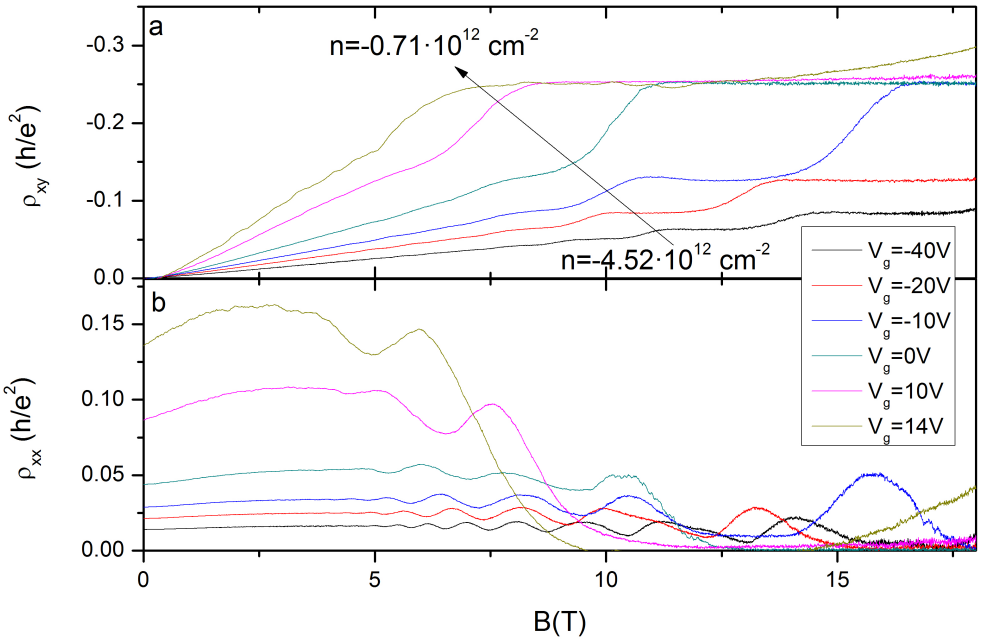

Figure 4.10 (a) ρ_{xy} as a function of the magnetic field at T=2 K and at different gate voltages. The plateau sequence $\nu \pm 4, \pm 8, \pm 12, \ldots$ can be observed. From the slope of ρ_{xy} at $B < 1$ T the density was extracted. (b) Shows ρ_{xx} as a function of the magnetic field at 2 K and different gate voltages. We can observe the SdHO in which for each plateau in ρ_{xy} there is a minimum. Image adapted from Ref. [57]

our data with experts on graphene as F. Guinea and L. Brey, Taychatanapat reported the quantum Hall effect in trilayer graphene observed in an outstanding sample [26].

The device we used, shown in figure 4.12, was a trilayer graphene device on top of SiO_2 and it had been tailored in the geometry of a Hall bar.

The number of layers of this sample had been characterized by optical contrast measurements [16] and Raman spectroscopy [59]. The Raman scattering spectrum was measured at the Universitá degli Studi di Pavia at room temperature. We used a microRaman setup with laser light excitation at 1.96 eV with $\sim$ 10 mW/mm^2 power density. We used 50X and 100X objectives, with a corresponding laser spot area of approximately 4 μm^2 and 1 μm^2, respectively. The spatial resolution of the setup in the xy plane was approximately 1 μm. (see figure 4.13).

The sample was cooled down to 2 K and we tried to measure ρ_{xx} as a function of the gate voltage. Nonetheless, the dielectric (SiO_2) separating the graphene flake from the p-doped silicon wafer appeared to be broken, resulting in the leak of current ($i_{leak} > 10$ nA) from the silicon wafer into the graphene device.

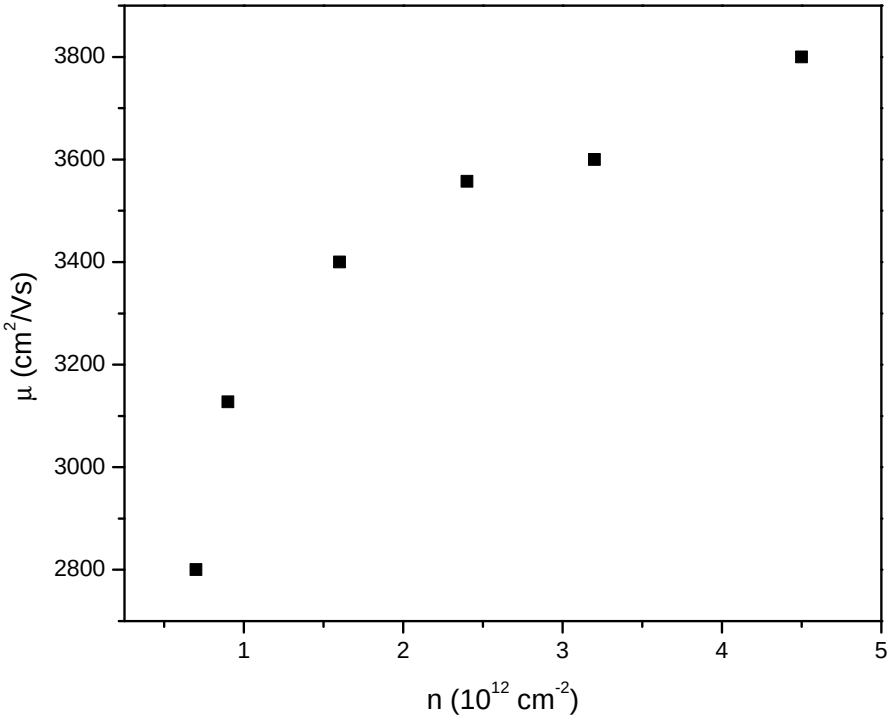

Figure 4.11 Mobility as a function of density for our bilayer graphene device N11.

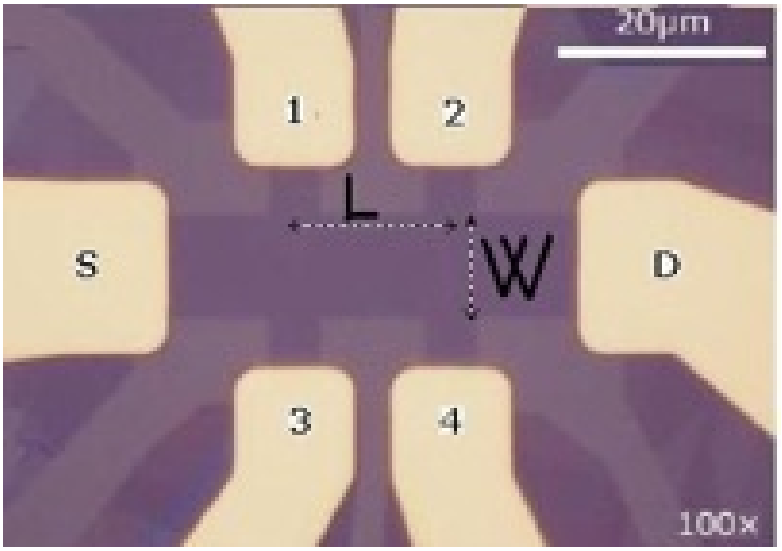

Figure 4.12 Optical image of the trilayer graphene device N33.

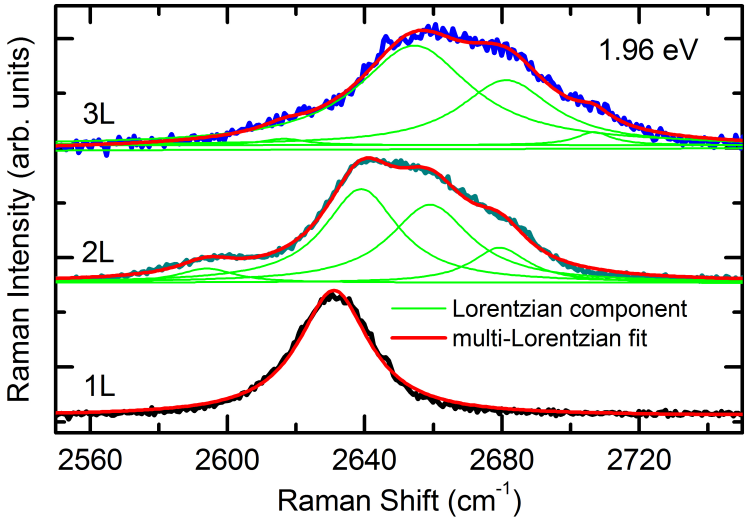

Figure 4.13 Raman spectrum of the device under study and the comparison of the 2D band of bilayer and monolayer graphene. Red lines represent the multi Lorentzian fits as the convolution of singular Lorentzian (green lines).

As a consequence, we were unable to change the density of this device and we studied the QHE as a function of the temperature.
We used the four Hall contacts (1,2,3 and 4 in figure 4.12) to measure ρ_{xx} and ρ_{xy}. We will thus refer to ρ^t_{xx} ("top") to the resistivity measured using the contacts 1 and 2 ($\rho^t_{xx} = (V_{12}/i)(W/L)$) and ρ^b_{xx} ("bottom") to that measured using the contacts 3 and 4. Equivalently, we measured two Hall resistivities: ρ^l_{xy} ("left") and ρ^r_{xy} ("right") as $\rho^{l(r)}_{xy} = V_{13(24)}/i$.

We observed two important things. First of all, the two ρ_{xy} were strongly different: ρ^l_{xy} had a higher slope and showed a plateau of value $\rho^l_{xy} = h/6e^2$; whereas ρ^r_{xy} had a lower slope and showed no quantized value. Second of all, and strikingly, none of the longitudinal resistivities are symmetric with the magnetic field. In fact, not only $\rho_{xx}(B) \neq \rho_{xx}(-B)$ (either "top" or "bottom") but what we find is that, when reversing the magnetic field, one ρ_{xx} is symmetric with respect to the other one; *i.e.* $\rho^t_{xx}(B) = \rho^b_{xx}(-B)$ and $\rho^b_{xx}(B) = \rho^t_{xx}(-B)$, as shown in figure 4.14.

This striking feature can be explained as follows. From the slope of ρ^l_{xy} at low magnetic field we extract a density $n^l = 6.43 \cdot 10^{12}$ cm^{-2}, whereas from the slope of ρ^r_{xy} we get a density $n = 2.04 \cdot 10^{12}$ cm^{-2}. Thus, the sample is highly inhomogeneous since the carrier density along the sample varied by a factor of 3. This gradient in the carrier density, combined with the magnetic field, induces a non uniform accumulation of charge carriers

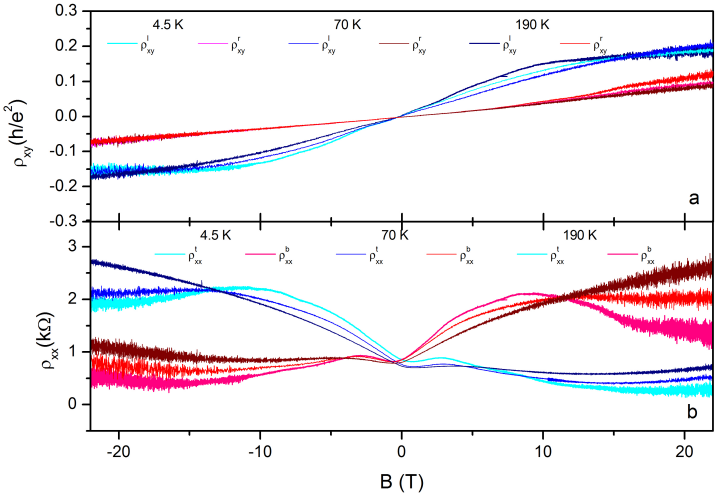

Figure 4.14 (a) ρ^r_{xy} (blueish lines) and ρ^l_{xy} (reddish lines) as function of the magnetic field at selected temperatures. ρ^r_{xy} develops the $\nu = \pm 6$ plateau whereas ρ^l_{xy} does not. (b) Isotherms of ρ^t_{xx} (blueish lines) and ρ^b_{xx} (reddish lines) versus the magnetic field. As explained in the text, $\rho^{t(b)}_{xx}(B) \neq \rho^{t(b)}_{xx}(-B)$ but $\rho^{t(b)}_{xx}(B) \neq \rho^{b(t)}_{xx}(-B)$. Adapted from Ref. [58].

at the boundaries of the sample, and as a result the current density is spatially inhomogeneous.

Let's name ρ_{xx} and ρ_{xy} the resistivies which would be measured if there were no inhomogeneity. If there is a density gradient, the measured resistivities can be written in terms of the "ideal" (*i.e.* unaffected by the inhomogeneity) as [60]

$$\rho^{t,b}_{xx} = (\rho_{xx} \pm \rho_{xy}\beta\frac{W}{2}) = \frac{L}{W}R^{t,b}_{xx} \tag{4.2a}$$

$$\rho^{l,r}_{xy} = \rho_{xy}(1 \mp \beta\frac{L}{2}) = R^{l,r}_{xy} \tag{4.2b}$$

Here β is a phenomenological parameter that depends evenly on the magnetic field and the temperature. From eqs. 4.2a and 4.2b we get: $\Delta R_{xx} = R^t_{xx} - R^b_{xx} = R^r_{xy} - R^l_{xy} = \Delta R_{xy} = \Delta R$.

If the sample is homogeneous, $\Delta R = 0$, but a density gradient implies that $\Delta R \neq 0$, as shown in figure 4.15.

Since, for $B \gtrsim 0$, $\rho_{xy} = B/ne$, we can calculate βL as $\beta L = 2(n^l - n^r)/(n^l + n^r)$. Since $n^l = 3n^r$, $\beta L \approx 1$, the gradient density is of the same order than the mean carrier density. According to eq. 4.2a, the "true" longitudinal resistivity can be calculated as an average

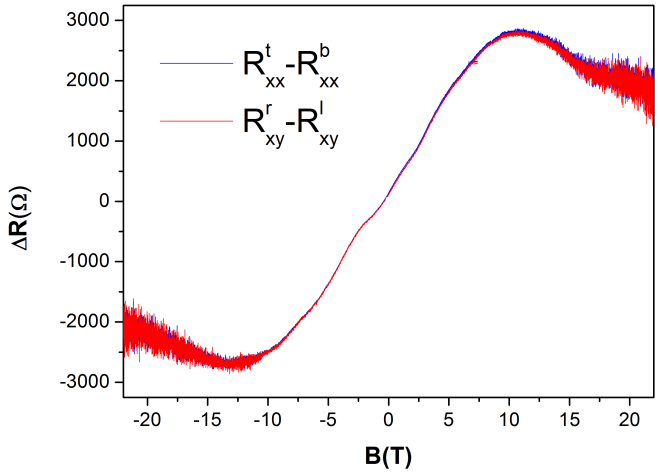

Figure 4.15 Difference between the two longitudinal resistances (blue) and between the Hall resistances (red). The overlapping is evident, confirming the hypothesis of density gradient.

of ρ^t_{xx} and ρ^b_{xx}, which is equivalent to taking only the symmetric part of the resistivity:

$$\rho_{xx}(B) = \frac{\rho^t_{xx}(B) + \rho^b_{xx}(B)}{2} = \frac{\rho^{t(b)}_{xx}(B) + \rho^{t(b)}_{xx}(-B)}{2}$$

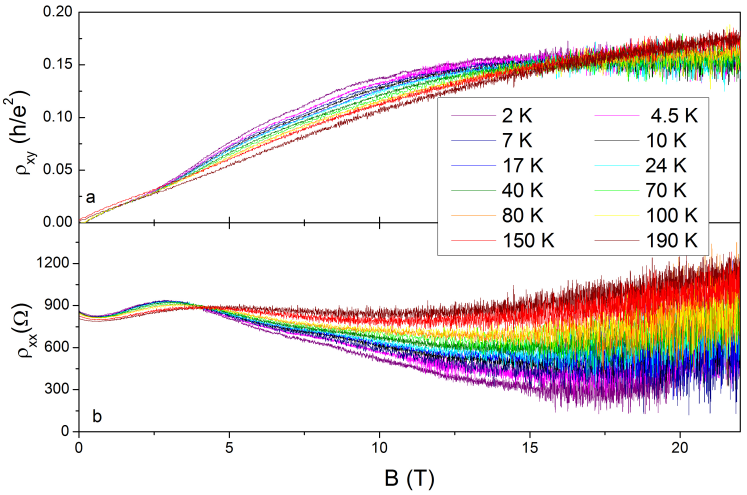

Figure 4.16 Isotherms of ρ_{xy} and ρ_{xx} (a and b respectively) as functions of the magnetic field.

We cannot follow this same approach for the Hall resistivities, since the difference between the two sides of the Hall bar is too big and is equivalent to having two effective regions. Thus, we can continue our analysis referring to ρ^r_{xy} as the Hall resistivity under analysis and ρ_{xx} as the average of ρ^t_{xx} and ρ^b_{xx}. The isotherms of ρ_{xy} and ρ_{xx} are shown

in figure 4.16, (a) and (b) respectively. We can see in figure 4.16(a) that at $B \sim 14$ T the $\nu = 6$ starts developing, and at higher B, ρ_{xy} is indeed quantized at $\rho_{xy} = h/6e^2$. At $B \sim 3$ T the SdHO start, indicating a mobility of the order of $(\mu B \sim 1)$ $\mu \sim 3300$ cm^2/Vs

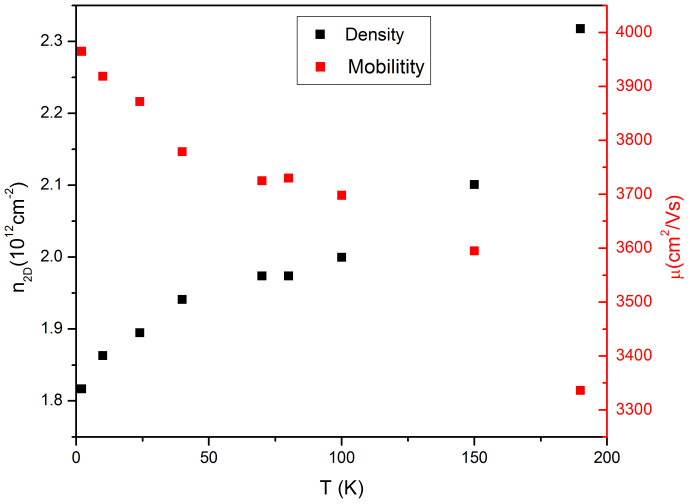

Figure 4.17 Density (black squares) and mobility (red squares) as function of the temperature. The density increases with the temperature, as expected from a semimetal.

Indeed, the density and the mobility can be extracted as explained previously (see section 4.3. The density and the mobility as a function of the temperature are shown in figure 4.17.

From these resistivities, we can obtain the conductivities $\sigma_{xx} = \rho_{xx}/(\rho_{xx}^2 + \rho_{xy}^2)$ and $\sigma_{xy} = \rho_{xy}/(\rho_{xx}^2 + \rho_{xy}^2)$. In figure 4.18 we show the isotherms of σ_{xy} (a) and σ_{xx} (b) as a function of the magnetic field. Figure 4.18(a) shows that the Hall conductivity is quantized at filling factor $\nu = 6$, as expected for ABA trilayer graphene. Also, when the $\nu = 6$ plateau starts developing, σ_{xx} decreases with the magnetic field, reaching a minimum at $\sigma_{xx} \sim 0$, revealing thus the SdHO even for such inhomogeneous sample.

4.5 Four layered graphene

A reasonable question to ask would be: “for how long can we keep on adding layers until the system stops behaving as a bidimensional material?"
We attempted to add more information to this issue by measuring the quantum Hall effect in a four layered graphene nanodevice, shown in figure 4.19.

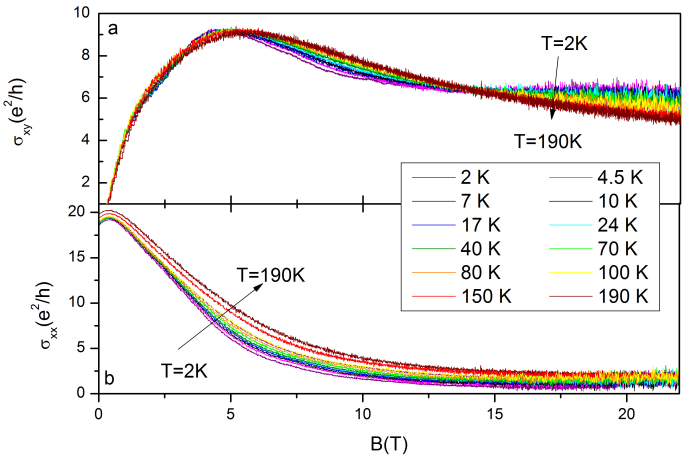

Figure 4.18 Isotherms of σ_{xy}(a) and σ_{xx}(b) as functions of the magnetic field. Figure adapted from Ref. [57].

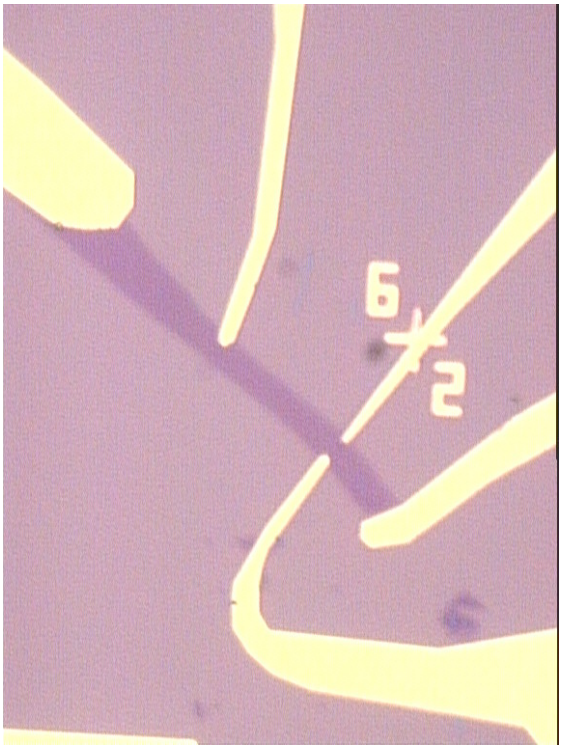

Figure 4.19 Optical image of the four layered graphene nanodevice under study in the geometry of a Hall bar.

First of all, the back gate voltage was swept and the Dirac peak was found to be at ~ 130 V, as shown in figure 4.20(a). After that, the magnetic field was swept at different densities, changed by applying different gate voltages. Though no clear quantization of the Hall resistance was observed, a clear ambipolar effect (*i.e.*, the ability to change from hole-like regime to electron-like regime) is clearly evidenced by the opposite signs of the Hall resistance when the gate voltage passes through 130 V (see figure 4.20(b)).

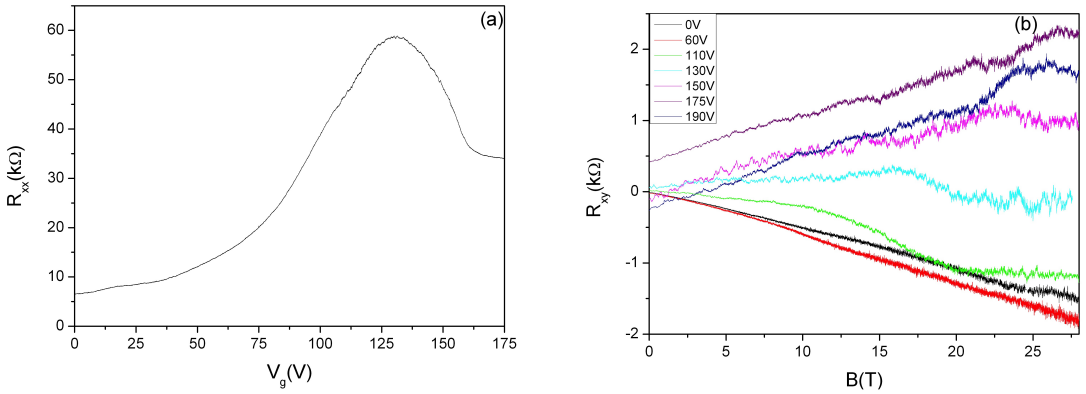

Figure 4.20 (a) Longitudinal resistance as a function of the gate voltage at 1.2K, showing the Dirac peak at 130 V. (b) Hall resistance as function of the magnetic field at different gate voltages and at $T = 1.2$ K. There are to observable regimes, those with $V_g < V_D$ with negative slope of the Hall resistance, and those with $V_g > V_D$, characterized by a positive slope.

4.6 Summary and conclusions

In this Chapter we have reviewed the integer quantum Hall effect and explained how the number of layers in graphene affects the quantization of the Landau levels.
We have then explained how information on the density and mobility can easily be extracted from the magnetotransport measurements and we have used this method for one bilayer device and one trilayer device. Moreover, we have shown that some useful data can be extracted even for highly inhomogeneous samples who also lack a back gate.

Chapter 5

Quantum phase transitions in bilayer graphene

In this section we investigate several plateau-plateau transitions at different carrier densities at temperatures varying in three orders of magnitude. We have found a non universality of the critical exponent for all the investigated transitions, which are compatible with a percolation scenario.

5.1 Introduction

A classical phase transition can be described as the transient from one state to another governed by thermal fluctuations. Nonetheless, when the temperature of the system aproaches $T = 0$ such fluctuations are no longer the cause of the transition, but an external parameter is required. These transitions which occur at the quantum limit of $T = 0$ and that are caused by a parameter other than the temperature are known as quantum phase transitions (see, for example Ref. [61] and references therein).
In the framework of the quantum Hall effect the first transition to appear is a metal-insulator transition. As explained in section 4.1, the existence of a plateu in ρ_{xy} and/or the existence of a minimum in ρ_{xx} is a consequence of the fact that all the states are localized, whereas in the transient from one plateu to another (or from one minimum in ρ_{xx} to the next one) the states are delocalized. This transition is governed by the sweeping of the energy of the Landau levels across the Fermi energy. Thus, the transition from localized states to delocalized states is a quantum phase transition governed by the energy [5].
At finite temperatures the Landau levels are broadened as a consequence of the thermal fluctuations, but as the temperature is decreased, the Landau levels are narrowed. There should be a way to understand how the transitions would take place at $T = 0$. In fact, there is a scaling law which allows us to express the localization length in terms of the energy [61–64]:

$$\xi \propto |E - E_c|^{-\gamma} \tag{5.1}$$

Where E_c is the critical energy and γ is the critical exponent of the transition. Obviously, the experiments of the QPT have been studied at finite temperatures, and as a result the Landau levels are broadened. Nonetheless, by means of the scaling law the behaviour of the transition can be studied and the quantum limit $T \to 0$ can be understood.
The first experimental observation of the plateau-plateau quantum phase transition was done by Tsui *et al.* in 1986 [4] and confirmed in 1988 [62] with the measurement of the critical exponent of the transition following the theoretical study of Pruisken [63]. They studied the plateau-plateau transitions using a InGaAs-InP heterostructure. They observed that the maximum of the derivative of ρ_{xy} with respect to the temperature followed [62]

$$\left(\partial\rho_{xy}/\partial T\right)_{max} \propto T^{-\kappa} \tag{5.2}$$

Following Pruisken [63], this power law is in fact a consequence of the divergence of ξ when varying the energy near the critical energy. In fact, the exponent κ obtained by Tsui *et al.* in the temperature scaling form can be related to γ by means of $\kappa = p/2\gamma$ [63], where p is the exponent which relates the coherence length dependence on the temperature as a consecuence of the inelastic scattering processes [63], *i.e.,*

$$L_\phi \propto T^{-p/2} \tag{5.3}$$

The value of κ was measured for the first time by Tsui *et al.*, where $\kappa = 0.42 \pm 0.04$ was obtained [62]. This value has been reproduced in studies which extended the temperature regime to the miliKelvi [65]. It has been accepted that $\kappa = 0.42$ must be a universal value in plateau-plateau transitions in the framework of the Anderson model, in which the disorder is mainly short range disorder. Nonetheless, it has recently been shown that in conventional two dimensional electron gases the exponent κ is not universal. Li *et al.* have observed that changing the concentration of Al in AlGaAs/InGaAs results in different values of κ. This means that the Anderson model is no longer valid in systems with long range disorder. In fact, systems with long range disorder are better described by the Chalker-Coddington model [66].

The discover of graphene paved the way to new studies concerning the universality of the quantum phase transitions. Until the discovery of graphene the studied systems were mainly 2DEGs in which the electrons were confined in a quasibidimensional space. With the coming of graphene it is possible to study real bidimensional electron gases. Also, it is now possible to investigate the plateau-plateau transitions using either the carrier density or the magnetic field as driving parameters. Furthermore, the possibility to tune the sign of the carriers (either holes or electrons) by changing the back gate voltage allows further control in the conditions of the experiment.

Nonetheless, controlling the disorder in graphene is not an easy task due to the techniques used in its fabrication. Several measurements can be made in order to distinguish some quality factors of the devices. The proximity of the charge neutrality point and the absence of weak localization is thought to indicate a low level of dopant impurities, whilst the narrowness of the Dirac peak indicates a low inhomogeneity and a high mobility. A Dirac peak far away from 0 V or a strong weak localization signal are usual hints which help to identify samples with high disorder caused by charged impurities, effects of the substrate and corrugation or strain [67]. As a result, it is difficult to know *a priori* what the main mechanism of disorder are present in each graphene device, and thus the effect of the disorder in the quantum Hall regime in graphene is far from being completely understood.

Actually, just a few studies investigating the quantum phase transitions in graphene have

been reported. Giesbers *et al.* [68] studied the plateau-plateau transitions in monolayer graphene on Si/SiO_2 in which they obtained both κ and γ. They changed the Fermi energy by changing the density via the back gate voltage instead of sweeping the magnetic field. At constact magnetic field, they extracted a scaling power law similar to that of eq. 5.2. Namely, they extracted $\partial\sigma_{xy}/\partial\nu$ and analised the evolution of its maximum with the temperature using $(\partial\sigma_{xy}/\partial\nu)_{max} \propto T^{-\kappa}$. They obtained $\kappa = 0.41 \pm 0.04$ for the first and second Landau levels. Under the common assumption of $p = 2$, this result of κ yields $\gamma = 2.44$. Nonetheless, Amado *et al.* [44, 45] studied the plateau-plateau and the plateau-insulator transitions also in monolayer graphene on Si/SiO_2 using an approach similar to that of Tsui *et al.* [62], that is sweeping the magnetic field instead of the density, and $\kappa = 0.25$ was obtained.
This discrepancy indicates that the criticality in the quantum Hall regime and the influence of the disorder in graphene remains unclear. In this chapter, we will show our results on the plateau-plateau transition in bilayer graphene enclosed by two flakes of h-BN .

5.2 Experimental measurement of plateau-plateau quantum phase transitions

In order to experimentally observe the plateau-plateau quantum phase transitions well developed plateaus are desirable. This can be achieved using high mobility devices in combination with low carrier density. As explained in Chapter 4, using h-BN as substrate enhances the mobility of the devices and reduce the corrugation and strain. Therefore, after many devices using SiO_2 as substrate, we tried to use a bilayer graphene flake which was on top of a hexagonal boron nitride flake used to reduce the doped impurities and the strain. After many attempts, we finally obtained such device. Additionally, another flake of h-BN was placed on top of the graphene flake in order to avoid further contamination from its exposure to the environment. This sample showed a very high mobility for a non-suspended bilayer graphene device, $\mu \approx 40000$ cm^2/Vs , and low density, $n \approx 10^{11}$ cm^{-2}. Additionally, there was not any considerable carrier density gradient ($\delta n/n \lesssim 5\%$), so this sample showed the optimum characteristics for our purposes.

5.2.1 Characterisation of the h-BN /bilayer graphene/h-BN

For our study we used a bilayer graphene flake enclosed by two h-BN flakes fabricated following the procedure developed by Zomer *et al.* [25]. The h-BN underneath the graphene

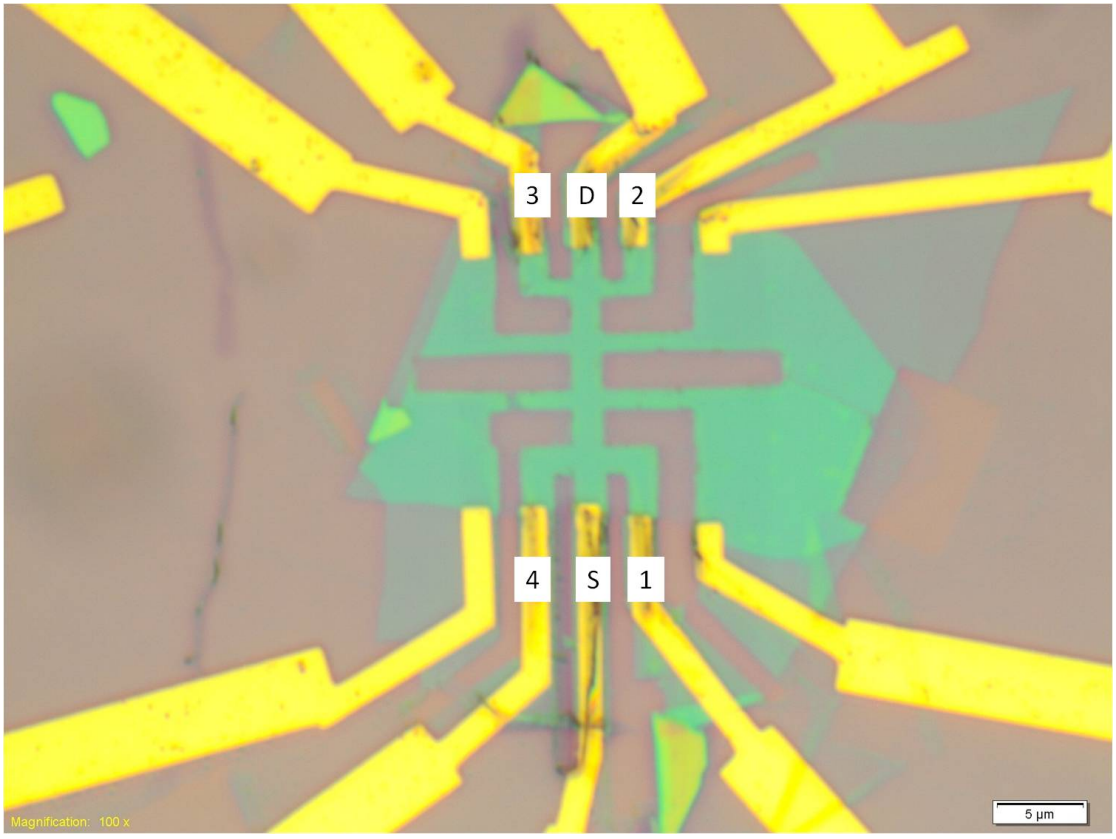

Figure 5.1 Optical image of the bilayer graphene device tailored in the geometry of a Hall bar and enclosed by two h-BN flakes and used in our quantum phase transition experiments. The green flakes are those of h-BN .

(*i.e.,* between the SiO_2 and the graphene) is meant to reduce the corrugation and avoid the spurious effects observed when graphene is on top of SiO_2 [18]. The purpose of the h-BN flake covering the graphene is reduce the contamination of the sample from its exposure to the environment, protecting it from adsorbing charged impurities.
The sample used is shown in figure 5.1.
A current $i = 10$ nA was injected in the sample through contact S. We used the setup depicted in section 3.3. An ac voltage ($f \sim 15$ Hz) of 5 V is generated and injected into the sample which is connected with an in series resistor of 500 MΩ.
The resistivity (either ρ_{xy} or ρ_{xx}) is obtained by measuring the voltage drop using several lock-in amplifiers using the signal generated as external reference. The current flowed from contact S to contact D and the Hall resistivities are obtained as: $\rho_{xy}^{41} = (V_4 - V_1)/i$ and $\rho_{xy}^{32} = (V_3 - V_2)/i$. Similarly, the longitudinal resistivities were measured using $\rho_{xx}^{43} = (V_4 - V_3)/i \cdot W/L$ and $\rho_{xx}^{12} = (V_1 - V_2)/i \cdot W/L$.

The sample was inserted in our Heliox cryostat (section 3.1.1) and cooled down at a base temperature of $T = 300$ mK. We swept the gate voltage and found the Dirac peak to be at $V_D = 0.5$ V. Also, as seen in figure 5.2 the difference between the two ρ_{xx} measured is negligible, and we will thus refer to any of them indistinctively.

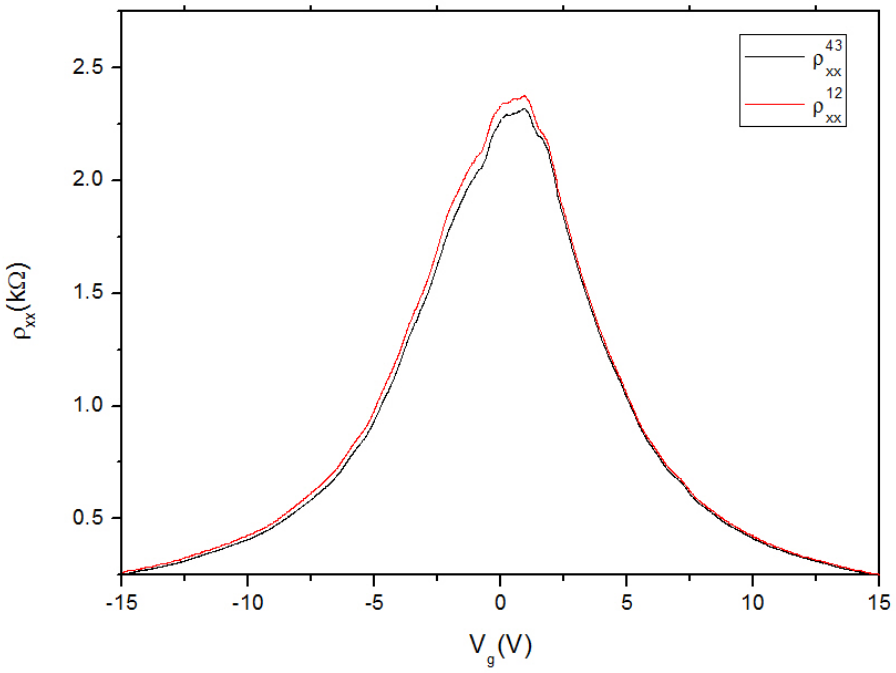

Figure 5.2 Longitudinal resistivites as a function of the gate voltage at $T = 300$ mK and with no magnetic field. In black we show the resistivity measured using contacts 4 and 3 and in red we show the resistivity obtained using contacts 1 and 2.

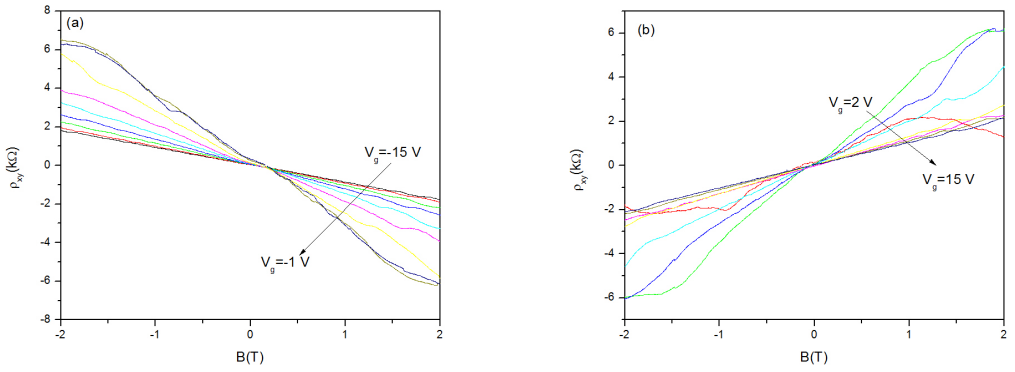

Figure 5.3 ρ_{xy} as a function of the magnetic field at $T = 300$ mK at gate voltages from -15 V to 15 V.

We then measured the Hall resistance by sweeping the magnetic field at constant gate voltages. Doing so, we were able to measure the carrier density at different gate voltages and know the carrier density at a certain gate voltage. We measured the resistivity as a function of the magnetic field either in the hole regime ($V_g < V_D$, shown in fig. 5.3**(a)**) and in the electron regime ($V_g > V_D$, shown in fig. 5.3**(b)**).

From these measurements the carrier density was extracted, using $n = 1/se$, where s is

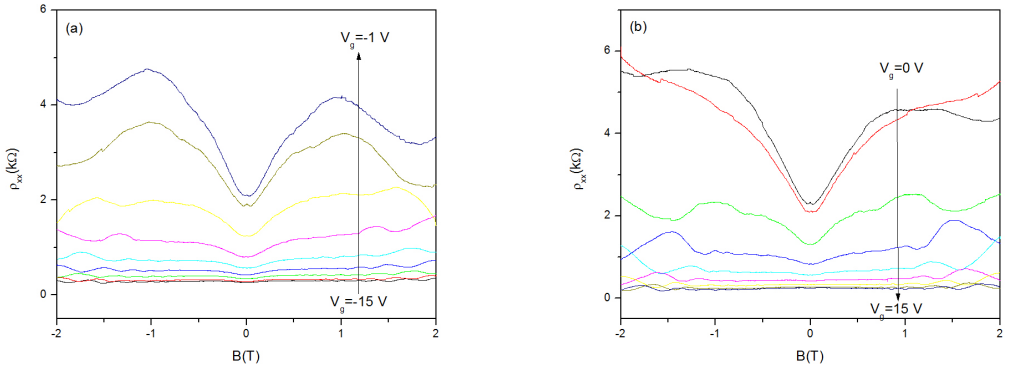

Figure 5.4 ρ_{xx} as a function of the magnetic field at $T = 300$ mK at gate voltages from -15 V to 15 V.

the slope of ρ_{xy} at low magnetic fields ($|B| < 0.5$ T) $s = \partial\rho_{xy}/\partial B$. Fitting the set of data (n, V_g) according to equation 4.1 ($n = \epsilon\left(V_g - V_D\right)/ed = \alpha\left(V_g - V_D\right)$) allows us to obtain both α and V_D.
Our fit gives:

$$n(10^{11}\mathrm{cm}^{-2}) = \begin{cases} 0.39 \cdot V_g + 1.00 & V_g < 0.5\ V \\ 0.39 \cdot V_g + 0.13 & V_g > 0.5\ V \end{cases}$$

The Hall mobility of the device can be quantified using the relation:

$$\mu = \frac{1}{ne\rho_{xx}(0)} \tag{5.4}$$

Where $\rho_{xx}(0)$ is the longitudinal resistivity at 0 T. In figure 5.4 ρ_{xx} as function of the magnetic field at gate voltages $-15\ V < V_g < 15\ V$ are shown.

To summarise, in figure 5.5**(a)** we show ρ_{xx} (left axis) and the density n (right axis) as functions of the gate voltage. The Dirac peak at $V_g \sim 0.5$ V indicates a device with a small number of charged impurities, which is confirmed by the carrier density of the order of 10^{11} cm^{-2} even at 15 V and the high mobility of the sample, shown in figure 5.5**(b)** as function of the density.

As we can see, the mobility is remarkably higher than that of the bilayer graphene device studied in section 4.4.1 and the density is one order of magnitude smaller. As a result, the quantum Hall effect regime is reached at smaller magnetic fields and the plateaus are well developed. In figure 5.6 we show ρ **(a)** and σ **(b)** as functions of the magnetic field. The quantization of the Landau levels follows $\nu = \pm 4, 8, 12, \ldots$, and therefore the

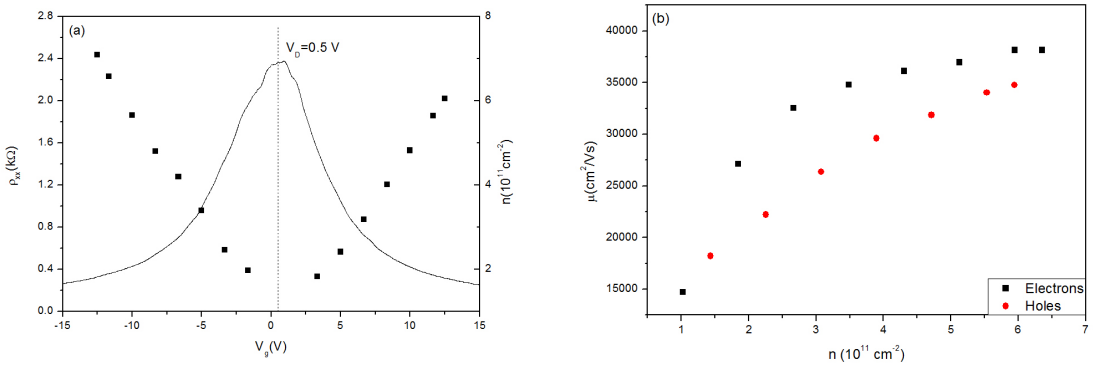

Figure 5.5 **(a)** ρ_{xx} as a function of the gate voltage at $T = 300$ mK at several gates voltages from 2 V to 15 V. The right axis shows the carrier density as a function of the gate voltage.
(b) Hall mobility as function of the density at $T = 300$ mK.

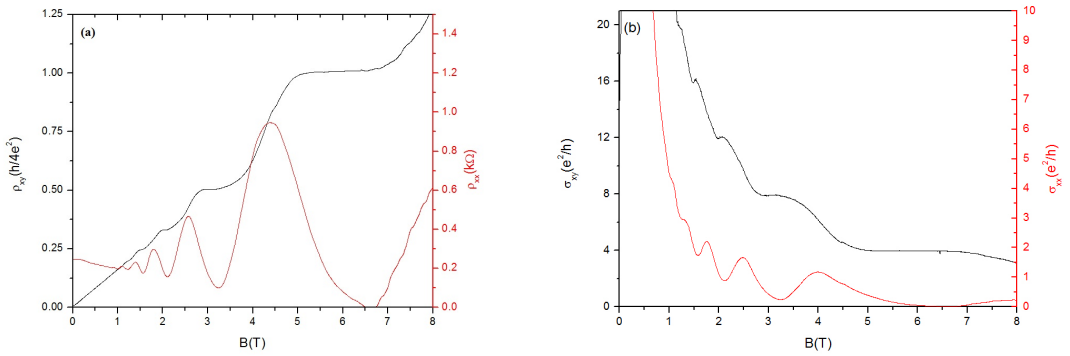

Figure 5.6 **(a)** ρ_{xy} (black line) and ρ_{xx} (red line).
(b) σ_{xy} and σ_{xx}.-it as functions of the magnetic field at $T = 300$ mK. The carrier density was $6.07 \cdot 10^{11}$ cm^{-2}.

Hall resistivity is quantized following $\rho_{xy} = h/4ie^2$ whereas $\sigma_{xy} = 4ie^2/h$. This sequence clearly distinguishes the number of graphene layers on the device and identifies the flake as bilayer graphene.

5.2.2 Study of the plateau-plateau transition in high mobility bilayer graphene

The sample was cooled down to a temperature of $T = 0.3$ K in our Heliox ^{3}He cryostat (see 3.1.1). The gate voltage was set to 15 V, which resulted in a carrier density $n = 6.07 \cdot 10^{11}$ cm^{-2}. Since $\nu = nh/eB$, at this density we can reach the $\nu = 4$ plateau at ~ 6 T, as shown in figure 5.6. We measured ρ_{xx} and ρ_{xy} at different temperatures using the magnetic field as driving parameter. The data are shown in figure 5.7. There

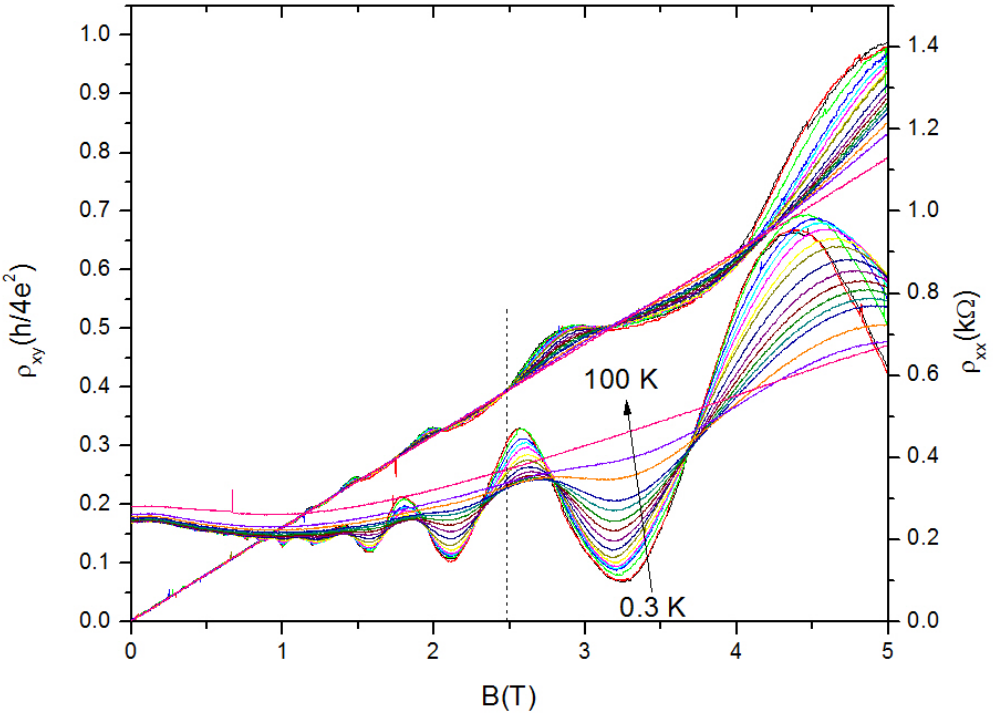

Figure 5.7 ρ_{xy} (in units of $h/4e^2$) and ρ_{xx} as functions of B at temperature $0.3\ K < T < 100\ K$. Notice that the isotherms of ρ_{xy} show a temperature independent crossing point at $B_C = 2.48$ T. The dashed line marks the crossing point at B_C.

is a clear temperature independent crossing point at $B = 2.48$ T. This crossing point indicates the transition from one plateau to another one, and is therefore the point at which the localization-delocalization transition occurs.

We can thus obtain the critical exponent of the transition by means of the scaling law in Eq. 5.2: $(\partial\rho_{xy}/\partial B)_{max} \propto T^{-\kappa}$. In figure 5.8 we show the maximum of the derivative of ρ_{xy} with respect to B between the $\nu = 8$ and the $\nu = 12$ plateaus as a function of the temperature in log-log scale. We analised the transition $\nu = 12 \rightarrow \nu = 8$ because this transition showed a clear and well defined crossing point and because the plateaus $\nu = 8$ and $\nu = 12$ are well developed.

In figure 5.8 we can see that below $T = 5$ K the values of $(\partial\rho_{xy}/\partial B)_{max}$ saturate, showing no longer dependence on the temperature. This is due to the finite dimensions of the sample. As we have shown earlier, the coherence length increases with decreasing temperature (see eq. 5.3). Therefore, we expect that at very low T the coherence length becomes comparable with the Hall bar width (W=1 μm) which is the smallest dimension of the bar. At this point the dominant length scale becomes W itself rather than L_ϕ, which results in the saturation [65].

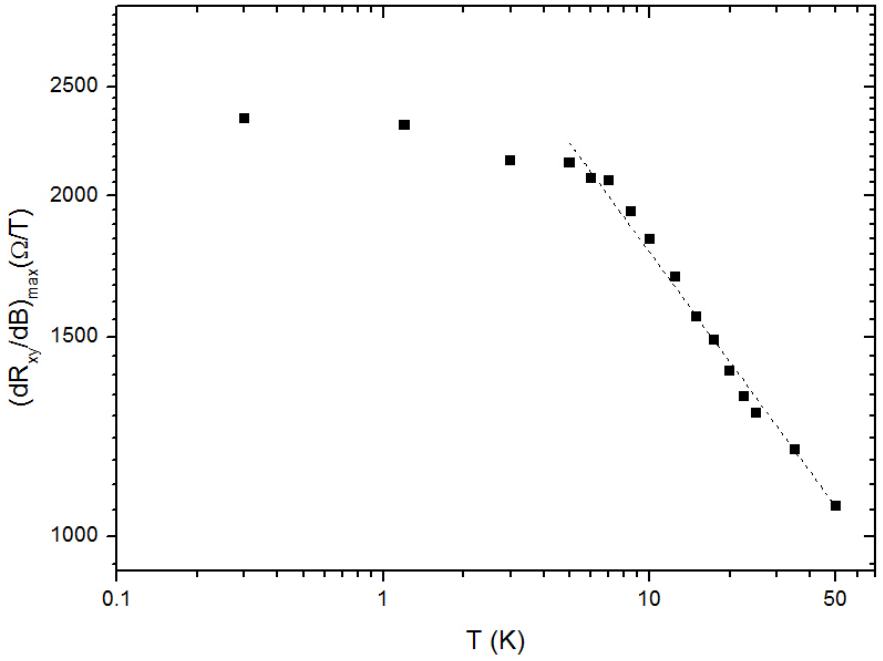

Figure 5.8 $(\partial\rho_{xy}/\partial B)_{max}$ as a function of T for $n = 6.07 \cdot 10^{11}$ cm^{-2} in log-log scale. The dashed line indicates the fit with respect to equation 5.2, giving $\kappa = 0.32$

Nonetheless, from our data, fitting $(\partial\rho_{xy}/\partial B)_{max}$ accordingly to equation 5.2 we obtain a critical exponent $\kappa = 0.32$. This value is in disagreement with the value considered as universal for an Anderson type transition whose value is $\kappa = 0.42$ [4, 62, 65, 69].
We performed several additional measurements at different densities to check if the value of κ depended on the density or the nature of carriers (holes or electrons) or whether it was independent either of n or of the nature of carriers.

These results are shown in figure 5.9, where the isotherms of $\rho(B)$ are plotted at several carrier densities, both in the hole regime and in the electron regime.
Again, we focused on the transitions which showed a clear crossing point. In figure 5.10**(a)-(f)** we show the isotherms of ρ_{xy} as functions of B for the transitions under study. The insets show the isotherms of ρ_{xx} as functions of B.
We analised the temperature dependence of $(\partial\rho_{xy}/\partial B)_{max}$, shown in fig. 5.11 in log-log scale. The critical exponent κ is obtained by fitting the data with respect to Eq. 5.2. We can see that κ is very similar for all the analised transitions, yielding $\kappa \sim 0.30$. The critical exponents obtained by applying scaling law analysis is shown in table 5.1.
We can see that $0.27 < \kappa < 0.32$. The mean value of the critical exponents measured is $\kappa = 0.30 \pm 0.02$. Again, this value is in disagreement with previous experiments on the plateau-plateau transitions which reported $\kappa = 0.42$.

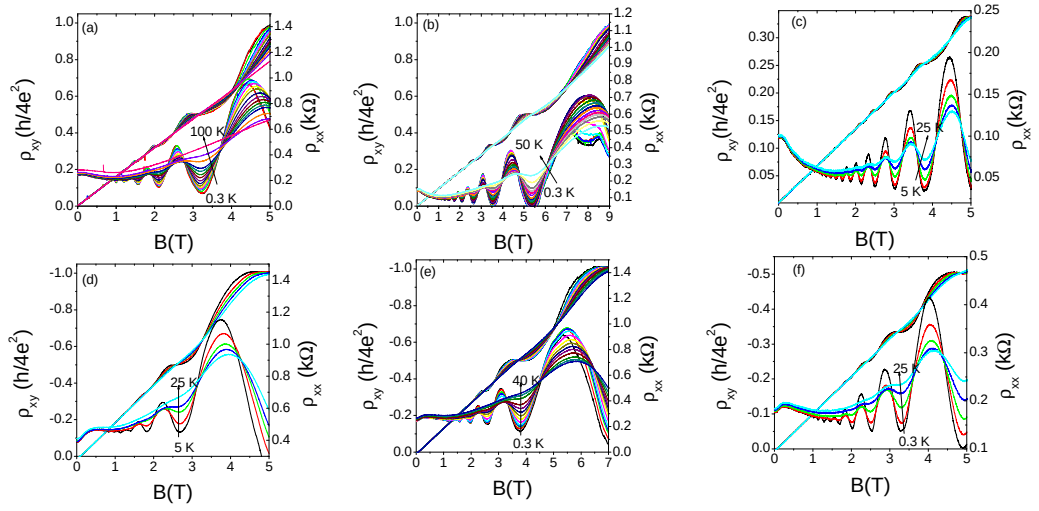

Figure 5.9 Isotherms of ρ_{xx} and ρ_{xy} as functions of B at different carrier densities: $n(10^{11}\ \mathrm{cm}^{-2})$=6.07 **(a)**, 10.3 **(b)**, 14.6 **(c)**, -4.74 **(d)**, -6.98 **(e)** and -9.03 **(f)**.

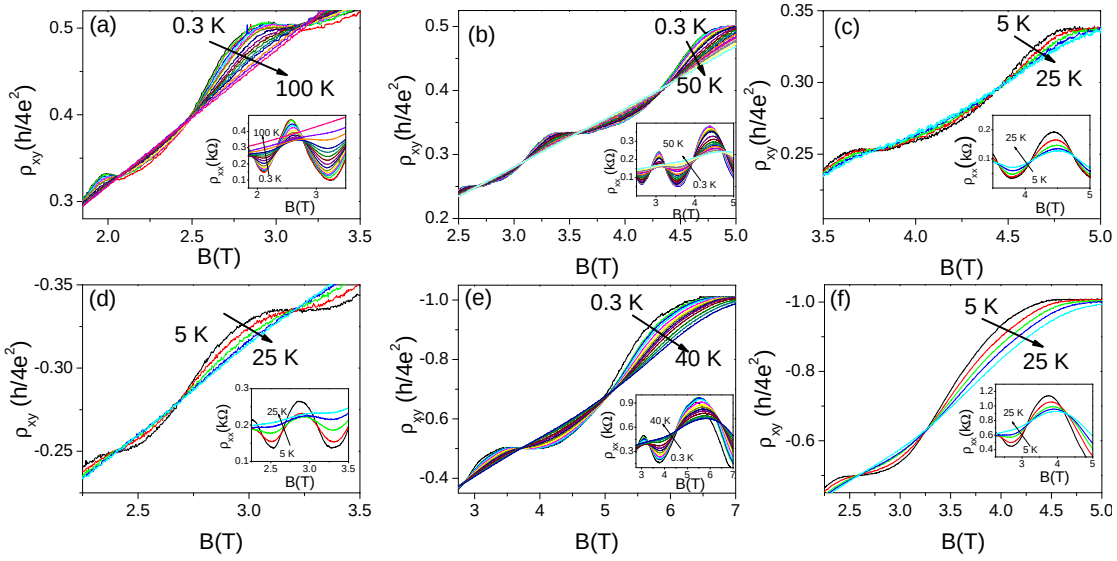

Figure 5.10 Isotherms of ρ_{xx} and ρ_{xy} as functions of B at different carrier densities: $n(10^{11}\ \mathrm{cm}^{-2})$=6.07 **(a)**, 10.3 **(b)**, 14.6 **(c)**, -4.74 **(d)**, -6.98 **(e)** and -9.03 **(f)**.

The criticality of the localization length is described by γ, since $\xi \propto |E - E_c|^{-\gamma}$, we will analyse now what $\kappa \sim 0.30$ implies. Since $\kappa = p/2\gamma$, $\gamma = p/2\kappa$ and therefore, with our data $\gamma = 3.3$. This value differs from the previously reported values of $\gamma = 2.38$.
This difference might be explained if values of p, p being given by eq. 5.3, different than $p = 2$ are possible. In fact, there are several studies in which the measured value of p in graphene differs from that of $p = 2$ [70–73].

n (10^{11} cm^{-2})	PP transition	κ
14.6	$\nu = 16 \rightarrow \nu = 12$	0.27 ± 0.01
10.2	$\nu = 12 \rightarrow \nu = 8$	0.32 ± 0.01
	$\nu = 16 \rightarrow \nu = 12$	0.30 ± 0.01
6.07	$\nu = 12 \rightarrow \nu = 8$	0.32 ± 0.01
-4.74	$\nu = -8 \rightarrow \nu = -4$	0.30 ± 0.02
-6.84	$\nu = -8 \rightarrow \nu = -4$	0.29 ± 0.02
-9.03	$\nu = -16 \rightarrow \nu = -12$	0.32 ± 0.02

Table 5.1 Measured values of for the different transitions at different densities.

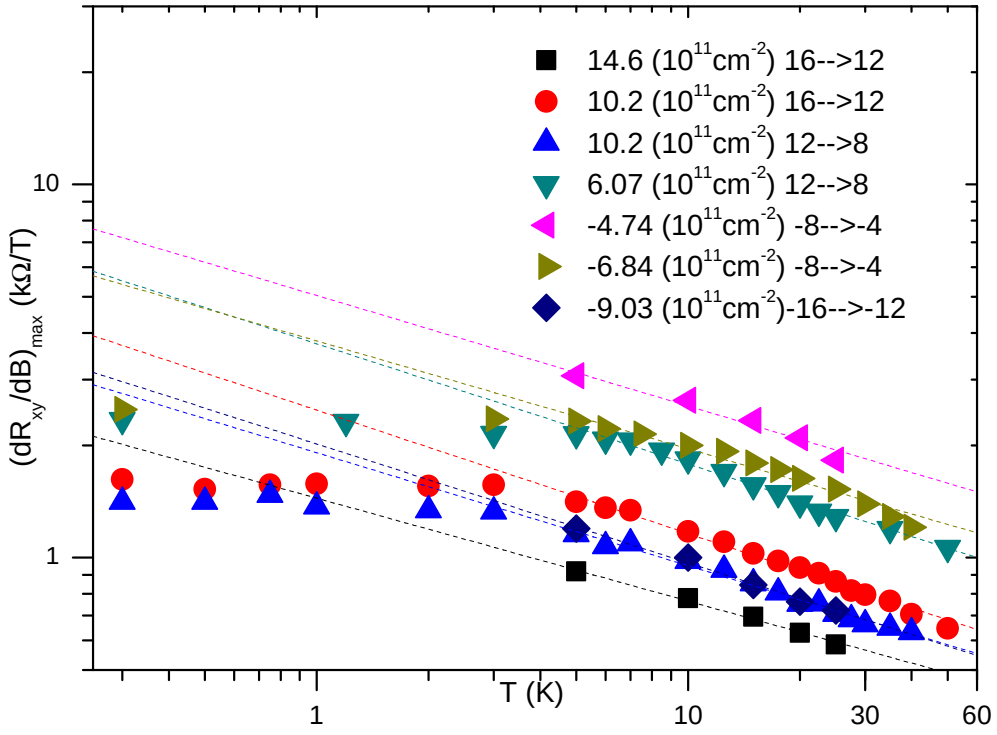

Figure 5.11 $(\partial R_{xy}/\partial B)_{max}$ as a function of T. Lines are fits with respect to Eq. 5.2.

By weak localization experiments (shown in Chapter 6) we measured that for our h-BN /bilayer graphene/h-BN heteroestructure $p = 0.90 \pm 0.02$. This result implies that $\gamma = 1.5$, again in disagreement with previous experiments. Moreover, the result $p = 0.9$ leads to a dynamic critical exponent $z = 2/p = 2.2$, which indicates a screening of the $e - e$ interaction, resulting from a smooth long range disorder which is a typical characteristic of the percolation regime.

Another hint of the kind of e-e interaction derives from the analysis of the conductivity dependence of the zero field longitudinal conductivity $1/\rho$ on the carrier density. As we can see in Fig. 5.12, $1/\rho$ depends linearly on the density. Following Morozov [74], the longitudinal conductivity $1/\rho$ can be expressed as $1/\rho = 1/(\rho_L + \rho_S)$, where ρ_S is a constant resistivity which does not depend on the density and which is caused mainly by

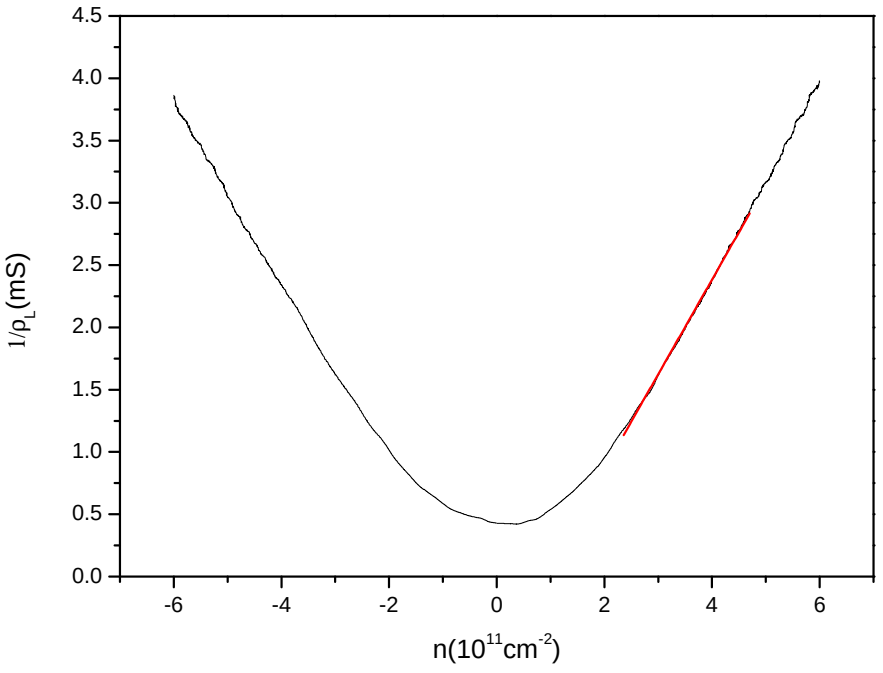

Figure 5.12 $1/\rho$ as a function of n at $B = 0$ and $T = 0.3$ K. It is observed that $1/\rho$ depends linearly on the density.

short range scattering, whereas $\rho_L^{-1} \propto n$ and is affected by long range scattering. Since $1/\rho \propto n$, it can be argued that $\rho_S \sim 0$, and therefore the scattering is mainly caused by long range interactions. Because of that, the plateau-plateau transition might be follow a mechanism which differs from that of an Anderson type transition.

In fact, our result of $\gamma = 1.5$ is compatible with a percolation scenario as studied by Trugman. According to Trugman, in the case of a smooth long range disorder, the localization-delocalization transition is governed by a classical percolation regime characterized by $\gamma = 4/3$ [75]. Our result $\gamma = 1.5 \pm 0.1$ is compatible with a percolation regime.

In fact, there is another way to measure γ. This approach relies on the behaviour of the conductivity in the tails of the Landau levels. In these regime, the conductivity follows [68, 76]

$$\sigma_{xx} \propto e^{-\sqrt{T_0/T}}/T \tag{5.5}$$

The characteristic temperature T_0 is a quantity inversely proportional to the localization length. Thus, combining $T_0 \propto \xi^{-1}$ and $\xi \propto |E - E_c|^{-\gamma}$, we have $T_0 \propto |E - E_c|^{\gamma}$. Since

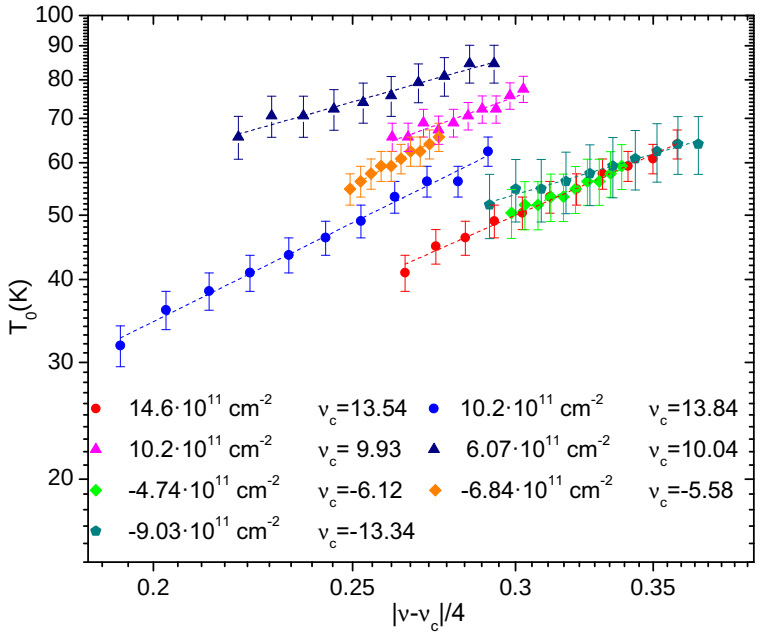

Figure 5.13 Characteristic temperatures T_0 in the Landau level tails as a function of the filling factor ν for each one of the analysed plateau-plateau transitions. The dashed lines correspond to the fit of the data following eq. 5.6.

the parameter we tune close to the criticality is the magnetic field, which is equivalent to tune the filling factor, this relation results in

$$T_0 \propto |\nu - \nu_c|^{\gamma} \tag{5.6}$$

Here, ν_c is the filling factor at the critical magnetic field B_c. Thus, if the conductivity at different temperatures and at a magnetic field is measured, we can obtain the characteristic temperature at certain filling factor. Then, repeating this method at different magnetic fields in the Landau level tails (between the maxima and minima in σ_{xx}), we obtain T_0 as a function of ν.

Fitting T_0 with respect to ν following eq. 5.6 we obtained γ for each transition. In figure 5.13 we show the values of T_0 obtained for each one of the analised transitions as functions of $|\nu - \nu_c|$. As we can see from the data, the data show a similar dependence with γ, being the mean value $\gamma = 1.4 \pm 0.2$, which is in remarkable agreement with the value of γ obtained indendently and which is in agreement with a plateau-plateau transition in the classical percolation regime.

Thus, the overall picture of the transport regime in the sample can be described as follows. The linearity of $1/\rho$ with $\rho_S = 0$ indicates the presence of long range scattering processes and the absence of short scattering mechanisms. Furthermore, $p = 0.9$ implies $z = 2/p = 2.2$, which additionally suggests that the e-e interaction is screened. As a consequence, we have long range scattering processes with e-e interaction screened,

which results in a smooth long range disorder, leading the transitions to be governed by a percolation regime as described by Trugman [75].

5.3 Summary and conclusions

In Chapter we have shown our results obtained using a high mobility graphene bilayer flake enclosed by two flakes of h-BN .
We have throughly shown the characterisation of the device using a gate voltage and magnetic fields, showing the high quality in terms of density, inhomogeneity and mobility of the device.
We have then studied a number of plateau-plateau quantum phase transitions and its universality. We have shown that γ is compatible with a classical percolation regime $\gamma = 4/3$ by two different and indepent approaches, both of them yielding results $\gamma \sim 1.4$.

Chapter 6

Zero and low field transport regimes in graphene

High magnetic field experiments prove to be a very useful tool in unraveling phenomena such as the localization-delocalization transitions. Nonetheless, small magnetic field measurements and zero field experiments also yield important information. In this Chapter we will show our data on low and zero field on graphene.

6.1 Introduction

We have explained how the measurement of the resistivity as a function of the density (changed by means of applying a gate voltage) allows us to obtain information about the mobility and the charged impurities in the sample. There are nonetheless measurements which can be performed using very low (and even zero) magnetic field in order to obtain additional information and observe different effects. In particular, we will show in this Chapter our results on weak localization in monolayer and bilayer graphene as well as different transport mechanisms driven by the carrier density.

6.2 Weak localization

It has been proved that quantum interference affects the conducting properties of bidimensional materials at low temperatures [77], deviating the behaviour of the conductivity from Drude's model, where $\sigma_0 = \mu n e$ [55].
Electrons propagating in time-reversed counter-propagating closed paths will suffer from constructive intereference, increasing the back scattering probability. As a result, the conductivity will be decreased from the prediction of Drude's model, an effect known as weak localization [78, 79]. Nonetheless, this effect holds as long as carriers keep their phase coherence and only if time-reversal symmetry holds. Therefore, since the inelastic scattering induces a loss of phase coherence, we can introduce a decoherence length L_ϕ which limits the number the number of constructively interfering paths to a length smaller than L_ϕ. The weak localization correction to Drude's conductivity at zero field is given by [77]

$$\delta\sigma_{WL} = g_s g_v \frac{e^2}{4\pi^2\hbar} \ln\left(1 + \frac{\tau_\phi}{\tau_s}\right) \tag{6.1}$$

Where g_s and g_v are the spin and valley degeneracies, τ_ϕ is the decoherence time associated with L_ϕ and τ_s is the mean elastic scattering time.
Nonetheless, since weak localization takes place as long as time reveral symmetry holds, the presence of a magnetic field perpendicular to the two dimensional electron gas will break the weak localization corrections to the conductivity, leading to the classical magnetoconductivity as the magnetic field is increased. Indeed, the presence of Aharonov-Bohm phases [80] $\delta\varphi \sim \pi\phi/\phi_0$ (where $\phi = BS$, the magnetic flux and ϕ_0 is the flux quantum) between time-reversed paths results in lowering the interference, leading to a restoration of Drude's model when a finite magnetic field is applied. Therefore, the expected behaviour will be to observe a minimum in the conductivity at $B = 0$ followed

by an increase of the magnetoconductivity as the magnetic field increases.
Nevertheless, electronic carriers in graphene are known to be chiral [12, 15, 81, 82], *i.e.,* are eigenstates of both the Dirac hamiltonian $H = v_f \boldsymbol{\sigma} \cdot \boldsymbol{p}$ (where $\boldsymbol{\sigma}$ is the pseudospin operator and $\boldsymbol{p}$ is the momentum) and the helicity operator: $h = \boldsymbol{\sigma p}/|\boldsymbol{p}|$ with defined values: +1 for electrons in the K point and -1 at K'. Therefore, since a back scattering event implies a reversal of the sign of the wave vector in the reciprocal space ($\boldsymbol{q} \rightarrow -\boldsymbol{q}$), which would imply that chirality is not conserved and is thus a forbidden effect, weak localization is forbidden in graphene as long as the carriers remain eigenstates of the Dirac Hamiltonian.
Therefore, in graphene an increase with respect to σ_0 is expected for $B = 0$, followed by a decreasing of the conductivity as the magnetic field is increased, effect known as weak antilocalization [79, 83].
Weak antilocalization will take place as long as chirality is a good quantum number, therefore, far away from the K and K' points, where the energy bands deviate from the linear dispersion, back scattering processes are allowed and weak antilocalization will be supressed. Furthermore, since carriers at different valleys have opposite pseudospins (and therefore opposite chirality) back scattering processes between valleys (intervalley backscattering) are allowed [84].
As a result, the presence of intervalley backscattering will imply a transition from weak antilocalization to weak localization events. This intervalley backscattering processes are induced by short range potentials (adatoms and vacancies).
We can associate the mean elastic scattering time τ_s to the valleys taking place within the same valley (intravalley) and for which the chirality is a good quantum number, τ_w to intravalley processes with trigonal warping and for which chirality is not a good quantum number and τ_i to the intervalley scattering events.

6.2.1 Weak localization and weak antilocalization in monolayer graphene

We studied a monolayer graphene device (shown in figure 6.1) tailored in the geometry of a Hall bar. We started the study of the sample by characterizing the transport properties as explained in section 4.3. Fitting the Dirac peak (shown in figure 6.2) following the approach developed by Kim *et al.* [85] we obtained the position of the charge neutrality point at $V_D = 4.66$ and the density of residual charges is $n_{res} \sim 2 \cdot 10^{12}$ cm^{-2}. Since the density of impurities in the interface between the graphene and the SiO_2 can be stimated by means of $n_{res} = 0.2 \cdot n_{imp}$ [86], the density of charged impurites was calculated to be $n_{imp} \approx 10^{12}$ cm^{-2}.

The carrier density as a function of the gate voltage is shown in figure 6.2. The density was obtained at 0.3 K by Hall resistance measurements, as explained in Chapter 4,

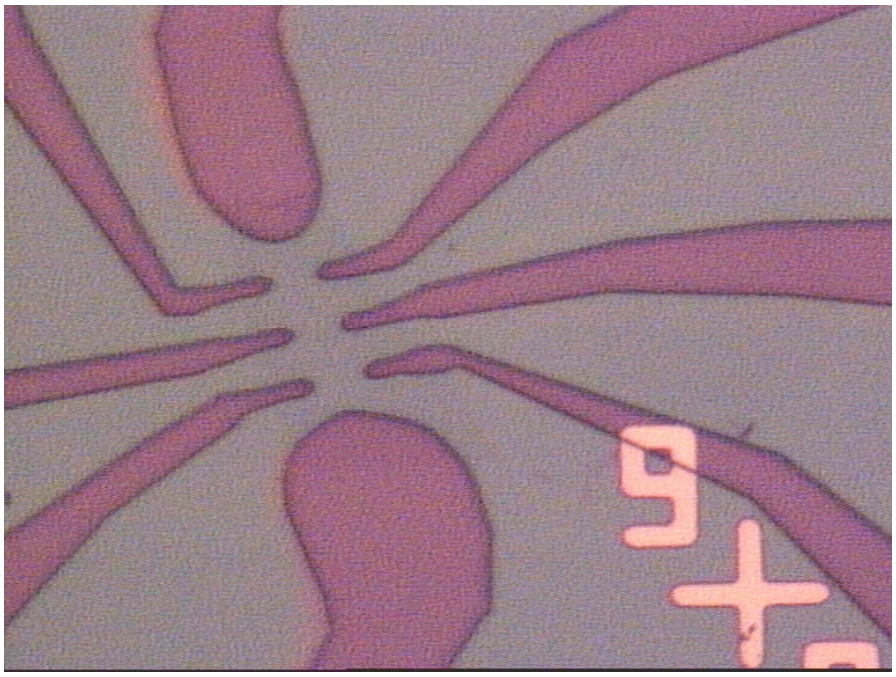

Figure 6.1 Optical image of the monolayer graphene Hall bar"S2601" used in our WL-WAL study.

which ranged from $n = 0.7 \cdot 10^{12}$ cm^{-2} at $V_g \sim 0$ V to $n \sim 4 \cdot 10^{12}$ cm^{-2} at $V_g \sim -40$ V. The mobility of the sample showed a small decrease with increasing density, being $\mu \simeq 4000$ cm^2/Vs at carrier density $n \simeq 0.7 \cdot 10^{12}$ cm^{-2} and $\mu \simeq 3600$ cm^2/Vs at carrier density $n \simeq 2 \cdot 10^{12}$ cm^{-2}.

The resistivity was measured as a function of the magnetic field at different gate voltages at 0.3 K, showing weak localization far away from the charge neutrality point and a competition between weak localization and weak antilocalization at a gate voltage of 0 V. We show this competition in figure 6.3, where a clear transition from weak antilocalization regime to weak localization regime can be observed as the gate voltage is set far from the charge neutrality point.

We see in figure 6.3 that as the gate voltage is set further from the charge neutrality point, the amplitude of the weak localization peak decreases. This is due to the fact that as the Fermi level is incresingly driven further from the charge neutrality point, more carriers are added to the sample, resulting in an increase of the hole-hole scattering rate. Therefore, τ_ϕ decreases, and so does the number of closed paths which give rise to constructive interference and therefore to weak localization. We can also observe that at 0 V the magnetoresistivity increases with increasing magnetic field, evidencing the presence of weak antilocalization at low energies. This effect disappears at energies. Indeed, at -10 V the magnetoresistivity doesn't increase with the magnetic field, due to the trigonal warping and the supression of chirality conservation. Therefore, by changing the

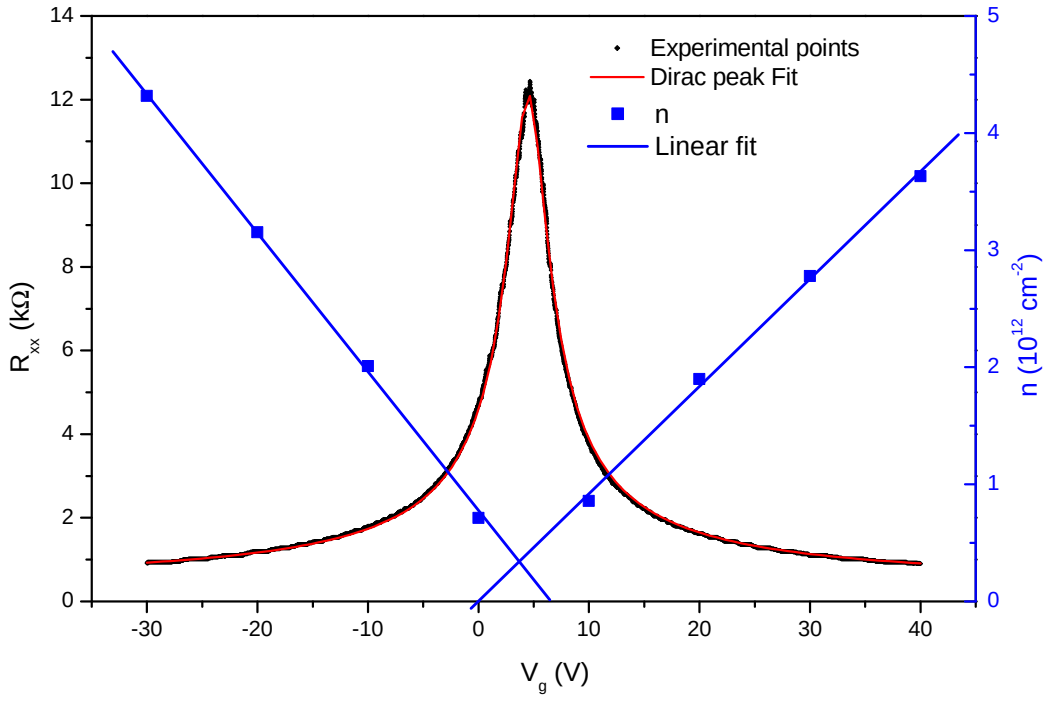

Figure 6.2 Black line shows R_{xx} as a function of the gate voltage and the red line shows its fitting with respect to the model by Kim. Blue squares show the density as a function of the gate voltage, and the blue lines show the fits of the data with respect to eq. 4.1

gate voltage the transport regime is changed from intervalley processes where trigonal warping is negligible ($\tau_s^{-1} > \tau_w^{-1}$) to a trigonal warping dominated regime ($\tau_s^{-1} < \tau_w^{-1}$) at $V_g = -10$ V.

This is evidenced in figures 6.4 and 6.5. We compared these two regimes in figures 6.4 and 6.5. In figure 6.4 we show $\delta\sigma$ as a function of the magnetic field at $V_g = 0$ V (that is, close to the charge neutrality point) at different temperatures; whereas in figure 6.5 we show the same set of data at a different gate voltage, $V_g = -10$ V, that is, at higher energies and in presence of trigonal warping.

In figure 6.4 we observe a deep hollow at $|\boldsymbol{B}| \gtrsim 0$, signature of the weak localization, whose depth decreases with increasing temperature, as a result from the supression of the quantum interferences due to the fact that at higher temperatures the phase coherence is decreased. We can also see that there is a maximum at $B \approx 0.06$ T, at magnetic fields greater than 0.06 the magnetoconductivy decreases with increasing magnetic field, as expected in the presence of weak antilocalization. This point marks the transition from weak localization to weak antilocalization. This transition is expected to take place at a magnetic field B_i such that $\tau_B \approx \tau_i$ [87]. However, since the weak localization correction

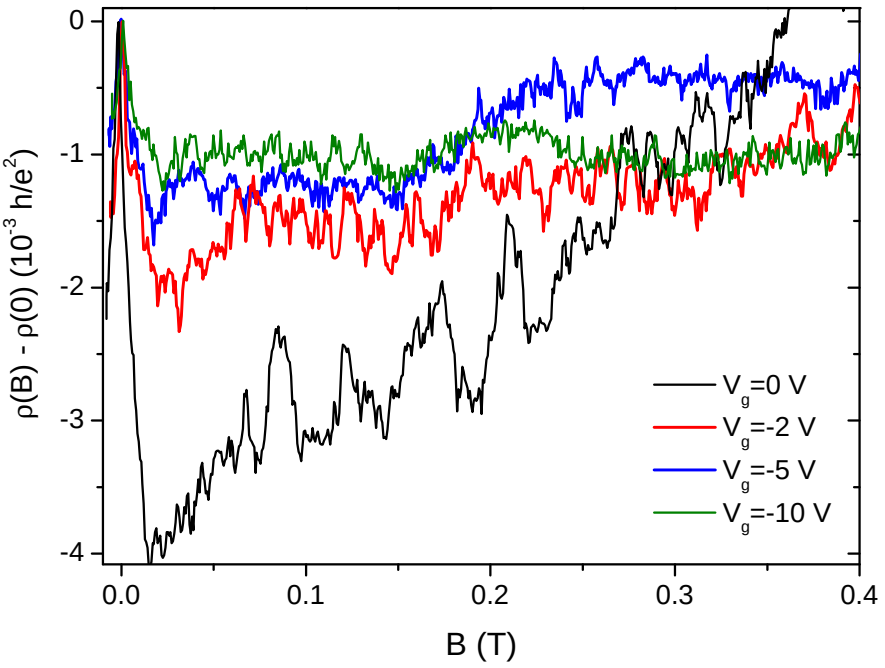

Figure 6.3 Weak localization and weak antilocalization corrections to the resistivity at gate voltages from 0 V to -10V at 0.3 K.

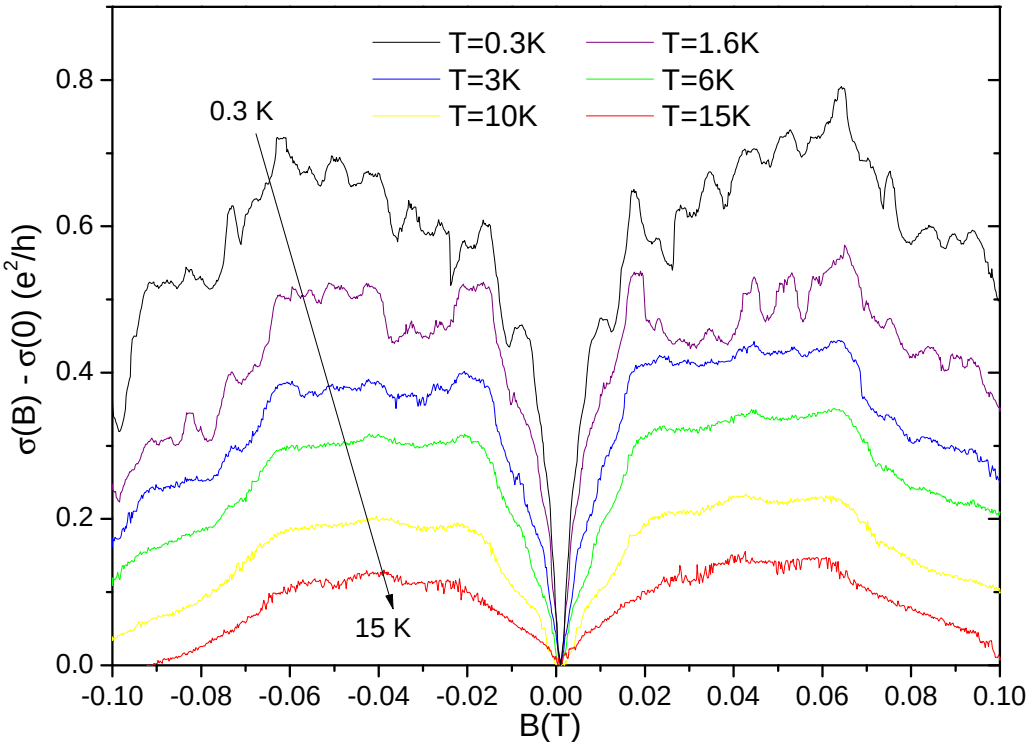

Figure 6.4 Weak localization and weak antilocalization corrections to the resistivity at gate voltage 0 V and at temperatures from 0.3 K to 15 K.

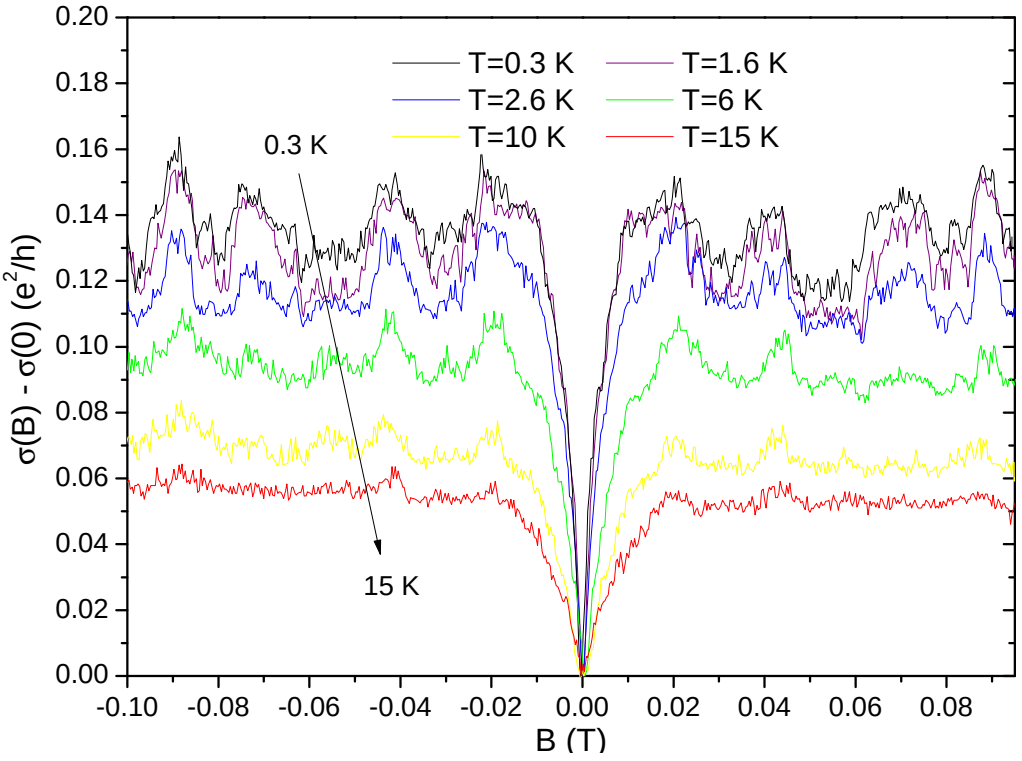

Figure 6.5 Weak localization in graphene measurements in graphene taken at $V_g = -10$ V at different temperatures. The absence of weak antilocalization is caused by the trigonal warping.

also depends on the magnetic field, the magnetic field must be renormalized by a factor of $4e^{\gamma}$ [88], where γ is Euler's constant. From the renormalized value of B_i we can stimate the intervalley scattering rate $\tau_i^{-1} \simeq 0.5 \cdot 10^{12}$ s^{-1} at $n = 0.7 \cdot 10^{12}$ cm^{-2}. Since weak antilocalization survives at $B > B_i$ we can argue that intravalley scattering processes take place at lower time scale ($\tau \propto B^{-1}$) with respect to intervalley processes. Thus, $\tau_s^{-1} \gg \tau_i^{-1}$, which implies that the intravalley long range scattering events dominate in this sample.

On the other hand, at energies far from the charge neutrality point (figure 6.5), we can see how weak antilocalization is supressed and only weak localization corrections are observable. In this case, the transport regime is changed from one in which $\tau_s^{-1} > \tau_w^{-1}$ to one dominated by trigonal warping, *i.e.*, $\tau_s^{-1} < \tau_w^{-1}$. We can also observe that the weak localization corrections are supressed at a magnetic field $B_i \simeq 0.02$ T, which after renormalization, yields $\tau_i \simeq 0.3 \cdot 10^{12}$ s^{-1}.

6.2.2 Weak localization in a h-BN/bilayer graphene/h-BN heteroestructure

Aiming to extend our study on the plateau-plateau transitions shown in Chapter 5 we studied weak localization effects in the bilayer graphene and hexagonal boron nitride heteroestructure (shown in figure 5.1) used for our quantum phase transitions studies. We measured the magnetoresistivity at magnetic fields smaller than 15 mT. The weak localization signal was very small due to the small degree of disorder in the sample, which encouraged us to increase the excitation current to 100 nA.
The figure 6.6 shows the weak localization peak as a function of the magnetic field at temperatures from 0.3 K to 15 K. The weal localization to magnetoconductivity in bilayer graphene is given by [70]:

$$\Delta\sigma(B) = \frac{e^2}{\pi h}\left[F\left(\frac{B}{B_\phi}\right) - F\left(\frac{B}{B_\phi + 2B_i}\right) + 2F\left(\frac{B}{B_\phi + B_*}\right)\right] \tag{6.2}$$

Where $F(z) = \ln z + \psi\,(1/2 + 1/z)$ and $B_{\phi,i,*} = \hbar\tau_{\phi,i,*}/(4De)$, being ψ the digamma Euler function.

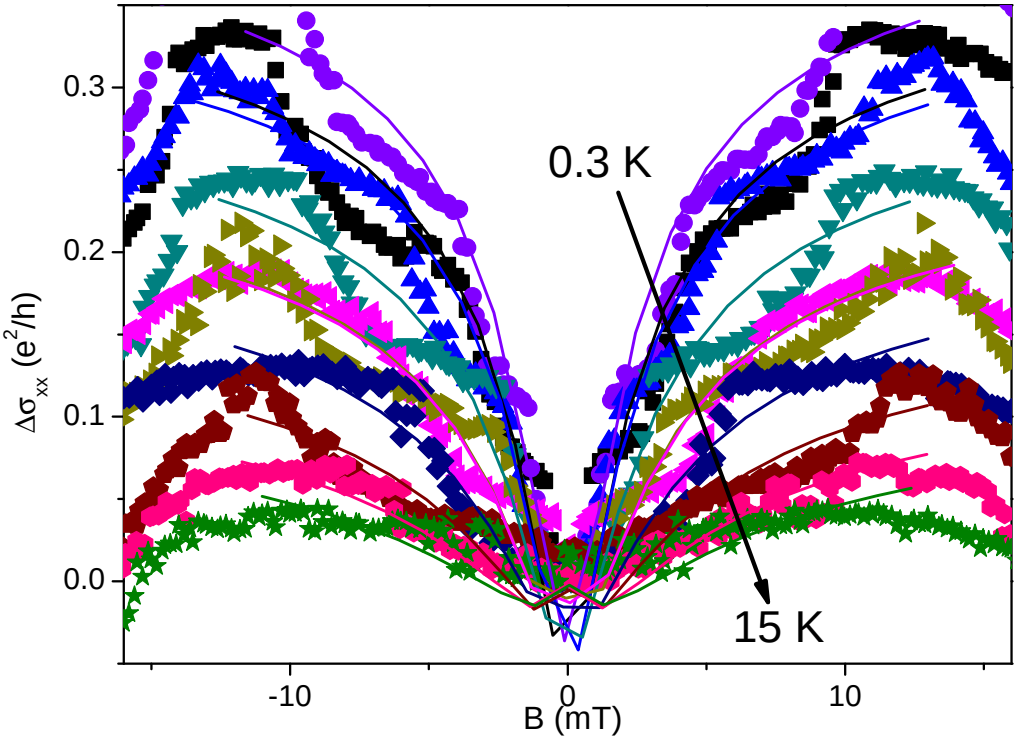

Figure 6.6 $\Delta\sigma$ as function of B at different temperatures from 0.3 K to 15 K. Solid lines are fits with respect to equation 6.2

From the fits at different temperatures shown in figure 6.6 we obtained τ_ϕ and therefore the coherence length L_ϕ as a function of temperature. These data are shown in figure 6.7.

We fitted the experimental data to equation 5.3, namely $L_\phi \propto T^{-p/2}$. In figure 6.7 we observe that, in agreement with the observed saturation of $(\partial\rho_{xy}/\partial B)_{max}$ (see figure 5.9), L_ϕ saturates at $L_\phi \simeq 0.8$ μm, being the smallest dimension of the sample $W \lesssim 1$ μm. This is in accordance with our interpretation of the saturation of $(\partial\rho_{xy}/\partial B)_{max}$ as a consequence of the finite dimensions of the sample.
Also, the fit gives $p = 0.90 \pm 0.02$ (shown in figure 6.7) instead of $p = 2$.

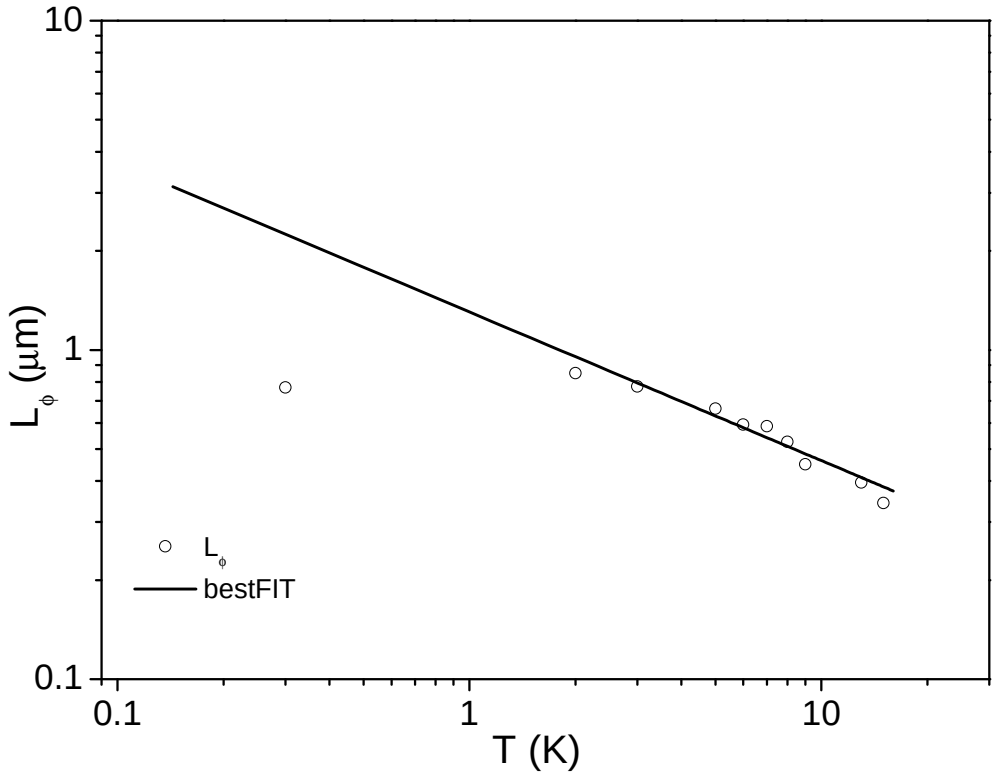

Figure 6.7 Coherence length as a function of temperature obtained by fitting the experimental $\Delta\sigma$ data shown in Fig 6.6 to eq. 6.2. The black line represents the best fit to Eq. 5.3, giving $p = 0.9$.

6.3 Zero magnetic field characterization of a h-BN /bilayer graphene/h-BN heteroestructure

We used our bilayer graphene flake enclosed by two flakes of h-BN . We studied the dependence of $\rho_{xx}(V_g)$ on the temperature at zero magnetic field.
In figure 6.8 we show the Dirac peak's variation with the temperature. Close to the charge neutrality point, the data show a an insulatiing behaviour, $\partial\rho_{xx}/\partial T < 0$. We can observe that at $V_g - V_D \simeq \pm 5$ V, *i.e.*, at densities $n \simeq \mp 2.5 \cdot 10^{11}$ cm^{-2}, the isotherms show a crossing point. When the gate voltage is set far away from the charge neutrality point, $|V_g - V_D| > 5$ V, a metallic behaviour, $\partial\rho_{xx}/\partial T > 0$ is observed.
This temperature indepentent crossing point might be thought to be an indication of a

density driven quantum phase transition from a metallic state to an insulating state when the density drops below a critical value [89, 90], similar to those transitions studied in Chapter 5. Nevertheless, a quantitave analysis of the data shows that this isn't a proper quantum phase transition in the sense of a metal to insulator transition.

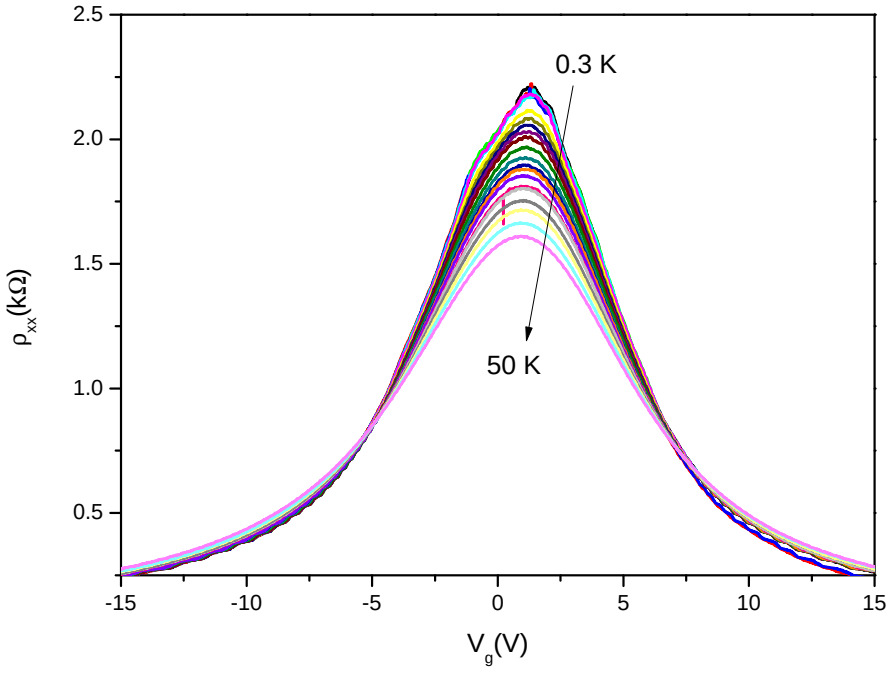

Figure 6.8 Four probes measurement of the longitudinal resistivity using the gate voltage as driving parameter at 0 T and at temperatures such that $0.3 < T < 50$ K.

At temperatures above 10 K, the density driven transition from $\partial\rho_{xx}/\partial T < 0$ to $\partial\rho_{xx}/\partial T > 0$ is evident when the gate voltage is increased as shown in figures 6.9(a) and (b). Nonetheless, the possibility that we are facing a metal to insulator transition is soon ruled out. The whole range of resistivity measured is spaned over one order of magnitude ($200\,\Omega \lesssim \rho_{xx} \lesssim 2000\,\Omega$) whereas in systems showing a metal-insulator transition the resistivity varies in a range over $10^5\ \Omega$ [91, 92]. Furthermore, the separatrix at the critical density in a metal-insulator transition should appear at $\rho_{xx}(n_c) \simeq 3h/e^2$ [93], whilst in our system it appears at $\rho_{xx}(n_c) \simeq 900\ \Omega$, *i.e.*, two orders of magnitude smaller.

We identified four different transport regimes characterized by the boundaries defined by the density (n_c) and the temperature ($T \approx 10$ K) which will be discussed next.
For $T > 10$ K and close to the charge neutrality point the conductivity increases with increasing temperature, showing a linear dependance with T at temperatures 10 K$<$ T $<$50 K, as shown in figure 6.10(a). This follows from a parabolic dispersion of the energy bands, as expected in bilayer graphene. Since this parabolic energy-momentum

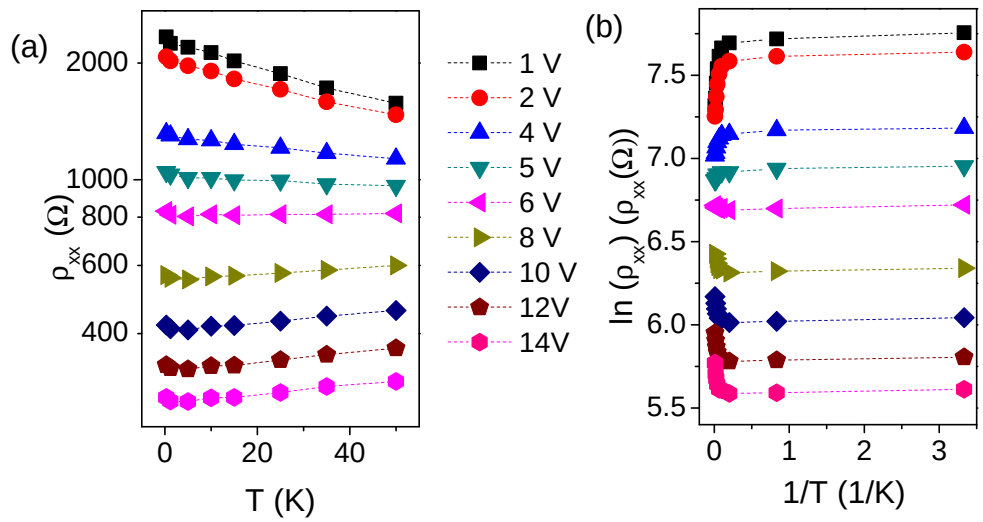

Figure 6.9 (a) $\rho_{xx}(T)$ at gate voltages from 1 V to 14 V. The behaviour in the hole regime is qualitatively similar.
(b) $\ln \rho_{xx}$ as a function of T^{-1} for the same gate voltages than (a).

results in a constant density of states, the minimum conductivity is calculated using $\sigma_{min} = e\mu \int D(E)\left[f(E,T) - f(E,T=0)\right] \mathrm{d}E$, which gives $\sigma_{min} = 4 \ln 2\, e\mu m k_B T/\pi\hbar^2$. Here $D(E)$ is the density of states, $f(E,T)$ is the Fermi-Dirac distribution function, m is the effective mass and μ is the mobility.
Our data fit well with a linear dependence, yielding a slope of which ranges from 3.5 $\mu S/K$ to 4 $\mu S/K$ for a gate voltage around $V_g = \pm 2$ V. This method has already been applied to obtain the effective mass of a suspended bilayer graphene device, obtaining a value of $m = 0.03 m_e$ [94]. In our case, the data reveal a supression of the effective mass down to $m = 0.009 m_e$ at the charge neutrality point. This is in accordance with recent calculations [95] and experiments performed on graphene on SiO_2 [96].

For $T > 10$ K and at densities $n > n_c$, the conductivity decreases with increasing temperature, characteristic of ballistic transport. Ballistic regimes take place when $T\tau > \hbar$. From the onset of the linear dependence of the conductivity, we can estimate that the mean elastic scattering time is $\tau \simeq 0.7$ ps. Since the mobility can be written as $\mu = e\tau/m$, $\tau = 0.7$ ps results in a mobility $\mu \simeq 41500$ cm^2/Vs , which is in good agreement with the Hall mobilities measured at high density (see figure 5.5(b)).

At low temperature ($T < 10$ K) the behaviour is that of an insulating material $\partial\rho_{xx}/\partial T$ regardless of the density. At low energies; that is, close to the charge neutrality point, the resistivity follows $\rho_{xx} \propto \exp\left((T/T_0)^{-1/3}\right)$, as shown in figure 6.10(c). This dependence is expected for transport mediated by variable range hopping [97], *i.e.*, localized impurity states inside a gap. Such behaviour has also been found in bilayer graphene systems in

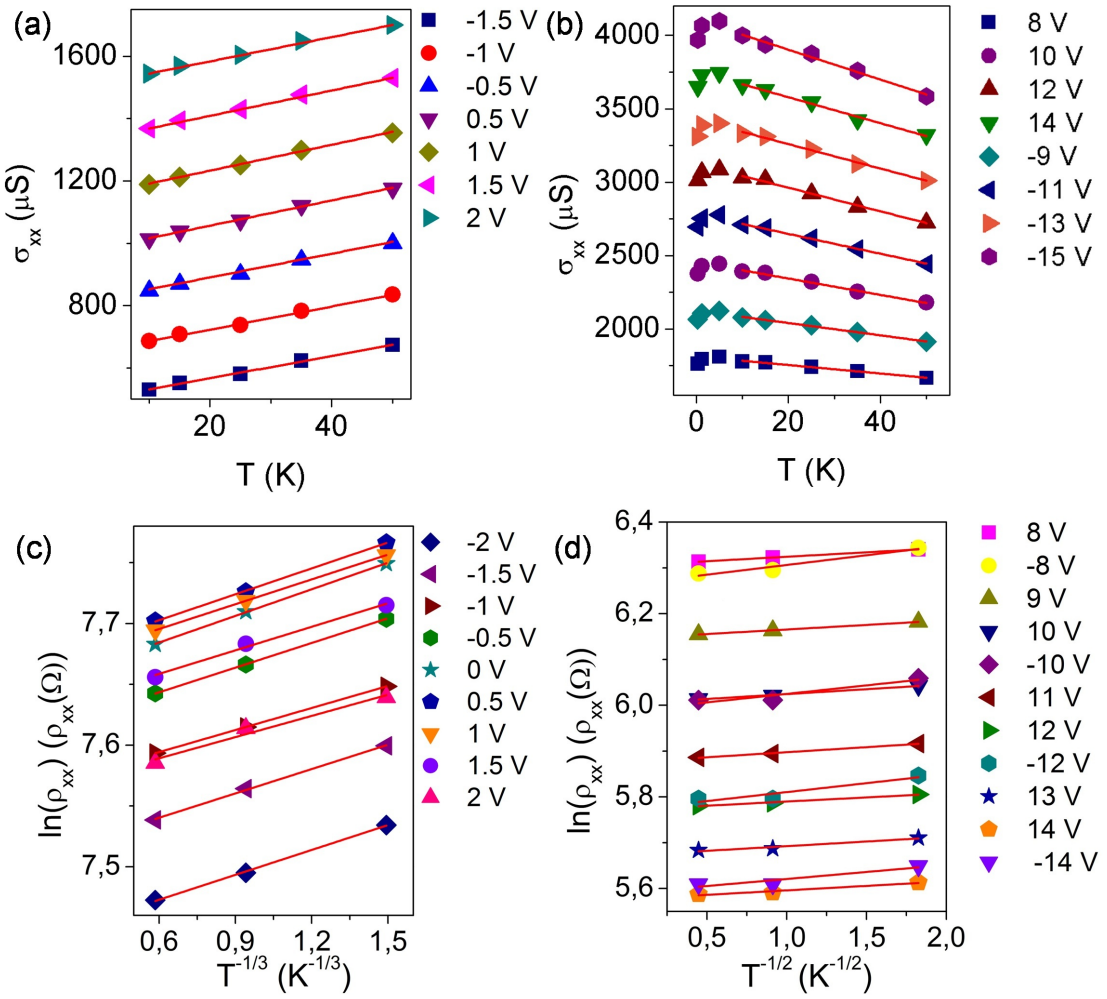

Figure 6.10 (a): Linear σ_{xx} as function of T near the charge neutrality point. (b) Linear σ_{xx} as function of T for $n > n_c$. (c): $\ln \rho_{xx}(T^{-1/3})$ close to the charge neutrality point. (d) Linear dependence of $\ln \rho_{xx}$ with respect to $T^{-1/2}$ for $n > n_c$. Lines are linear fits to our data.

which the symmetry between the layers is broken in the presence of an electric field (done by using two gates) which results in the opening of an energy gap [91, 98].

From the fit we obtained a critical temperature of $T_0 \simeq 0.07$ K, which is one order of magnitude smaller than those previously reported [91]. This implies that in this case, the sample shows a weaker temperature dependence and a larger localization length than those present in double-gated bilayer graphene devices. Nonetheless, we haven't observed the opening of a gap caused by breaking the layer symmetry. In that case, the dependence of ρ_{xx} would follow $\rho_{xx} \propto \exp\left(T^{-1}\right)$. Since the break of the layers' symmetry without magnetic field has only been reported in ultra clean suspended bilayer devices [92, 99] we think that in our sample, such gap is obscured by potential fluctuations, resulting in the localized states that contribute to transport via variable range hopping. This scenario would be, in fact, in agreement with the percolation regime observed in our study of the plateau-plateau quantum phase transitions shown in Chapter 5.

Since hopping between localized states will take place until the thermal energy is above the potential fluctuations, we can use the onset of the variable range hopping to estimate the order of such fluctuations. Indeed, when $k_BT \gtrsim \delta\epsilon$ the thermal energy will start to overcome the potential fluctuations, indicating the point at which the transport stops being mediated by variable range hopping.
The condition $k_BT \gtrsim \delta\epsilon$ yields a fluctuation of the order $\delta\epsilon 0.9$ meV. Since we argue that the gap opened as a consecuence of breaking the layers' symmetry is obscured by the energy fluctuations, this $\delta\epsilon$ also gives an upper limit to the value of the gap. Moreover, $\delta\epsilon$ also allows us to estimate the order of the surface density fluctuations, since $\delta\epsilon \approx h^2\delta n/8\pi m$. The density fluctuations are therefore $\delta n \approx 2.4 \cdot 10^{11}$ cm^{-2}. Since the critical density is $n_c = 2.5 \cdot 10^{11}$ cm^{-2}, it is likely that the metallic behaviour of the sample starts when the density obtained by populating the bands (*i.e.*, applying a gate voltage) overcomes the density fluctuations.

The last regime is that corresponding to low temperature and high density. This regime shows a renormalization from $\rho_{xx} \propto \exp\left((T/T_0)^{-1/3}\right)$ to $\rho_{xx} \propto \exp\left((T/T_0)^{-1/2}\right)$, indicating that Coulomb interaction between localized states must be taken into account [97]. This dependance indicates that at densities above n_c *e*-*e* interaction (or *h*-*h* interaction) becomes dominant, whereas close to the charge neutrality point, the interaction is that of electron-hole puddles.

6.4 Summary and conclusions

In this Chapter we have studied the tranport properties of monolayer graphene on SiO_2 and bilayer graphene enclosed by two *h*-BN flakes when a low (or zero) magnetic field is applied.
Monolayer graphene shows a weak antilocalization to weak localization transition driven by the application of a gate voltage setting the Fermi energy far from the K and K' points, which results in the non linear energy-momentum dispersion (trigonal warping) and, as a consecuence, chirality ceases to be a good quantum number.
For the bilayer graphene device, we have measured the weak localization effect at different temperatures. From these measurements we have obtained the coherence length at different the temperatures, and observed a dependence which obbeys that $L_\phi \propto T^{-p/2}$. By fitting the experimental data to such equation, we have obtained $p = 0.9$.
Finally, we have studied the different transport regimes at zero magnetic field as a function of the temperature and the density. We have observed a ballistic regime when the density is set above certain critical density and temperature (10 K). Below such temperature, the transport becomes dominated by potential fluctuations, leading to a variable

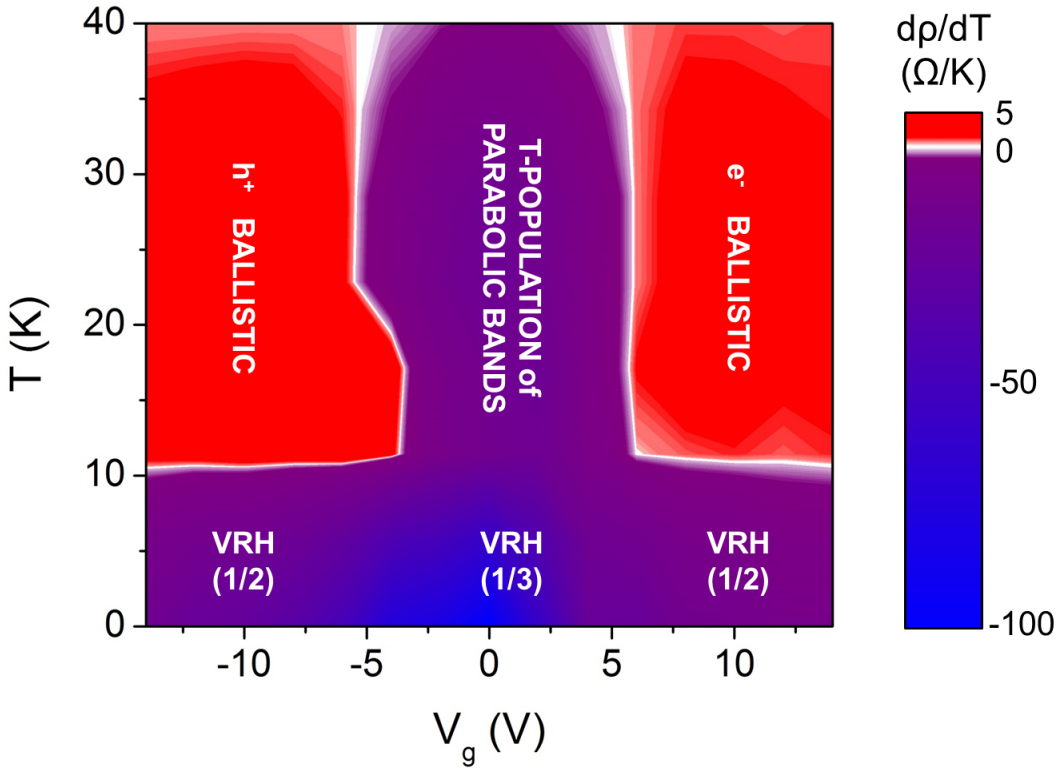

Figure 6.11 Summary of the different transport regimes observed when tuning the density through a critical density (given by the T-independent crossing points of figure 6.8) and the temperature. The reversal of the sign of $\partial\rho_{xx}/\partial T$ indicates a change from ballistic like transport to variable range hopping dominated regime. Image adapted from Ref.[100].

range hopping regime. The different transport regimes at zero field are summarized in figure 6.11.

Chapter 7

Superconductivity in 3D porous graphene

Amongst all the outstanding properties of graphene, there is one property lacking: superconductivity. In this chapter we will show our results on a novel graphene based structure when covered by a superconducting material such as tantalum.

7.1 Introduction

After studying the properties of graphene when placed between two layers of h-BN we aimed to study the interplay of surface effects arising from the interactions between superconducting materials and graphene.
Until now, there have been several studies investigating the behaviour of graphene when interacting with a superconductors [101–103], but most of these studies have shown focused on graphene-superconductor. In particular, pioneering works by Heersche *et al.* [101] studied the Josephson effect in graphene. Other studies have shown how the adsorption of metal adatoms on graphene modifies the electronic transport [104–107], with interesting applications for sensors and energy storage. In fact, it has been shown that lithium decorated graphene shows a higher transition temperature than that of lithium atoms when intercalated in bulk graphite [108].
Since this effect has been shown to be enhanced by the surface of graphene, very interesting approaches have been developed in order to increase the area. In fact, three dimensional graphene structures have been used to study the effect of enhanced area of two dimensional electron systems. These systems, showing a bigger surface area, maintain the electrical and thermal properties of conventional bidimensional graphene. Therefore, they are expected to play an important role in several applications: energy storage, sensors and electronics.
In this Chapter, we will show how these structures are fabricated and the results we have obtained at Sandia National Laboratories.

7.2 Fabrication of 3D porous graphene structures

The three dimensional porous graphene and carbon were fabricated at Sandia National Laboratories by Xiaoyin Xiao following a pioneering technique [109].
The process consists on sputttering nickel three dimensional carbon structures and annealing the structures after the sputtering process. The nickel is then removed by wet etching and as a result, three dimensional graphene structures are obtained. This process is ilustrated in figure 7.1

The porous carbon is fabricated by interference lithography, resulting in a face-centered cubic carbon structure, shown in figure 7.2(A). Then, nickel is sputtered at a rate of 0.5 Å/s during 20 min. Since the structure is porous, the nickel will penetrate into the whole structure, coating the surface even in the bottom layers.

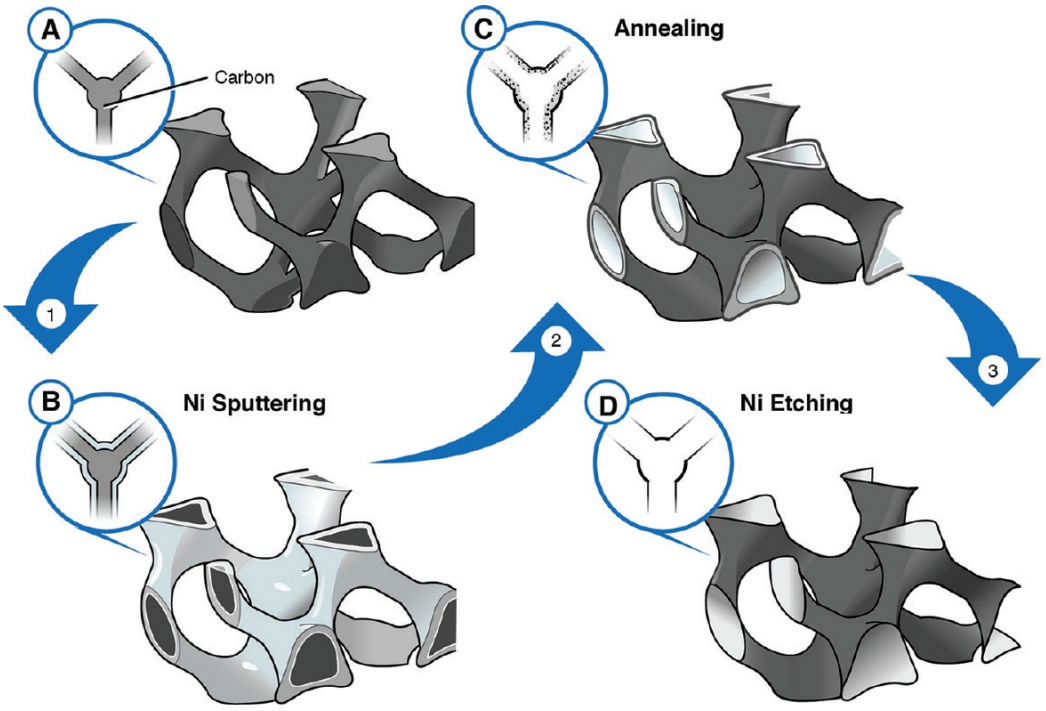

Figure 7.1 Scheme of the fabrication process followed to fabricate 3D porous graphene. (A) Interference lithography is employed in order to fabricate 3D porous carbon. (B) Nickel is sputtered and a film coating of Ni covers the whole surface. (C) The structure is annealed, resulting in the diffusion of carbon atoms into the nickel. (D) Nickel is removed by acidic etching, which results in a 3D graphene structure. Figure adapted from Ref. [109].

By annealing the device at 750 °C in a 5%/95% H_2N_2 atmosphere during 50 min the carbon atoms diffuse into the nickel film coating, converting the sp^3 carbon bonds into sp^2. Finally, the nickel film is etched using a 2 M H_2SO_4 solution during 8 hours. This results in a 3D graphene structure.

Once the 3D graphene structures have been fabricated, they were covered by a thin film (100 nm) of tantalum. For comparison, we studied both tantalum decorated 3D carbon structures and 3D graphene structures. In figure 7.2(A) we show a scanning electron microscopy (SEM) image of the 3D carbon structure prior to the tantalum coating. Fig. 7.2(B) shows that same structure after tantalum has been sputtered. In figure 7.2 we show the three dimensional porous graphene after and before the sputtering of tantalum (figures 7.2 (C) and (D), respectively).

The samples were cleaved to a size of ∼4 mm×4 mm. Eight contacts made using silver epoxy were placed symmetrically around the sample perimeter. The epoxy was cured

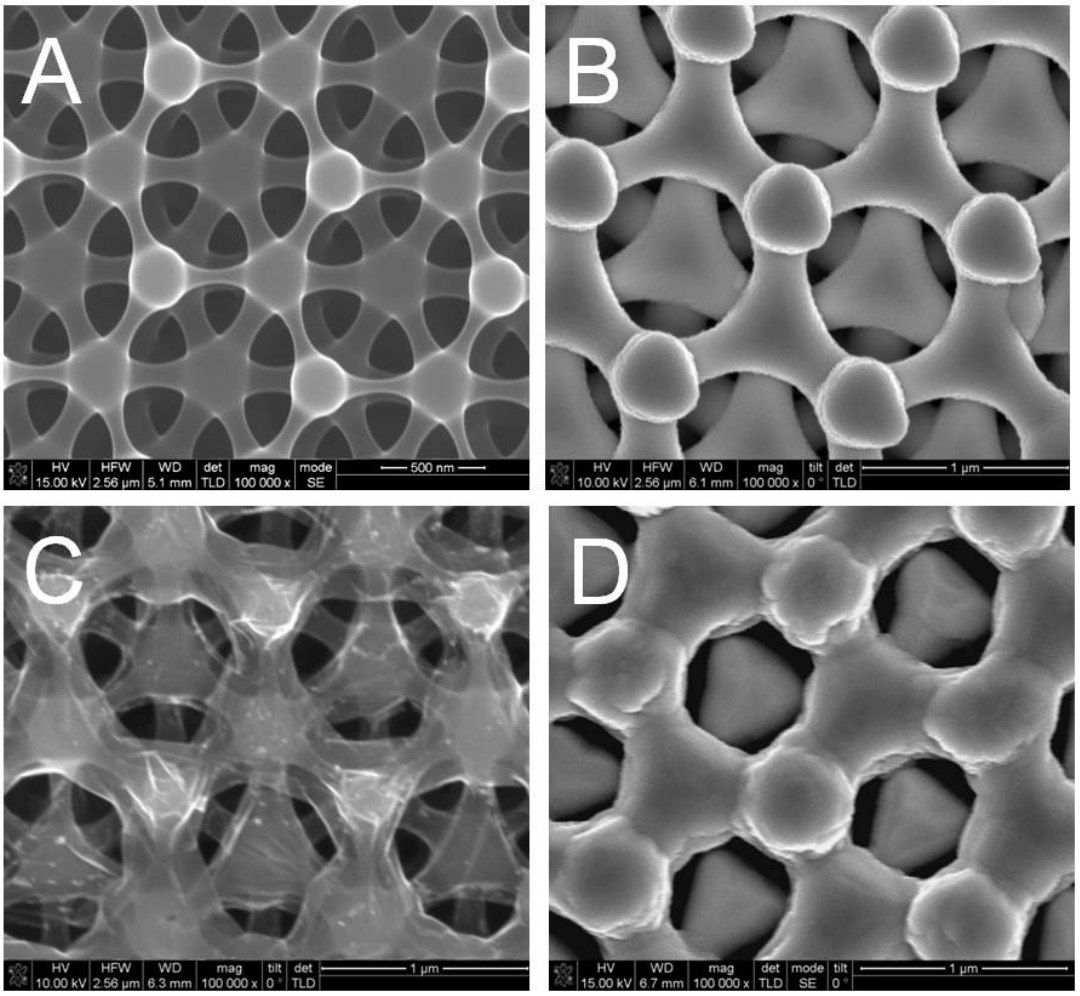

Figure 7.2 (A) SEM image of the 3D porous carbon structure fabricated by interference lithography. (B) SEM image of the 3D porous carbon structure coated by 100 nm of Ta. (C) SEM image of the 3D porous carbon fabricated according to process 7.1. (D) SEM image of the 3D graphene structure coated by 100 nm of Ta.

using a temperature of 60 °C. In figure 7.3 we show an sketch of the geometry of the samples studied.

7.3 Results on Ta decorated 3D porous graphene and 3D porous carbon

The longitudinal resistance of tantalum decorated 3D graphene. We observe a clear superconducting transition at $T_c \sim 1.2$ K, shown in figure 7.4. The resistance at high temperature $\sim 60\ \Omega$ is almost independent on the temperature until the resistance abruptly starts dropping to zero. Defining the critical temperature as the half value of the normal resistance, the critical temperature is found to be $T_c \sim 1.2$ K.

This temperature is smaller than the critical temperature of bulk tantalum, probably

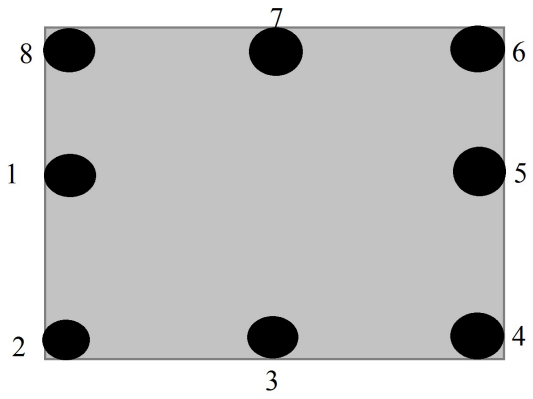

Figure 7.3 Sketch of the geometry used in our samples. Current was injected from contact 1 to contact 5. Longitudinal resistance measurements were taken using the pairs of contacts 8-6 and 2-4, showing the same behaviour.

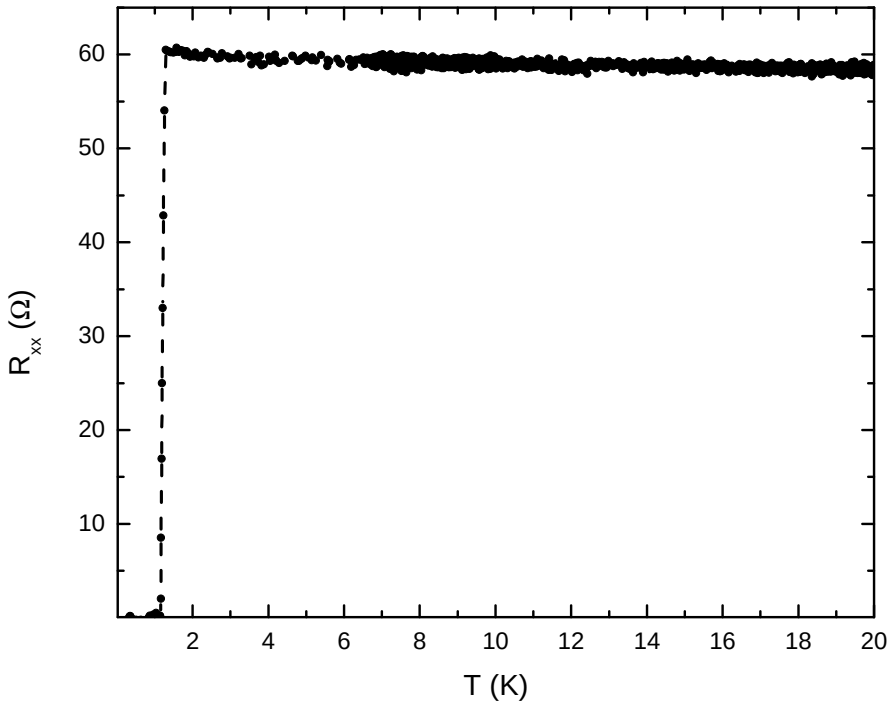

Figure 7.4 R_{xx} as a function of T for a tantalum coated 3D porous graphene structure. The system shows a clear superconducting transition at $T_c = 1.2$ K.

due to the disordered nature in the tantalum coating. Moreover, the width of the superconducting transition is $\Delta T \simeq 150$ mK, larger than that in bulk tantalum ($\simeq 4$ mK [110]).

This critical temperature is in agreement with the critical temperature observed from critical magnetic field measurements (shown in figure 7.5(b)). We also measured the

temperature driven superconductivity transition in a tantalum decorated 3D carbon structure, observing that the critical temperature of $T_c \simeq 1$ K.
Since the tantalum was deposited under the same conditions and at the same time, the possible different of thickness between the two films must be ruled out to explain this difference. In fact, by carefully examining figures 7.2 (B) and (D) we observe that the tantalum film on porous carbon is much smoother than that sputtered on porous graphene. Because of that, it would be expected that the quality of the thin film would be better in porous carbon, and therefore a higher critical temperature should be observed. Nevertheless, the results show an opposite behaviour.
Probably owing to the difference of the carbon bonds (sp^2 in porous graphene and sp^3 in porous carbon) the charge transfer between tantalum and the substrate (porous carbon or porous graphene) follows a different mechanism. In fact, it is known that the substrate greatly influences the strength of the electron-phonon interactions in metal-decorated structures [111]. As a result, probably fewer charges are transferred from the tantalum film to the 3D porous graphene than to the 3D carbon, resulting in a higher critical temperature for the tantalum decorated 3D porous graphene structure.
This is in agreement with a larger Fermi velocity in 3DG-Ta and confirmed by observing the superconductivity transition using a thinner tantalum film. A 20 nm thick film of tantalum was deposited on 3DG and 3DC. We observed a superconducting transition for 3DG covered with this thin film, but no transition was observed for 3DC. Accordingly, the critical temperature for 3DG coated with 20 nm of tantalum was $T_c \sim 0.75$ K.

In figure 7.5(a) we show the magnetoresistance at temperatures from 6.01 K to 0.36 mK. We have normalized the magnetoresistance to that at a magnetic field at which the tantalum is in normal state. We can observe that at the lowest temperature (0.36 mK) the resistance is zero at low magnetic fields. When the magnetic field is increased above $\gtrsim 1.4$ T, the resistance abruptly increases, being constant once the tantalum is in normal state. This observation evidences the field induced destruction of the superconducting state. By defining the critical magnetic field as the highest magnetic field at which the material is still in superconducting state, *i.e.*, at which $R_{xx}/(R_{xx})_N = 0$, we are able to study the dependence of the critical magnetic field on the temperature. Indeed, in figure 7.5(b) we observe that the higher the temperature is, the lower the critical magnetic field. We can fit these data following the standard Ginzberg-Landau theory for isotropic superconductors, namely [112]

$$H_{2c} = \frac{\phi_0}{2\pi\xi(0)^2} \cdot \left(1 - \frac{T}{T_c}\right) \tag{7.1}$$

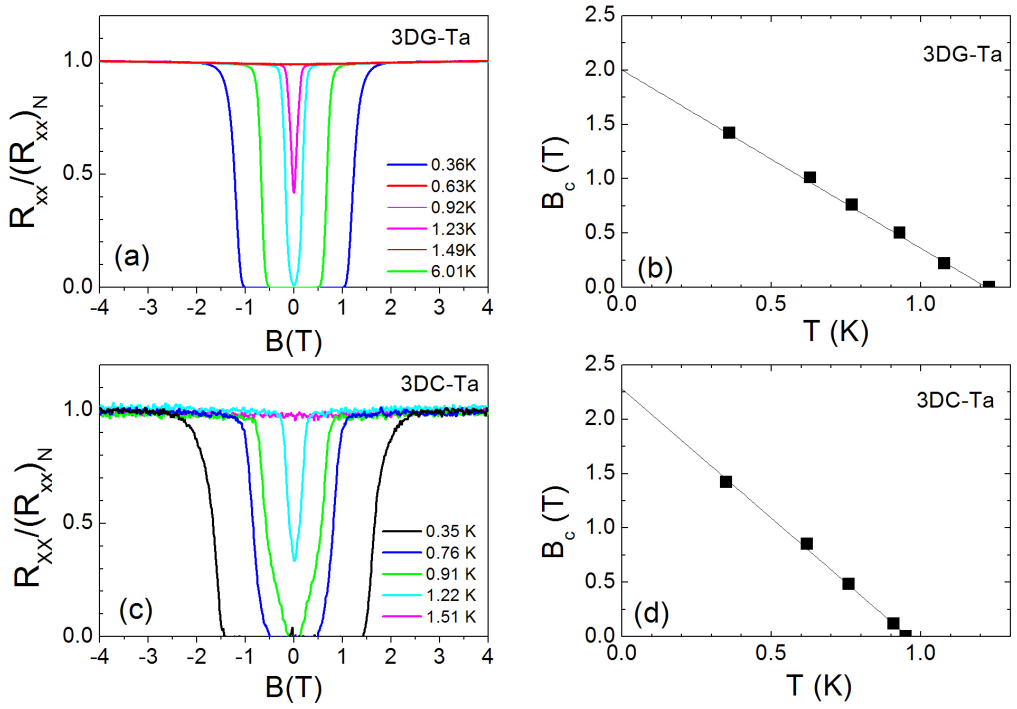

Figure 7.5 (a) Normalized magneto resistance at a few selected temperatures for 3DG-Ta. (b) Critical magnetic field obtained from the set of data illustrated in (a) as a function of the temperature and its linear fit. Panels (c) and (d) show similar sets of data for 3DC-Ta than (a) and (b), respectively. Lines in (b) and (d) are linear fits.

Where $\phi_0 = h/2e$, the flux quantum and $\xi(0)$ is the superconducting coherence length at T=0. From figure 7.5 we observe that indeed B_c follows a linear dependence on the temperature. From the fitting, a critical temperature $T_c = 1.22$ K is obtained, being consistent with that shown in figure 7.4. $\xi(0)$ is ~ 14 nm, much smaller than the coherence superconducting length in bulk tantalum (93 nm), again due to the disordered nature of the film. Also, the zero temperature critical magnetic field is roughly 2 T, whereas the zero temperature critical magnetic field in bulk tantalum is about 800 Ga[113]. In contrast, the results obtained for the tantalum film on 3D porous carbon show a lower critical temperature (0.96 K) and a higher critical magnetic field (2.3 T) at T=0.
The Fermi velocity can be calculated from $\xi(0)$ by means of the relation [112]

$$\xi(0) = \frac{\hbar v_F}{1.76\pi k_B T_c} \tag{7.2}$$

Using eq. 7.2 we obtain a Fermi velocity $v_F \sim 1.2 \cdot 10^4$ m/s for 3DG-Ta, whereas for 3DC-Ta it is $v_F \sim 0.8 \cdot 10^4$ m/s. This is probably due to the fact that there are less charges being transferred from tantalum to the sp^2 graphene than to the sp^3 carbon. Moreover, in both cases, the Fermi velocity is one order of magnitude lower than in bulk tantalum,

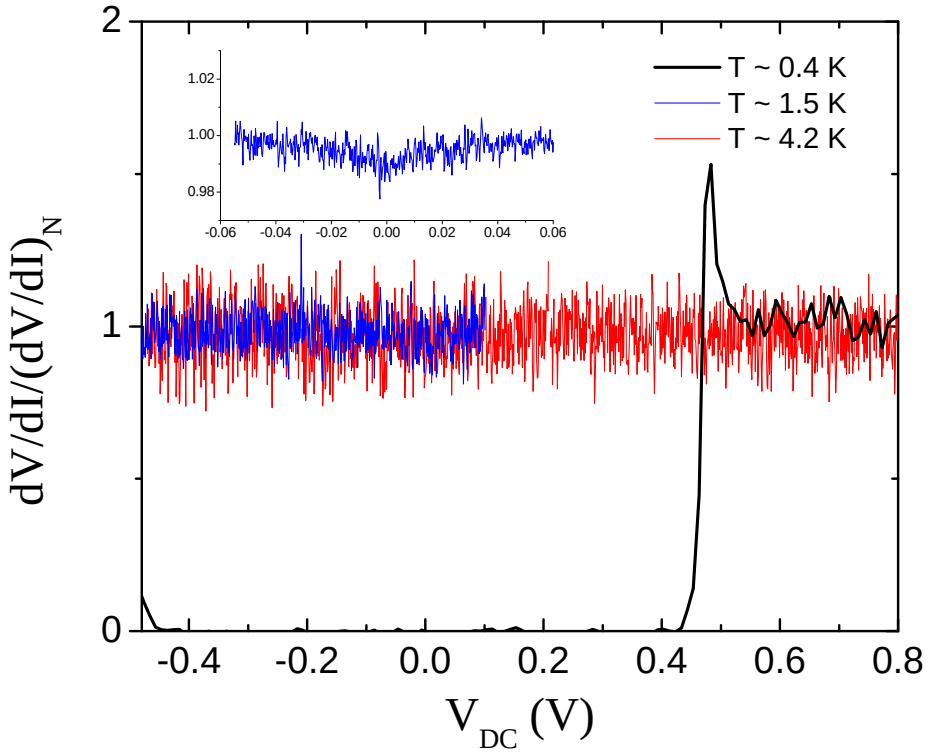

Figure 7.6 Normalized differential resistance as a function of the DC bias at different temperatures.

where if $\xi(0) = 93$ nm and $T_c = 4.47$ K are assumed [110, 113], $v_F \sim 3 \cdot 10^5$ m/s.
Finally dV/dI measurements were performed. This measurement was done as follows: a sweeping DC bias (V_{DC}) is applied in combination with a small AC bias ($\delta V_{AC} = 10\ \mu$V) between contacts 1 and 5 in series with a 100 Ω resistor, measuring dV/dI between contacts 2 and 4.
In figure 7.6 we show the normalized differential resistance $(dV/dI)/(dV/dI)_N$ as a function of V_{DC} in tantalum decorated 3D porous graphene at three temperatures. At temperatures higher than the critical temperature, the differential resistance is constant over the whole bias range. Nevertheless, when the temperature is close to the critical temperature, a weak dip appears at $V_{DC} = 0$ V (see inset in figure 7.6). If the sample is further cooled down, the dip reaches zero for a bias $|V_{DC}| \leq 0.43$ V. If the contact resistance is considered, the critical current can be estimated to be $i_c \sim 1$ mA.

7.4 Summary and conclusions

We have shown some of the results obtained during a three months stage at Sandia National Laboratories where the superconducting properties of thin tantalum films were

deposited on three dimensional carbon and graphene structures. The interplay between the tantalum and the sp^3 (carbon) bonds and sp^2 (graphene) bonds probed to be essential in understanding the differences between the quantitatively different results.

Chapter 8

Conclusions and open questions

This Thesis has been devoted to the study of the transport properties of graphene as function of parameters such as the temperature, the magnetic field and the carrier density.

We have learnt how to successfully exfoliate and fabricate graphene nanodevices with channel dimensions down to 45 nm wide. In order to achieve this, several attempts were made: we tried using different resists for the lithography process and optimised our technique to process graphene. We have also learnt that it is usually desirable to start with the etching of the graphene, so that the graphene surface underneath the titanium is as small as possible: this reduces the risk of losing the metal which makes up the contacts. Although during the time we have made great improvements fabricating the devices in terms of the size of the graphene flakes, the time spent in the fabrication and the overall behaviour of the sample (density and mobility); more work needs to be devoted in achieving a fully reproducible method and make exfoliated graphene suitable for industrial purposes.

We have studied the quantum Hall effect in monolayer, bilayer on SiO_2 and h-BN and trilayer on SiO_2 , but the answer addressing the existence of the quantum Hall effect in four layered graphene is still opened. Since the only studied device showed to be highly doped, the possibility of a quantized Hall resistivity should not be ruled out until four layered graphene devices showing less dopants and better quality are successfully fabricated and characterized. This can be done placing the graphene flake on top of hexagonal boron nitride (since, as we have shown, it greatly enhances the mobility and decreases the unwanted doping) or suspending the graphene flake.

These high quality devices will also be helpful in understanding the quantum phase transitions in graphene. From our experiments, the critical exponent of a number of plateau-plateau transitions showed to be independent of the density and the filling factor, being $\gamma \approx 1.5$. We have obtained the critical exponent following two independent approaches. One of them relied upon the scaling of $\left(\partial\rho_{xy}/\partial B\right)_{max} \propto T^{-\kappa}$ close to the critical point. From this expression we have extracted $\kappa \sim 0.3$, which combined with our experiments on weak localization yields $\gamma = 1.5 \pm 0.1$.
Studying the conductivity in the tails of the Landau levels, *i.e.,* in the variable range hopping regime, the critical exponent γ can be obtained by fitting the conductivity with respect to the temperature according to $\sigma_{xx} \propto \exp\left(-\sqrt{T_0/T}\right)/T$, and the dependance of T_0 with respect to γ is $T_0 \propto |\nu - \nu_c|^{\gamma}$. Using this approach we have obtained $\gamma = 1.4 \pm 0.2$. This result is compatible not only with the previously obtained value of $\gamma = 1.5 \pm 0.1$, but also with a localization-delocalization transition driven by a percolation regime.

Though this results suggests that transport mechanisms are mainly governed by long range scattering, it is not yet known if this is the case for every bilayer graphene sample enclosed by hexagonal boron nitride or this is a sample dependent effect. Thus, the impact that dopants might have in the transitions in graphene is not yet understood and further studies in a bigger number of samples must be done. Additionally, the possibility to effectively control the number and kind of dopants, as done by Li *et al.* [69] could shed more light to this problem.
Also, since the quantization of R_{xy} in graphene depends on the number of layers, the criticality of the localization-delocalization transition should be studied in trilayer graphene devices and, if quantization persists, in four layered devices.

In order to gain more insight of the transport regimes in graphene and the impact of dopants, we have studied two graphene devices at low and zero magnetic field. The monolayer device on SiO_2 showed both weak antilocalization and weak localization at higher gate voltages, which implies that at high Fermi energy the energy-momentum dispersion ceases to be linear, and therefore the chirality cannot be considered as a good quantum number.
Regarding the bilayer graphene device enclosed by h-BN , we have extracted the inelastic scattering exponent p ($l_\phi \propto T^{-p/2}$) whose value was found to be $p = 0.90 \pm 0.02$. Additionally, we have characterized and found a number of transport regimes driven by the density and temperature. This characterization yields information in the understanding of the transport mechanisms in bilayer/h-BN heterostructures. Such information is useful as it helps finding the best conditions at which these heterostructures will show a better performance in terms of electronic application.

More applications can be found if the interaction between graphene and other materials is studied. In Chapter 7 we have shown the differences in the superconductivity properties of a thin film on tantalum depending on whether it is evaporated on top of graphene or carbon. We have explained how these devices were fabricated and studied the superconducting properties of a thin film of tantalum sputtered on top of 3D graphene and 3D carbon. We have observed that the difference between the sp^3 bonds in 3D porous carbon and sp^2 in porous graphene affects the superconducting properties of a thin film of tantalum, namely the critical temperature and the critical magnetic field at T=0. The Fermi velocity in the thin tantalum films is also affected by the material underneath it.

Additionally, there have been a few of studies which we could not complete. The main reason for that is the important bottleneck that we have found in the fabrication of

the devices. Since the only possibility of access to clean room facilities was that of two weeks per semester, the number of working devices was not as big as it is desirable. Now that the University of Salamanca is installing a clean room, we could work on unfinished studies and start new ones. For example, we had a critical point drier installed at our laboratory, but the lack of continued access to a clean room prevented us from fabricated suspended devices. Obtaining such devices would allow us to study the fractional quantum Hall effect in graphene and, since it eliminates the interaction with the substrate, it would also allow to study the quantum phase transitions in pristine graphene. Also, with a clean room, we would have the possibility to devote more time to fabricate complicated devices such as Corbino rings. Also, we could process more monolayer-bilayer junctions until obtaining a high quality one, and then proceed to the study of the quantum Hall regimes in these systems.

Furthermore, we would like to study CVD graphene, since it allows an scalable route to graphene-based electronics and transistors. It would also allow us to fabricate devices following a same procedure, which would be useful in the standarization of graphene devices and the standarization of resistance measures.

Finally, the techniques that we have used in graphene could easily be applied to different bidimensional systems. In particular, I would like to study with other 2D materials, such as MoS_2. MoS_2 can be exfoliated similarly to graphene, obtaining a bidimensional material. Also, since it is a semiconductor with a direct gap of 1.2 eV we could circumvent the problems of field effect transistors based on graphene whilst, at the same time, taking benefit of its reduced thickness.

Appendix A

Introducción y motivación de la Tesis

En una revolucionaria e inspiradora charla richard Feynman aseguró que "había mucho espacio al fondo"[1]. ¿Qué significa esto? En 1959 investigadores y científicos habían empezado a desarrollar el estudio de microeléctroniac y la miniaturización de chips. Aún asi, Feynman sabía que el camino acaba de abrirse.

Los científicos consiguieron confinar electrones en un espacio de unos pocos nanómetros, forzando a los electrones a moverse en un plano debido al confinamiento cuántico. Dicho confinamiento resulta en un comportamiento radicalmente distinto del observado materiales tridimensionales. Por ejemplo, el descubrimiento del efecto Hall cuanto en 1980 reveló que, de hecho, el confinamiento de portadores de carga lleva a nuevos efectos.

La observación del efecto Hall cuántico fue la piedra angular de una nueva línea de investigación en Física. En efecto, las muestras se mejoraron y la observación del efecto Hall cuantico fraccionario en 1982 abrió aún mas preguntas, dado que esta consecuenta de la interacción de muchos cuerpos afecta profundamente el comportamiento de la materia.

El efecto Hall cuántico es un fenómeno cuántico observable en sistemas macroscópicos. Se basa en el hecho de que cuando se aplica un campo magnético perpendicular a un gas bidimensional de electrones se consigue una cuantización adicional. Como consecuencia, si se inyecta una corriente a través de la muestra y se mide la resistencia perpendicularmente a la dirección de la corriente, se observa que dicha resistencia está cuantizada en una serie de plateaus. Poco después del descubrimiento del efecto Hall cuantico se entendió que el transiente entre dos plateaus indicaba una transición de localización-deslocalización. Es mas, se observó que dichos plateaus se cuantizaban tomando los mismos valores independientemente de la muestra, que se convirtió en un hecho de crucial importancia en el estudio de las propiedades fundamentales de la materia y en metrología.

[1] "There's plenty of room at the bottom"

Aún asi, aunque la resistencia sigue la misma cuantización independientemente de la muestra, pronto se observó que el transiente entre dos plateaus (es decir, cada transición de fase cuántica) no eran necesariamente iguales para las distintas muestras. De hecho, esto abrió el debate con respecto al hecho de si las transiciones de fase cuanticas siguen algún comportamiento universal y, de ser así, bajo qué condiciones.

Por otra parte, en el trabajo seminal de P.R. Wallace, se encontró que cuando una lámina de grafito se aisla, los electrones en dicha lámina siguen la ecuación de Dirac en lugar de la ecuación de Schrödinger. El propósito de Wallace era establecer un punto de partida para entender las propiedades del grafito (material candidato a ser usado en eléctronica). No sé podía imaginar que su trabajo sería el que inspirara la búsqueda del alótropo bidimensional del carbono: el grafeno.
En efecto, a finales del siglo XX, alótropos 0D y 1D del carbono (fullerenos y nanotubos de carbono) ya habían sido aislados y su investigación revelaba prometedores e interesantes resultados. A pesar de ello, el alótropo 2D tenía que esperar para ser encontrado. Fue en el año 2004 cuando Geim y Novoselov encontraron, con algo de fortuna, que la cinta adhesiva podía romper de forma efectiva el grafito, separando las láminas entre sí hasta, eventualmente, aislar una sola lámina de grafito. A esta lámina monoatómica de grafito se la llamó grafeno.
El grafeno se convirtió rápidamente en uno de los temas más investigados en Física. Y no sin razón. Para empezar, es realmente un material de espesor atómico. Había, ciertamente, mucho espacio al fondo. Además, es tambien un material puramente bidimensional, de forma que efectos como el anteriormente mencionado efecto Hall cuántico podían ser investigados sin la necesidad "artificial" de confinar a los electrones.
Además, el grafeno demostró rápidamente ser un material prometedor en cuanto a aplicaciones se refiere: es uno de los materiales mas duros conocidos, es un increíble conductor de electricidad y su reducido espesor podría ser la solución para una mayor miniaturización de microchips. Más aún, es un semiconductor sin gap y en el que el tipo de portadores (huecos o electrones) de carga puede variarse simplemente con la aplicación de un campo eléctrico perpendicular a la muestra. Ademas, el hecho de que los electrones obedezcan la ecuación de Dirac, abre la posibilidad de estudiar ciertos fenómenos de la electrodinámica cuantica sin la necesidad de recurrir a grandes instalaciones como el Gran Colisionador de Hadrones[2].

En esta Tesis hemos estudiado las propiedades fundamentales de grafeno, estudiando las transiciones de fase cuántica y clarificando el debate sobre la universalidad. Tambien

[2]Large Hadron Collider en inglés

hemos estudiado sus regímenes de transporte en dispositivos de alta mobilidad, añadiendo información relevante para futuras aplicaciones en el sentido de que regímenes de transporte bien diferenciados se pueden modificar con la simple variación de temperatura y densidad. Finalmente, hemos estudiado como los enlaces sp^2 en el grafeno afectan las propiedades superconductoras del tántalo, en oposición a los enlaces sp^3.

Esta Tesis está organizada de la siguiente manera:

- En el Capítulo 2 introducimos las principales propiedades del grafeno y discutimos las diferentes maneras en que los investigadores and conseguido producirlo. Obviamente, cada método tiene sus ventajas e inconvenientes, que también se han comentado. También hemos ilustrado en detalle el proceso de fabricación en sala blanca usado para fabricar los dispositivos que hemos investigado. Enseñaremos algunos de nuestros dispositivos y comentaremos las geometrías de cada uno.

- El Capítulo 3 está dedicado a las técnicas experimentales que nos han permitido realizar nuestro estudio. En concreto, enseñaremos los principios físicos de funcionamiento de los criostatos utilizados, prestando especial atención a los sistemas *cryofree* utilizados en el Laboratorio de Bajas Temperaturas de Salamanca. También explicaremos los diferentes tipos de imán utilizados en nuestros experimentos.

- En el Capítulo 4 enseñaremos y explicaremos el efecto Hall cuántico medido en dispositivos III-V y grafeno. En particular, enseñaremos el efecto Hall cuántico en grafeno bicapa y tricapa, mostrando la cuantización de la resistencia y como se puede extraer información sobre las propiedades de estos materiales a través de estas medidas.

- Extenderemos nuestro estudio del efecto Hall cuántico a la caracterización de las transiciones de fase cuánticas plateau-plateau en un dispositivo de grafeno bicapa de alta mobilidad. En el Capítulo 5 mostraremos nuestros resultados de la transición de fase plateau-plateau, revelando una no universalidad de la transición localización-deslocalización.

- El régimen opuesto al del efecto Hall cuántico se estudiará en el Capítulo 6. En este Capítulo estudiaremos el comportamiento de grafeno cuando se aplica un pequeño campo magnético. Hemos observado una transición de localización débil a antilocalización débil en grafeno monocapa. En grafeno bicapa, hemos identificado varios regímenes de transporte dirigidos por una modificación de la temperatura y la densidad de portadores.

- En una estancia de tres meses de duración en el Laboratorio Nacional de Sandia[3] tuve la oportunidad de investigar las propiedades superconductoras de una fina película de tántalo sobre grafeno tridimensional poroso y carbono tridimensional poroso. El proceso de fabricación, asi como los resultados de estos experimentos se mostrarán en el Capítulo 7.

- En el Capítulo 8 discutiremos las conclusiones generales a este trabajo, resaltando los aspectos mas importantes.

- Finalmente se incluyen dos Apéndices con las traducciones al español de los Capítulos 1 y 8 para optar al doctorado con *Mención de "Doctorado Internacional"*.

[3]Sandia National Laboratories

Appendix B

Resumen y conclusiones de la Tesis

Esta Tesis se ha dedicado al estudio de las propiedades de transporte en grafeno como función de parámetros tales como la temperatura, el campo magnético y la densidad de portadores.

Hemos aprendido como exfoliar y fabricar nanodispositivos de grafeno con una anchura de canal de 45 nm. Para conseguir esto se hicieron varios intentos probando diferentes resinas hasta encontrar que la óptima para el procesado de grafeno es PMMA. También hemos aprendido que por lo general es mejor empezar el proceso de fabricación con el ataque de grafeno, de forma que la superficie de grafeno por debajo del titanio es la menor posible: esto disminuye las probabilidades de perder el metal que forma los contactos. Aunque durante el tiempo empleado en ganar experiencia en la fabricación de dispositivos hemos hecho grandes avances; en términos del tama no de los copos de grafeno exfoliado, el tiempo empleado en la fabricación y en el comportamiento general de la muestra (en mobilidad y densidad), hay que dedicar más esfuerzos en conseguir un método de fabricación completamente reproducible y escalable a nivel industrial.

También hemos enseñado que el efecto Hall cuántico depende del número de capas del dispositivo. Hemos mostrado el efecto Hall cuantico en grafeno bicapa y tricapa sobre un sustrato de SiO_2 , pero la respuesta a la existencia una resistencia cuantizada en grafeno de cuatro capas aún está sin responder. Dado que el único dispositivo estudiado estaba altamente dopado, la posibilidad de que exista una resistencia Hall cuantizada no debería descartarse hasta estudiar dispositivos de mayor calidad. Esto podría conseguirse depositando el grafeno sobre nitruto de boro (dado que, como hemos ense nado, aumenta la mobilidad y disminuye las impurezas dopadas) o suspendiendo el grafeno.

Estos dispositivos de alta calidad serán tambien útiles para entender las transiciones de fase cuánticas en grafeno. Gracias a nuestros experimentos, hemos demostrado que el exponente crítico de varias transiciones plateau-plateau son independendientes tanto de la densidad de portadores como del factor de llenado, y vale $\gamma \approx 1.5$. Hemos obtenido el exponente crítico siguiendo dos técnicas independientes. Una de ellas se basa en la técnica de scaling de $(\partial\rho_{xy}/\partial B)_{max} \propto T^{-\kappa}$ cerca del punto crítico. A través de esta expresión obtenemos $\kappa \sim 0.3$, que combinado con nuestros experimentos de localización débil lleva a $\gamma = 1.5 \pm 0.1$.
Estudiando la conductividad en las colas de los niveles de Landau, es decir, en el régimen de *variable range hopping*, el exponente crítico γ se puede obtener considerando que $\sigma_{xx} \propto \exp\left(-\sqrt{T_0/T}\right)/T$ y que la dependencia de T_0 con γ viene dada por $T_0 \propto |\nu - \nu_c|^{\gamma}$. Utilizando esto hemos obtenido $\gamma = 1.4 \pm 0.2$. Este resultado es compatible, no sólo con el resultado anterior de $\gamma = 1.5 \pm 0.1$, sino también con una transición localización-delocalización dominada por un régimen de percolación.
Aunque este resultado sugiere que los mecanismos de transporte esta dominados principlamente por desorden de largo alcance, aun no se ha determinado si éste es el caso general para grafeno bicapa entre dos copos de nitruro de boro o es un fenómeno que depende de la muestra. Así pues, el efecto que los dopantes pueden tener en las transiciones en grafeno no está completamente entendido y hace falta a nadir más estudios en esta dirección estudiando un mayor número de muestras. Adicionalmente, la posibilidad de controlar el número y tipo de dopantes, como hicieron Li *et. al* [69] podría ser de gran utilidad.
También, dado que la cuantización de R_{xy} en grafeno depende del número de capas, la criticalidad de las transiciones localización-delocalización debería estudiarse en dispositivos tricapa y, de haber aun cuantización, en dispositivos de cuatro capas.

Para entender mejor los regímenes de transporte en grafeno y el efecto de los dopantes, hemos estudiado dos dispositivos de grafeno a bajo y cero campo magnético. El dispositivo de grafeno monocapa sobre SiO_2 mostraba antilocalización débil y localización débil a mayores potenciales de puerta, que implica que a altas energías de Fermi la relación energía-momento deja de ser lineal y por tanto la quiralidad deja de ser un buen número cuántico.
En cuanto al dispositivo de grafeno bicapa encerrado por dos copos de h-BN , hemos extraído el exponente de dispersión inelástica p ($l_\phi \propto T^{-p/2}$), cuyo valor es $p = 0.90 \pm 0.02$. Ademas, hemos caracterizado y encontrado diferentes regímenes de transporte gobernados por la densidad y la temperatura. Esta caracterización proporciona información útil para entender cuales son los mecanismos principales de transporte en heteroestructuras de grafeno bicapa y nitruro de boro. Dicha información puede ayudar a encontrar

las condiciones óptimas en cuanto a aplicaciones en industra electrónica de dichas heteroestructuras.

Aún mas aplicaciones se pueden encontrar si se estudia la interacción entre el grafeno y otros materiales. En el Capítulo 7 hemos enseñado las diferencias en las propiedades superconductoras de una fina lámina de tántalo en función de si está depositada sobre grafeno o sobre carbono. Hemos explicado el proceso de fabricación de dispositivos de carbono y grafeno tridimensional poroso y estudiado las propiedades de superconductividad de tántalo sobre estos materiales. Hemos observado que la diferencia entre los enlaces sp^3 en el carbono tridimensional poroso frente los enlaces sp^2 de grafeno tridimensional poroso afecta de manera distinta las propiedades del tántalo, variando la temperatura crítica y el campo magnético crítico a T=0. Tambien hemos visto que la velocidad de Fermi estas láminas de tántalo se ven afectadas por el material que se encuentre debajo.

Además, hay estudios que no hemos podido completar. La principal razón para esto ha sido el gran cuello de botella que hemos encontrado a la hora de fabricar las muestras. Dado que únicamente teníamos acceso a la sala blanca dos semanas por semestre, el número de muestras disponible no ha sido tan alto como es deseable. Ahora que la Universidad de Salamanca está finalizando la instalación de una sala blanca, podríamos continuar trabajo que no fueron finalizados y empezar nuevas líneas de investigación.
Por ejemplo, adquirimos una secadora de punto crítico y la instalamos en nuestro laboratorio, sin embargo, por carecer de acceso continuado a una sala blanca no pudimos procesar dispositivos suspendidos. Procesar estos dispositivos nos permitiría estudiar el efecto Hall fraccionario en grafeno y, dado que elimina la interacción con el substrato, también nos permitiría estudiar las transiciones de fase cuánticas en grafeno puro.
Además, con una sala blanca, tendríamos la posibilidad de dedicar más tiempo a fabricar dispositivos complicados, tales como los anillos de Corbino. También podríamos procesar uniones monocapa-bicapa hasta obtener una muestra de buena calidad y proceder al estudio del transporte en el régimen Hall cuántico en estos sistemas.
También me gustaría estudiar el grafeno CVD en profundidad, dado que permite una ruta escalable de acceso a dispositivos electrónicos y transistores basados en grafeno. Además, la fabricación de grafeno en un proceso controlado, permitiría la reproducibilidad del proceso y la standarización de dispositivos de grafeno y la unidad de resistencia.
Finalmente, las técnicas que hemos utilizado con el grafeno podrían ser aplicadas para la fabricación de otros sistemas bidimensionales. En particular, me gustaría trabajar con MoS_2, que puede ser exfoliado de forma similar al grafeno y formar láminas de espesor atómico. Además, como es un semiconductor con gap directo de 1.2 eV, podríamos evitar los problemas que presenta el grafeno a la hora de obtener transistores eficientes, pero manteniendo las ventajas de ser materiales bidimensionales y de espesor atómico.

Appendix C

List of publications

- *C. Cobaleda*, X. Xiao, D. B. Burckel, R. Polsky, D. Huang, E. Diez and W. Pan "Superconducting properties in Tantalum decorated three-dimensional graphene an carbon structures" (submitted to Applied Physics Letters)
- *C. Cobaleda*, S. Pezzini, A. González, E. Diez and V. Bellani "Percolation transitions in bilayer graphene enclosed by hexagonal boron nitride" (submitted to Physical Review Letters)
- C. H. Fuentevilla, J. D Lejarreta, *C. Cobaleda* and E. Diez "Angle dependent conductivity in graphene FET transistors" (submitted to Solid State Electronics)
- *C. Cobaleda*, S. Pezzini, E. Diez and V. Bellani "Temperature- and density-dependent transport regimes in a h-BN/bilayer graphene/h-BN heterostructure" *Physical Review B* **89** 121404R (2014)
- *C. Cobaleda*, E. Diez, M. Amado, S. Pezzini, F. Rossella, V. Bellani, D. López-Romero and D. K. Maude "Quantum Hall effect in monolayer, bilayer and trilayer graphene" *J. Phys.: Conf. Ser.* **456** 012006 (2013)
- S. Pezzini, *C. Cobaleda*, E. Diez and V. Bellani "Disorder and de-coherence in graphene probed by low-temperature magneto-transport: weak localization and weak antilocalization" *J. Phys.: Conf. Ser.* **456** 012032 (2013)
- S. Pezzini, *C. Cobaleda*, E. Diez and V. Bellani "Quantum interference corrections to magnetoconductivity in graphene" *Physical Review B* **85**, 165451 (2012)
- *C. Cobaleda*, F. Rossella, S. Pezzini, E. Diez, V. Bellani, D. K. Maude and P. Blake "Quantum Hall effect in bilayer and trilayer graphene" *Phys. Status Solidi C* **9**, 1411-1414 (2012)

- *C. Cobaleda*, F. Rossella, S. Pezzini, E. Diez, V. Bellani, D. K. Maude and P. Blake "Quantum hall effect in inhomogeneous trilayer graphene" *Physica E* **44** 530-533 (2011)

Bibliography

[1] Richard P. Feynman. There's plenty of room at the bottom. In *Caltech Engineering and Science*, volume Volume 23, pages 22–36, 1959. URL `http://calteches.library.caltech.edu/47/2/1960Bottom.pdf`.

[2] K. von Klitzing, G. Dorda, and M. Pepper. New method for high-accuracy determination of the fine-structure constant based on quantized hall. *Physical Review Letters*, 45:494–497, 1980. doi:10.1103/PhysRevLett.45.494.

[3] D. C. Tsui, H. L. Stormer, and A. C. Gossard. Two-dimensional magnetotransport in the extreme quantum limit. *Physical Review Letters*, 48:1559, 1982. doi:10.1103/PhysRevLett.48.1559.

[4] H. P. Wei, D. C. Tsui, and A. M. M. Pruisken. Localization and scaling in the quantum hall regime. *Physical Review B*, 33:1488, 1986. doi:10.1103/PhysRevB.33.1488.

[5] Richard E. Prange and Steven M. Girvin, editors. *The Quantum Hall Effect*. Springer-Verlag, 1987.

[6] P. W. Anderson. Absence of diffusion in certain random lattices. *Physical Review*, 109:1492, 1957. doi:10.1103/PhysRev.109.1492.

[7] E. Abrahams, P. W. Anderson, D. C. Licciardello, and T. V. Ramakrishnan. Scaling theory of localization: Absence of quantum diffusion in two dimensions. *Physical Review Letters*, 42:673, 1979. doi:10.1103/PhysRevLett.42.673.

[8] P. R. Wallace. The band theory of graphite. *Physical Review*, 71:622, 1947. doi:10.1103/PhysRev.71.622.

[9] H. W. Kroto, J. R. Heath, S. C. O'Brien, R. F. Curl, and R. E. Smalley. C_{60}: Buckminsterfullerene. *Nature*, 318:162–163, 1985. doi:10.1038/318162a0.

[10] S. Iijima. Helical microtubules of graphitic carbon. *Nature*, 354:56–58, 1991. doi:10.1038/354056a0.

[11] S. Iijima and T. Ichinashi. Single-shell carbon nanotubes of 1 nm diameter. *Nature*, 363:603–605, 1993. doi:10.1038/363603a0.

[12] K. S. Novoselov, A. K. Geim, S. V. Morozov, D. Jiang, Y. Zhang, S. V. Dubonoz, I. V. Grigorieva, and A. A. Firsov. Electric field effect in atomically thin carbon films. *Science*, 306:666–669, 2004. doi:10.1126/science.1102896.

[13] Y. Zhang, YW Tan, H. L. Stormer, and P. Kim. Experimental observation of the quantum hall effect and berry's phase in graphene. *Nature*, 438:201–204, 2005. doi:10.1038/nature04235.

[14] A. K. Geim and K. S. Novoselov. The rise of graphene. *Nature Materials*, 6: 183–191, 2007. doi:10.1038/nmat1849.

[15] A. H. Castro Neto, F. Guinea, N. M. R. Peres, K. S. Novoselov, and A. K. Geim. The electronic properties of graphene. *Reviews of Modern Physics*, 81:1, 2009. doi:10.1103/RevModPhys.81.109.

[16] P. Blake, E. W. Hill, A. H. Castro Neto, K. S. Novoselov, D. Jiang, R. Yang, T. J. Booth, and A. K. Geim. Making graphene visible. *Applied Physics Letters*, 91: 063124, 2007. doi:10.1063/1.2768624.

[17] K. I. Bolotin, K. J. Sikes, Z. Jiang, M. Klima, G. Fudenberg, H. Hone, P. Kim, and H. L. Stormer. Ultrahigh electron mobility in suspended graphene. *Solid State Communications*, 146:351–355, 2008. doi:10.1016/j.ssc.2008.02.024.

[18] C. R. Dean, A. F. Young, I. Meric, C. Lee, L. Wang, S. Sorgenfrei, K. Watanabe, T. Taniguchi, P. Kim, K. L. Shepard, and J. Hone. Boron nitride substates for high-quality graphene electronics. *Nature Nanotechnology*, 5:722–726, 2010. doi:10.1038/nnano.2010.172.

[19] X. Li, W. Cai, J. An, S. Kim, J. Nah, D. Yang, R. Piner, A. Velamakanni, I. Jung, E. tutuc, S. K. Banerjee, L. Colombo, and R. S. Ruoff. Large-area synthesis of high-quality and uniform graphene films on copper foils. *Science*, 324:1312–1314, 2009. doi:10.1126/science.1171245.

[20] W. Gannett, W. Regan, K. Watanabe, T. Tanighuchi, and Z. Zettl. Boron nitride substrates for high mobility chemical vapor deposited graphene. *Applied Physics Letters*, 98:242105, 2011. doi:10.1063/1.3599708.

[21] C. Berger, Z. Song, X. Li, X. Wu, N. Brown, C. Naud, D. Mayou, T. Li, J. Hass, A. N. Marchenkov, E. H. Conrad, P. N. First, and W. A. de Heer. Electronic confinement and coherence in patterned epitaxial graphene. *Science*, 312:1191–1196, 2006. doi:10.1126/science.1125925.

[22] W. Strupinski, K. Grodecki, A. Wysmolek, R. Stepniewski, T. Szokopek, P. E. Gaskell, A. Grüneis, D. Haberer, R. Bozek, J. Krupka, and J. M. Baranowski.

Graphene epitaxy by chemical vapor deposition on sic. *Nano Letters*, 11:1786–1791, 2011. doi:10.1021/nl200390e.

[23] X. Li, G. Zhang, X. Bai, X. Sun, X. Wang, E. Wang, and H. Dai. Highly conducting graphene sheets and langmuir-blodgett films. *Nature Nanotechnology*, 3:538–542, 2008. doi:10.1038/nnano.2008.210.

[24] N. Tombros, A. Veligura, J. Junesch, J. J. van den Berg, P. J. Zomer, M. Wojtaszek, I. J. Vera Marun, H. T. Jonkman, and B. J. van Wees. Large yield production of high mobility freely suspended graphene electronic devices on a polydimethylglutarimide based organic polymer. *Journal of Applied Physics*, 109:093702, 2011. doi:10.1063/1.3579997.

[25] P. J. Zomer, S. P. Dash, N. Tombros, and B. J. van Wees. A transfer technique for high mobility graphene devices on commercially available hexagonal boron nitride. *Applied Physics Letters*, 99:232104, 2011. doi:10.1063/1.3665405.

[26] T. Taychatanapat, K. Watanabe, T. Taniguchi, and P. Jarillo-Herrero. Quantum hall effect and landau-level crossing of dirac fermions in trilayer graphene. *Nature Physics*, 7:621–625, 2011. doi:10.1038/nphys2008.

[27] O. M. Corbino. Azioni elettromagnetiche dovute agli ioni dei metalli deviati dalla traiettoria normale per effetto di un campo. *Nuovo Cimento*, 1:397–420, 1911. URL `http://fisica.unipv.it/percorsi/pdf/Corbinoazioni.PDF`.

[28] A. Rycerz. Magnetoconductance of the corbino disk in graphene. *Physical Review B*, 81:121404, 2010. doi:10.1103/PhysRevB.81.121404.

[29] D. A. Abanin, S. V. Morozov, L. A. Ponomarenko, R. V. Gorbachev, A. S. Mayorov, M. I. Katsnelson, K. Watanabe, T. Taniguchi, K. S. Novoselov, L. S. Levitov, and A. K. Geim. Giant nonlocality near the dirac point in graphene. *Science*, 332:328, 2011. doi:10.1126/science.1199595.

[30] J. Munárriz, A. V. Malyshev, and F. Domínguez-Adame. Towards a graphene-based quantum interference device. 2011. URL `http://graphita.bo.imm.cnr.it/GraphITA_PDF_Talks/Dominguez_GraphITA_Talk.pdf`.

[31] L. Vicarelli, M. S. Vitiello, D. Coquillat, A. Lombardo, A. C. Ferrari, W. Knap, M. Polini, V. Pellegrini, and A. Tredicucci. Graphene field-effect transistors as room temperature terahertz detectors. *Nature Materials*, 11:865–871, 2012. doi:10.1038/nmat3417.

[32] Frank Pobell. *Matter and Methods at Low Temperatures*. Springer-Verlag, 2007.

[33] H. Ibach and H. Lüth. *Solid-State Physics An Introduction to Principles of Materials Science*. Springer-Verlag, 2009. doi:10.1007/978-3-540-93804-0.

[34] R. B. Laughlin. Quantized hall conductivity in two dimension. *Physical Review B*, 23:5632, 1981. doi:10.1103/PhysRevB.23.5632.

[35] R. B. Laughlin. Anomalous quantum hall effect: An incompressible quantum fluid with fractionally charged excitations. *Physical Review Letters*, 50:1395, 1983. doi:10.1103/PhysRevLett.50.1395.

[36] F. D. M. Haldane. Fractional quantization of the hall effect: A hierarchy of incompressible quantum fluid states. *Physical Review Letters*, 51:605, 1983. doi:10.1103/PhysRevLett.51.605.

[37] J. K. Jain. Composite-fermion approach for the fractional quantum hall effect. *Physical Review Letters*, 63:199, 1989. doi:10.1103/PhysRevLett.63.199.

[38] H. L. Stormer, D. C. Tsui, and A. C. Gossard. The fractional quantum hall effect. *Reviews of Modern Physics*, 71:S298, 1999. doi:10.1103/RevModPhys.71.S298.

[39] W. Pan, J. S. Xia, V. Shvarts, D. E. Adams, H. L. Stormer, D. C. Tsui, L. N. Pfeiffer, and K. W. West. Exact quantization of the even-denominator fractional quantum hall state at $\nu = 5/2$ landau level filling factor. *Physical Review Letters*, 83:3530, 1999. doi:10.1103/PhysRevLett.83.3530.

[40] Y. Zheng and T. Ando. Hall conductivity of a two-dimensional graphite system. *Physical Review B*, 65:245420, 2002. doi:10.1103/PhysRevB.65.245420.

[41] Y. Zhang, J. P. Small, M. S. Purewal, Y. W. Tan, M. Fazlollahi, J. D. Chudow, J. A. Jaszczak, H. L. Stormer, and P. Kim. Landau-level splitting in graphene in high magnetic fields. *Physical Review Letters*, 96:136806–, 2006. doi:10.1103/PhysRevLett.96.136806.

[42] K. L. Bolotin, F. Ghahari, M. D. Shulman, H. L. Stormer, and P. Kim. Observation of the fractional quantum hall effect in graphene. *Nature*, 462:196–199, 2009. doi:10.1038/nature08582.

[43] C. R. Dean, A. F. Young, P. Cadden-Zimansky, L. Wang, H. Ren, K.Watanabe, T. Taniguchi, P. Kim, J. Hone, and K. L. Shepard. Multicomponent fractional quantum hall effect in graphene. *Nature Physics*, 7:693–696, 2011. doi:10.1038/NPHYS2007.

[44] M. Amado, E. Diez, D. López-Romero, F. Rossella, J. M. Caridad, F. Dionigi, V. Bellani, and D. K. Maude. Plateau-insulator transition in graphene. *New Journal of Physics*, 12:053004, 2010. doi:10.1088/1367-2630/12/5/053004.

[45] M. Amado, E. Diez, F. Rossella, V. Bellani, D. López-Romero, and D. K. Maude. Magneto-transport of graphene and quantum phase transitions in the quantum hall regime. *Journal of Physics: Condensed Matter*, 24:305302, 2012. doi:10.1088/0953-8984/24/30/305302.

[46] E. McCann and M. Koshino. The electronic properties of bilayer graphene. *Reports on Progress in Physics*, 76:056503, 2013. doi:10.1088/0034-4885/76/5/056503.

[47] Z. Liu, K. Suenaga, J. F. Harris, and S. Iijima. Open and closed edges of graphene layers. *Physical Review Letters*, 102:015501, 2009. doi:10.1103/PhysRevLett.102.015501.

[48] M. Freitag. Graphene: trilayers unravelled. *Nature Physics*, 7:596, 2011. doi:10.1038/nphys2032.

[49] K. S. Novoselov, E. McCann, S. V. Morozov, V. I. Fal'ko, A. K. Geim, F. Scholin, and D. Jiang. Unconventional quantum hall effect and berry's phase of 2π in bilayer graphene. *Nature Physics*, 2:177–180, 2006. doi:10.1038/nphys245.

[50] E. McCann and V. I. Fal'ko. Landau-level degeneracy and quantum hall effect in a graphite bilayer. *Physical Review Letters*, 96:086805, 2006. doi:10.1103/PhysRevLett.96.086805.

[51] Y. Zhao, P. Cadden-Zimansky, Z. Jiang, and P. Kim. Symmetry breaking in the zero-energy landau level in bilayer graphene. *Physical Review Letters*, 104:066801, 2010. doi:10.1103/PhysRevLett.104.066801.

[52] A. Kumar, W. Escoffier, J. M. Poumirol, C. Faugeras, D. P. Arovas, M. M. Fogler, F. Guinea, S. Roche, M. Goiran, and B. Raquet. Integer quantum hall effect in trilayer graphene. *Physical Review Letters*, 107:126806, 2011. doi:PhysRevLett.107.126806.

[53] J. Moser, A. Barreiro, and A. Bachtold. Current-induced cleaning of graphene. *Applied Physics Letters*, 91:163513, 2007. doi:10.1063/1.2789673.

[54] Z. Cheng, Q. Zhou, C. Wang, Q. Li, C. Wang, and Y. Fang. Toward intrinsic graphene surfaces: A systematic study on thermal annealing and wet-chemical treatment of sio_2-supported graphene devices. *Nano Letters*, 11:767–771, 2011. doi:10.1021/nl103977d.

[55] N. W. Ashcroft and N. D. Mermin. *Solid State Physics*. Hartcourt College Publishers, 1976.

[56] C. Cobaleda, F. Rossella, S. Pezzini, E. diez, V. Bellani, D. K. Maude, and P. Blake. Quantum hall effect in bilayer and trilayer graphene. *Physica Status Solidi (c)*, 9: 1411–1414, 2012. doi:10.1002/pssc.201100657.

[57] C. Cobaleda, E. Diez, M. Amado, S. Pezzini, F. Rossella, V. Bellani, D.López-Romero, and D. K. Maude. Quantum hall effect in monolayer, bilayer and trilayer graphene. *Journal of Physics: Conference Series*, 456:012006, 2013. doi:10.1088/1742-6596/456/1/012006.

[58] C. Cobaleda, F. Rossella, S. Pezzini, E. Diez, V. Bellani, D. K. Maude, and P. Blake. Quantum hall effect in inhomogeneous trilayer graphene. *Physica E: Low-dimensional Systems and Nanostructures*, 44:530–533, 2011. doi:10.1016/j.physe.2011.10.007.

[59] A. C. Ferrari, J. C. Meyer, V. Scardaci, C. Casiraghi, M. Lazzeri, F. Mauri, S. Piscanec, D. Jiang, K. S. Novoselov, S. Roth, and A. K. Geim. Raman spectrum of graphene and graphene layers. *Physical Review Letters*, 97:187401, 2006. doi:10.1103/PhysRevLett.97.187401.

[60] B. Karmakar, M.R. Gokhale, A.P. Shah, B.M. Arora, D.T.N. de Lang, A.de Visser, L.A. Ponomarenko, and A.M.M. Pruisken. The effects of macroscopic inhomogeneities on the magnetotransport properties of the electron gas in two dimensions. *Physica E: Low-dimensional Systems and Nanostructures*, 24:187–210, 2004. doi:10.1016/j.physe.2004.03.019.

[61] Subir Sachdev. *Quantum Phase Transitions*. Cambridge University Press, 2011.

[62] H. P. Wei, D. C. Tsui, M. A. Paalanen, and A. M. M. Pruisken. Experiments on delocalization and university in the integral quantum hall effect. *Physical Review Letters*, 61:1294, 1988. doi:10.1103/PhysRevLett.61.1294.

[63] A. M. M. Pruisken. Universal singularities in the integral quantum hall effect. *Physical Review Letters*, 61:1297, 1988. doi:10.1103/PhysRevLett.61.1297.

[64] S. L. Sondhi, S. M. Girvin, J. P. Carini, and D. Shahar. Continuous quantum phase transitions. *Reviews of Modern Physics*, 69:315, 1997. doi:10.1103/RevModPhys.69.315.

[65] W. Li, C. L. Vicente, J. S. Xia, W. Pan, D. C. Tsui, L. N. Pfeiffer, and K. W. West. Scaling in plateau-to-plateau transition: A direct connection of quantum hall systems with the anderson localization model. *Physical Review Letters*, 102: 216801, 2009. doi:10.1103/PhysRevLett.102.216801.

[66] J. T. Chalker and P. D. Coddington. Percolation, quantum tunnelling and the integer hall effect. *Journal of Physics C*, 21:2665, 1988. doi:10.1088/0022-3719/21/14/008.

[67] E. R. Mucciolo and C. H. Lewenkopf. Disorder and electronic transport in graphene. *Journal of Physics: Condensed Matter*, 22:273201, 2010. doi:10.1088/0953-8984/22/27/273201.

[68] A. J. M. Giesbers, U. Zeitler, L. A. Ponomarenko, R. Yang, K. S. Novoselov, A. K. Geim, and J. C. Maan. Scaling of the quantum hall plateau-plateau transition in graphene. *Physical Review B*, 80:241411, 2009. doi:10.1103/PhysRevB.80.241411.

[69] W. Li, G. A. Csáthy, D. C. Tsui, L. N. Pfeiffer, and K. W. West. Scaling and universality of integer quantum hall plateau-to-plateau transitions. *Physical Review Letters*, 94:206807, 2005. doi:10.1103/PhysRevLett.94.206807.

[70] R. V. Gorbachev, F. V. Tikhonenko, A. S. Mayorov, D. W. Horsell, and A. K. Savchenko. Weak localization in bilayer graphene. *Physical Review Letters*, 98: 176805, 2007. doi:10.1103/PhysRevLett.98.176805.

[71] F. V. Tikhonenko, D. W. Horsell, R. V. Gorbachev, and A. K. Savchenko. Weak localization in graphene flakes. *Physical Review Letters*, 100:056802, 2008. doi:10.1103/PhysRevLett.100.056802.

[72] W. Pan, A. J. Ross III, S. W. Howell, T. Ohta, T. A. Friedmann, and C. T. Liang. Electron-electron interaction in high-quality epitaxial graphene. *New Journal of Physics*, 13:113005, 2011. doi:10.1088/1367-2630/13/11/113005.

[73] S. Pezzini, C. Cobaleda, E. Diez, and V. Bellani. Quantum interference corrections to magnetoconductivity in graphene. *Physical Review B*, 85:165451, 2012. doi:10.1103/PhysRevB.85.165451.

[74] S. V. Morozov, K. S. Novoselov, M. I. Katsnelson, F. Schedin, D. C. Elias, J. A. Jaszczak, and A. K. Geim. Giant intrinsic carrier mobilities in graphene and its bilayer. *Physical Review Letters*, 100:016602, 2008. doi:10.1103/PhysRevLett.100.016602.

[75] S. A. Trugman. Localization, percolation, and the quantum hall effect. *Physical Review B*, 27:7539, 1983. doi:10.1103/PhysRevB.27.7539.

[76] M. Furlan. Electronic transport and the localization length in the quantum hall effect. *Physical Review B*, 57:14818, 1998. doi:10.1103/PhysRevB.57.14818.

[77] C.W.J. Beenakker and H. van Houten. *Quantum Transport in Semiconductor Nanostructures*. Elsevier, 1991. doi:10.1016/S0081-1947(08)60091-0.

[78] B. L. Altshuler, D. Khmel'nitzkii, A. I. Larkin, and P. A. Lee. Magnetoresistance and hall effect in a disordered two-dimensional electron gas. *Physical Review B*, 22:5142, 1980. doi:10.1103/PhysRevB.22.5142.

[79] G. Bergmann. Physical interpretation of weak localization: A time-of-flight experiment with conduction electrons. *Physical Review B*, 28:2914, 1983. doi:10.1103/PhysRevB.28.2914.

[80] Y. Aharonov and D. Bohm. Significance of electromagnetic potentials in the quantum theory. *Physical Review*, 115:485, 1959. doi:10.1103/PhysRev.115.485.

[81] M. I. Katsnelson, K. S. Novoselov, and A. K. Geim. Chiral tunnelling and the klein paradox in graphene. *Nature Physics*, 2:620, 2006. doi:10.1038/nphys384.

[82] N. M. R. Peres. Colloquium: The transport properties of graphene: An introduction. *Reviews of Modern Physics*, 82:2673, 2010. doi:10.1103/RevModPhys.82.2673.

[83] F. V. Tikhonenko, A. A. Kozikov, A. K. Savchenko, and R. V. Gorbachev. Transition between electron localization and antilocalization in graphene. *Physical Review L*, 103:226801, 2009. doi:PhysRevLett.103.226801.

[84] I. Deretzis, G. Fiori, G. Iannaccone, and A. la Magna. Effects due to backscattering and pseudogap features in graphene nanoribbons with single vacancies. *Physical Review B*, 81:085427, 2010. doi:10.1103/PhysRevB.81.085427.

[85] S. Kim, J. Nah, I. Jo, D. Shahrjerdi, L. Colombo, Z. Yao, E. Tutuc, and S. K. Banerjee. Realization of a high mobility dual-gated graphene field-effect transistor with al_2o_3 dielectric. *Applied Physics Letters*, 94:062107, 2009. doi:10.1063/1.3077021.

[86] S. Adam, E. H. Hwang, V. M. Galitski, and S. das Sarma. A self-consistent theory for graphene transport. *Proceedings of the National Academy of Sciences of the United States of America*, 104:18392–18397, 2007. doi:10.1073/pnas.0704772104.

[87] E. McCann, K. Kechedzhi, V. I. Fal'ko, H. Suzuura, T. Ando, and B. L. Altshuler. Weak-localization magnetoresistance and valley symmetry in graphene. *Physical Review Letters*, 97:146805, 2006. doi:10.1103/PhysRevLett.97.146805.

[88] S. Pezzini, C. Cobaleda, E. Diez, and V. Bellani. Disorder and de-coherence in graphene probed by low- temperature magneto-transport: weak localization and weak antilocalization. *Journal of Physics: Conference Series*, 456:012032, 2013. doi:10.1088/1742-6596/456/1/012032.

[89] S. V. Kravchenko, W. E. Mason, G. E. Bowker, J. E. Furneaux, V. M. Pudalov, and M. D'Iorio. Scaling of an anomalous metal-insulator transition in a

two-dimensional system in silicon at $b = 0$. *Physical Review B*, 51:7038, 1995. doi:10.1103/PhysRevB.51.7038.

[90] S. V. Kravchenko, D. Simonian, M. P. Sarachik, W. Mason, and J. E. Furneaux. Electric field scaling at a $b = 0$ metal-insulator transition in two dimensions. *Physical Review Letters*, 77:4938, 1996. doi:10.1103/PhysRevLett.77.4938.

[91] J. B. Oostinga, H. B. Heersche, X. Liu, A. F. Morpurgo, and L. M. K. Vandersypen. Gate-induced insulating state in bilayer graphene devices. *Nature Materials*, 7:151–157, 2008. doi:10.1038/nmat2082.

[92] F. Freitag, J. Trbovic, M. Weiss, and C. Schönenberger. Spontaneously gapped ground stated in suspended bilayer graphene. *Physical Review Letters*, 108:076602, 2012. doi:10.1103/PhysRevLett.108.076602.

[93] S. V. Kravchenko and M. P. Sarachik. Metal-insulator transition in two-dimensional electron systems. *Reports on Progress in Physics*, 67:1–44, 2004. doi:10.1088/0034-4885/67/1/R01.

[94] A. S. Mayorov, D. C. Elias, M. Mucha-Kruczynski, R. V. Gorbachev, T. Tudorovskiya, S. V. Morozov, M. I. Katsnelson, V. I. Fal'ko, A. K. Geim, and K. S. Novoselov. Interaction-driven spectrum reconstruction in bilayer graphene. *Science*, 333:860–863, 2011. doi:10.1126/science.1208683.

[95] G. Borghi, M. Polini, R. Asgari, and A. H. MacDonald. Fermi velocity enhancement in monolayer and bilayer graphene. *Solid State Communications*, 149:1117–1122, 2009. doi:10.1016/j.ssc.2009.02.053.

[96] K. Zou, X. Hong, and J. Zhu. Effective mass of electrons and holes in bilayer graphene: Electron-hole asymmetry and electron-electron interaction. *Physical Review B*, 84:085408, 2011. doi:10.1103/PhysRevB.84.085408.

[97] B. I. Shklovskii and A. L. Efros. *Electronic Properties of Doped Semiconductors*. Springer, 1984.

[98] K. Zou and J. Zhu. Transport in gapped bilayer graphene: The role of potential fluctuations. *Physical Review B*, 82:081407, 2010. doi:10.1103/PhysRevB.82.081407.

[99] J. Velasco Jr., L. Jing, W. Bao, Y. Lee, P. Kratz, V. Aji, M. Bockrath, C. N. Lau, C. Varma, R. Stillwell, D. Smirnov, F. Zhang, J. Jung, and A. H. MacDonald. Transport spectroscopy of symmetry-broken insulating states in bilayer graphene. *Nature Nanotechnology*, 7:156–160, 2012. doi:10.1038/nnano.2011.251.

[100] C. Cobaleda, S. Pezzini, E. Diez, and V. Bellani. Temperature- and density-dependent transport regimes in a h-bn/bilayer graphene/h-bn heterostructure. *Physical Review B*, 89:121404R, 2014. doi:10.1103/PhysRevB.89.121404. URL `http://journals.aps.org/prb/abstract/10.1103/PhysRevB.89.121404`.

[101] H. B. Heersche, P. Jarillo-Herrero, J. B. Oostinga, L. M. K. Vandersypen, and A. F. Morpurgo. Bipolar supercurrent in graphene. *Nature*, 446:56–59, 2007. doi:10.1038/nature05555.

[102] P. Rickhaus, M. Weiss, L. Marot, and C. Schönenberger. Quantum hall effect in graphene with superconducting electrodes. *Nano Letters*, 12:1492–1495, 2012. doi:10.1021/nl204415s.

[103] A. Allain, Z. Han, and V. Bouchiat. Electrical control of the superconducting-to-insulating transition in graphene-metal hybrids. *Nature Materials*, 11:590–594, 2012. doi:10.1038/nmat3335.

[104] K. T. Chan, J. B. Keaton, and M. L. Cohen. First-principles study of metal adatom adsorption on graphene. *Physical Review B*, 77:235430, 2008. doi:10.1103/PhysRevB.77.235430.

[105] X. Liu, C. Z. Wang, M. Hupalo, W. C. Lu, M. C. Tringides, Y. X. Yao, and K. M. Ho. Metals on graphene: correlation between adatom adsorption behavior and growth morphology. *Physical Chemistry Chemical Physics*, 14:9157–9166, 2012. doi:10.1039/C2CP40527J.

[106] I. Gierz, C. Riedl, U. Starke, C. R. Ast, and K. Kern. Atomic hole doping of graphene. *Nano Letters*, 8:4603–4607, 2008. doi:10.1021/nl802996s.

[107] O. Cretu, A. V. Krasheninnikov, J. A. Rodrǵuez-Manzo, L. Sun, R. M. Nieminen, and F. Banhart. Migration and localization of metal atoms on strained graphene. *Physical Review Letters*, 105:196102, 2010. doi:10.1103/PhysRevLett.105.196102.

[108] G. Profeta, M. Calandra, and F. Mauri. Phonon-mediated superconductivity in graphene by lithium deposition. *Nature Physics*, 8:131–134, 2012. doi:10.1038/nphys2181.

[109] X. Xiao, T. E. Beechem, M. T. Brumbach, T. N. Lambert, D. J. Davis, J. R. Michael, C. M. Washburn, J. Wang, S. M. Brozik, D. R. Wheeler, D. B. Burckel, and R. Polsky. Lithographically defined three-dimensional graphene structures. *ACS Nano*, 6:3573–3579, 2012. doi:10.1021/nn300655c.

[110] J. I. Budnick. Some studies of the superconducting transition in purified tantalum. *Physical Review*, 119:1578, 1960. doi:10.1103/PhysRev.119.1578.

[111] T. P. Kaloni, A. V. Balatsky, and U. Schwingenschlögl. Substrate-enhanced superconductivity in li-decorated graphene. *Europhysics Letters*, 104:47013, 2013. doi:10.1209/0295-5075/104/47013.

[112] M. Tinkham. *Introduction to Superconductivity*. McGraw-Hill, 1996.

[113] C. H. Hinrichs and C. A. Swenson. Superconducting critical field of tantalum as a function of temperature and pressure. *Physical Review*, 123:1106, 1961. doi:10.1103/PhysRev.123.1106.